JAN KOCHANOWSKI UNIVERSITY IN KIELCE

DOCTORAL SCHOOL

FACULTY OF NATURAL SCIENCES

PHYSICAL SCIENCES

Valeria Zelina Reyna Ortiz

MULTIPLICITY FLUCTUATIONS IN RELATIVISTIC HEAVY ION COLLISIONS

(Negatively charged hadrons intermittency analysis on Xe+La collisions in NA61/SHINE at CERN SPS)

Doctoral dissertations written under the supervision of:

prof. dr hab. Maciej Rybczyński

dr Tobiasz Czopowicz

Kielce, 2025

This doctoral thesis was financed by the National Science Centre, Poland, under grant number 2020/39/O/ST2/00277 and prepared in collaboration with the NA61/SHINE Collaboration at the CERN SPS.

ACKNOWLEDGEMENTS

I would like to express my deepest gratitude to my supervisor, Maciej Rybczyński, for the opportunity he created for me and for selecting me among several candidates for this project. Although our first collaboration was affected by the war in Ukraine, the lessons and guidance he provided in our field of study have been essential. I am deeply grateful for his patience, eloquence, and unwavering support throughout these four years. Without his invaluable guidance, this project would not have been possible.

I would also like to express my heartfelt gratitude to my auxiliary supervisor, Tobiasz Czopowicz, whose technical expertise and guidance have been instrumental throughout my PhD. His patience, support, and insightful teachings greatly enriched my understanding of physics, computational methods, and the NA61/SHINE experiment. I am equally thankful for his generosity in sharing not only academic knowledge but also advice on Polish and CERN culture.

My sincere thanks go to Francesco Giacosa, director of the PhD school, for believing in me and for doing everything in his power to make me feel welcome and accepted at this university. His concern, advice, and wisdom – both in life and in physics – have always been an inspiration.

I am deeply grateful to Marek Gaździcki, who believed in me and accepted me into the NA61/SHINE collaboration without hesitation after the first project was interrupted. His vast experience in experimental and theoretical particle physics, together with his countless ideas and discussions, was key to the success of this project.

My gratitude also goes to Grzegorz Stefanek, Zbigniew Włodarczyk, Haradhan Adhikary, Katarzyna Grebieszkow, Andrzej Rybicki, Nikolaos Davis, and Giorgio Torreri, whose questions, ideas, comments, and discussions greatly enhanced the quality of the results presented in this thesis and contributed to my growth as a physicist.

My sincere appreciation goes to my NA61/SHINE friends and colleagues – Barnabas Porfy, Piotr Podlaski, Bartosz Maksiak, Simona Ilieva, Mateusz Bajda, Ivan Pidhurski, Yulia Balkova, Aleksandr Dmitriev, Kamil Wójcik, Sakiko Nishimori, Yoshikazu Nagai, Oleksandra Panova, and Yehor Bondar – for their constant support, collaboration, and kindness during my PhD studies.

To my Azerbaijani colleagues, Shahriyar Jafarzade and Narmin Nasibova, thank you for your support and our inspiring physics discussions. My gratitude also goes to my CERN friends, Rafei Hashmi, Joost van Engelen, Merel van der Hoven, Keagan, and Clara Bonniara, for their friendship and encouragement.

To my Mexican friends, Heber and Paulina, thank you for believing in me and encouraging me all

these years. And to Andi Buenrostro, though our paths have separated, I remain grateful for the friendship we shared.

My heartfelt thanks go to Richárd Nagy for his endless patience, care, and encouragement. His faith in me and constant support made even the toughest days easier, and I am deeply grateful to have shared this journey with him.

My infinite and special gratitude goes to Regina and Ursula Stachura – *you are sweeter than a peach*, and I will never be grateful enough for all the kindness you have shown me.

Finally, to my family: To my father, who taught me to stand up every time I fall, to see the value within myself, and to be ambitious and fearless. To my sister, who cheered me up even when I didn't believe in myself, and whose strength and energy I deeply admire. And to my mother, for her constant support along this path – although she doesn't know physics, her kind and heartwarming words have always been my greatest comfort. I will never be thankful enough for all you have done for me.

MULTIPLICITY FLUCTUATIONS IN RELATIVISTIC HEAVY-ION COLLISIONS

(NEGATIVELY CHARGED HADRONS INTERMITTENCY ANALYSIS ON XE+LA COLLISIONS IN NA61/SHINE AT CERN SPS)

Abstract

Valeria Zelina Reyna Ortiz, M.Sc.
Jan Kochanowski University, Kielce
October 2025

Supervisor: prof. dr hab. Maciej Rybczyński
Auxiliary supervisor: dr Tobiasz Czopowicz

The study of the QCD phase diagram is a central topic in both experimental and theoretical research in heavy-ion physics. The comprehensive data collected by the NA61/SHINE experiment during a two-dimensional scan in beam momentum and system size provides a solid foundation for systematically exploring the properties of strongly interacting matter – including the search for non-monotonic dependencies of various correlation and fluctuation observables on collision energy and the size of colliding nuclei. Among the areas of particular interest is the possible existence of the QCD critical point.

Intermittency analysis is a statistical tool applied in heavy-ion collisions that examines scaled factorial moments (SFMs) of multiplicity distributions in two-dimensional transverse momentum space. This method enables the identification of power-law fluctuations, providing insight into various regions of the QCD phase diagram. While proton intermittency has traditionally been used to search for the critical point, the present studies have extended this approach to negatively charged hadrons to gain a broader understanding of QCD interactions.

This thesis presents the results of negatively charged hadrons intermittency for central Xe+La collisions at beam momentum 13A, 19A, 30A, 40A, 75A and 150A GeV/c ($\sqrt{s_{NN}} \approx$ 5.1–16.8 GeV) recorded by NA61/SHINE at the CERN SPS. The intermittency analysis is performed in transverse and cumulative transverse momentum, and statistically independent data sets are used for each subdivision number. The results provided insight into other possible phenomena that can cause misleading signals of the critical point, which have also been reported by other experiments but not fully explored from a physics perspective. Building on these findings, this thesis investigates the underlying physical mechanisms behind such misleading signals using data from the CERN SPS.

Fluktuacje krotności w relatywistycznych zderzeniach ciężkich jonów

(Analiza intermittencyjna ujemnie naładowanych hadronów w zderzeniach Xe+La zarejestrowanych przez NA61/SHINE w CERN SPS)

STRESZCZENIE

mgr Valeria Zelina Reyna Ortiz
Uniwersytet Jana Kochanowskiego w Kielcach
Październik 2025

Promotor: prof. dr hab. Maciej Rybczyński
Promotor pomocniczy: dr Tobiasz Czopowicz

Badanie diagramu fazowego QCD jest kluczowym zagadnieniem zarówno w eksperymentalnych, jak i teoretycznych badaniach nad zderzeniami ciężkich jonów. Obszerne dane zgromadzone przez eksperyment NA61/SHINE podczas dwuwymiarowego skanowania względem pędu wiązki oraz rozmiaru układu stanowią solidną podstawę do systematycznego badania właściwości silnie oddziałującej materii – w tym poszukiwania niemonotonicznych zależności różnych obserwabli korelacyjnych i fluktuacyjnych od energii zderzenia oraz rozmiaru zderzających się jąder. Jednym z obszarów szczególnego zainteresowania jest możliwe istnienie punktu krytycznego QCD.

Analiza intermittencyjna to narzędzie statystyczne stosowane w badaniach zderzeń ciężkich jonów, które analizuje skalowane momenty czynnikowe (SFM) rozkładów krotności w dwuwymiarowej przestrzeni poprzecznego pędu. Metoda ta umożliwia identyfikację fluktuacji o charakterze potęgowym, dostarczając informacji na temat różnych obszarów diagramu fazowego QCD. Choć tradycyjnie analiza intermittencyjna była stosowana do protonów w celu poszukiwania punktu krytycznego, w niniejszych badaniach podejście to rozszerzono na ujemnie naładowane hadrony, aby uzyskać szersze zrozumienie oddziaływań QCD.

W niniejszej pracy przedstawiono wyniki analizy intermittencyjnej ujemnie naładowanych hadronów wyprodukowanych w centralnych zderzeniach Xe+La przy energiach 13A, 19A, 30A, 40A, 75A i 150A GeV/c ($\sqrt{s_{NN}} \approx 5.1$ – 16.8 GeV), zarejestrowanych przez NA61/SHINE na akceleratorze CERN SPS. Analiza intermittencyjna została przeprowadzona w przestrzeni poprzecznego i skumulowanego poprzecznego pędu, przy czym dla każdej liczby podziałów zastosowano statystycznie niezależne zbiory danych. Uzyskane wyniki dostarczyły informacji na temat innych możliwych zjawisk, które mogą powodować mylące sygnały punktu krytycznego, sygnały te były również raportowane przez inne eksperymenty, lecz nie zostały dotychczas w pełni przeanalizowane z fizycznego punktu widzenia. W oparciu o te wyniki, niniejsza praca podejmuje próbę zbadania fizycznych mechanizmów leżących u podstaw tych mylących sygnałów, wykorzystując dane zebrane na CERN SPS.

TABLE OF CONTENTS

List of abbreviations

- **BES** – Beam Energy Scan
- **BES-II** – Beam Energy Scan Ii
- **BPD** – Beam Position Detector
- **CERN** – The European Organization for Nuclear Research (Conseil européen pour la recherche nucléaire)
- **CP** – Critical Point
- **ECR** – Electron Cyclotron Resonance
- **EMC** – European Muon Collaboration
- **GEANT** – GEometry ANd Tracking
- **gTTD** – Geometrical Two Track Distance cut
- **HBT** – Hanbury Brown Twiss
- **KLM** – Krakow-Louisiana-Minnesota collaboration
- **LBNL** – Lawrence Berkeley National Laboratory
- **LEIR** – Low Energy Ion Ring
- **LHC** – Large Hadron Collider
- **LINAC 3** – Linear Accelerator 3
- **LS2/LS3** – Long Shutdown 2/3
- **MC** – Monte Carlo
- **MTPC** – Main TPC
- **mTTD** – momentum based Two Track Distance cut

- **NA** – North Area
- **NA61/SHINE** – North Area Experiment 61 – Super Proton Synchrotron Heavy Ion and Neutrino experiment.
- **PMTs** – photomultiplier tubes
- **PSD** – Projectile Spectator Detector
- **QCD** – Quantum Chromodynamics
- **QGP** – Quark Gluon Plasma
- **RFQ** – Radio Frequency Quadrupole
- **RHIC** – Relativistic Heavy Ion Collider
- **SFMs** – Scaled Factorial Moments
- **SPS** – Super Proton Synchrotron
- **STAR** – Solenoidal Tracker at RHIC
- **TPC** – Time Projection Chamber
- **TTD** – Two Track Distance
- **VTPC** – Vertex TPC
- **WFA** – WaveForm Analyzer

THESIS STRUCTURE

Over the past almost 70 years, the study and comprehension of strongly interacting matter have been one of the challenges of modern particle physics, with theory and experiment trying to complement each other. From a theoretical point of view, Quantum Chromodynamics (QCD) provides the basic theoretical framework for this study, describing the interactions that govern the fundamental constituents of matter. At the same time, experiments in high-energy nuclear collisions develop tools and techniques for laboratory investigations. This field is characterized by overlapping and complementary studies between statistical, particle, and nuclear physics, spanning from the conceptual to the investigative methodologies that evolve.

The Standard Model (SM) successfully explains three of the four fundamental interactions between particles: electromagnetism, weak interaction, and strong interaction. While the SM has led to highly accurate predictions, such as the discovery of the Higgs boson in 2012, it still has several limitations. For example, it fails to explain phenomena like baryon asymmetry, the inclusion of gravity, the nature of dark matter, and – relevant to this thesis – the understanding of the phase diagram of strongly interacting matter. In particular, the search for the expected phase transition and the critical point between the hadronic gas (HG) and quark-gluon plasma (QGP) remains incomplete, with the precise location of the critical point of hadronic matter in heavy-ion collisions.

From the experimental point of view, we have High Energy Physics (HEP). Studying strong interactions goes beyond simply studying particles like electrons. We study heavy ions, which are atoms that have lost some (or all) of their electrons, leaving behind a nucleus made up of protons and neutrons. These heavy ions are then accelerated to nearly the speed of light using particle accelerators to make a collision. When these ions collide, they release a huge amount of energy, causing the nuclei to break apart and form new particles. The goal of heavy-ion experiments is to recreate the extreme conditions that existed in the early universe, allowing scientists to study how matter behaves under such extreme conditions and strong interactions between particles.

In the search for the critical point of strongly interacting matter and the study of the phase diagram, different techniques have been used to analyze particle collisions in heavy-ion experiments. One of the themes is intermittency. The original purpose of this research was to expand and

contrast the results of intermittency from the NA61/SHINE experiment with other experiments and confirm previous works in the area; however, the NA61/SHINE results obtained were not the ones expected and provided an opportunity for research into the physics of particle correlations, triggering several discussions that will be covered in this text.

Thesis outline

The goal of this project is to study strongly interacting matter by measuring scaled factorial moments (SFMs) for a selection of negatively charged hadrons (produced in strong and electromagnetic interactions) in ^{129}Xe+^{139}La interactions at 13A–150A GeV/c beam momentum ($\sqrt{s_{NN}} \approx 5.1 - 16.8$ GeV).

The present writing is organized into five chapters as follows:

- Chapter one contains a brief introduction to this thesis. The Author's efforts are directed to write this thesis in a very comprehensive way for future readers.
- Chapter two introduces the basic physics concepts related to the phase diagram of strongly interacting matter and the critical point.
- The third chapter summarizes intermittency as a concept and the evolution of this technique across time and previous results, and also treats the approach used in this work.
- The fourth chapter describes NA61/SHINE as a whole, emphasizing the strong interaction program and the search for the critical point.
- The fifth chapter is the most technical chapter of all, and the Author advises the reader to be aware of it. Details of the work related to NA61/SHINE are listed here for reproducibility purposes.
- Chapter six summarizes and discusses the results obtained, remarking on the impact of understanding and discussing physics beyond any data analysis work.

The Appendices organize additional content; furthermore, a compilation of acronyms can be found at the beginning of this thesis.

Author's contributions and achievements

Although devoted to the completion of the present thesis, the Author was also involved in several activities listed below:.

Co-authorship in publications

- V. Z. Reyna Ortiz, M. Rybczynski, Z. Wlodarczyk, U. Shah, A.Bazgir. *Imprint of clustering in multiplicity fluctuations*, Eur. Phys. J. A **59** (2023) 62.
- V. Z. Reyna Ortiz, M. Rybczynski, Z. Wlodarczyk, *A Monte Carlo study of multiplicity fluctuations in proton-proton collisions at* $\sqrt{s} \sim 7$ *TeV*, Phys. Rev. D **108** (2023) 074009.
- V. Z. Reyna Ortiz, M. Rybczynski, Z. Wlodarczyk, *Probing multi-particle bunching from intermittency analysis in relativistic heavy-ion collisions*, Nucl. Phys. A **1053** (2025) 122980.
- V. Z. Reyna Ortiz, M. Rybczynski, Z. Wlodarczyk, *Scaling for count-in-cell and factorial moment analysis*, Nucl. Phys. B **1018** (2025) 117051

Collaboration papers

- M. Alvarado, A. Ayala, M. A. Ayala-Torres, W. Bietenholz, I. Dominguez, et al., *A beam–beam monitoring detector for the MPD experiment at NICA*, Nucl. Instrum. Meth. A **953** (2020) 163150.
- R. Acevedo Kado, M. A. Hernández, A. Ayala, M. A. Ayala Torres, W. Bietenholz, et al., *The conceptual design of the miniBeBe detector proposed for NICA-MPD*, JINST **16** (2021) P02002.
- M. A. Ayala Torres, L. G. Espinoza Beltrán, M. A. Fontaine Sánchez, L. A. Hernández-Cruz, L. M. Montaño, et al., *The MPD-NICA experiment at JINR*, JINST **17** (2022) P09031.
- MPD Collaboration, V. Abgaryan et al., *Status and initial physics performance studies of the MPD experiment at NICA*, Eur. Phys. J. A **58** (2022) 140.
- NA61/SHINE Collaboration, H. Adhikary et al., *Search for a critical point of strongly-interacting matter in* ^{40}Ar + ^{45}Sc *collisions at 150 A GeV*/c *using scaled factorial moments of protons*, Eur. Phys. J. C **83** (2023) 881.
- NA61/SHINE Collaboration, H. Adhikary et al., *Measurements of* π^+, π^-, p, $\bar{p}$, K^+ *and* K^- *production in 120 GeV* $p+C$ *interactions*, Phys. Rev. D **108** (2023) 072013.
- NA61/SHINE Collaboration, H. Adhikary et al., *Measurements of* $\pi^{\pm}$, $K^{\pm}$, p *and* $\bar{p}$ *spectra in* ^{40}Ar + ^{45}Sc *collisions at 13A to 150A GeV*/c, Eur. Phys. J. A **59** (2023) 62.

- NA61/SHINE Collaboration, H. Adhikary et al., *Two-pion femtoscopic correlations in Be+Be collisions at* $\sqrt{s_{NN}}$ = 16.84 *measured by NA61/SHINE at CERN*, Eur. Phys. J. C **83** (2023) 919.

- NA61/SHINE Collaboration, H. Adhikary et al., *Measurements of higher-order cumulants of multiplicity and net-electric charge distributions in inelastic proton–proton interactions by NA61/SHINE*, Eur. Phys. J. C **84** (2024) 416.

- NA61/SHINE Collaboration, H. Adhikary et al., *Search for a critical point of strongly-interacting matter in central* ^{40}Ar + ^{45}Sc *collisions at 13 A–75 A GeV/c beam momentum*, Eur. Phys. J. C **84** (2024) 741.

- NA61/SHINE Collaboration, H. Adhikary et al., K^0_S *meson production in inelastic p+p interactions at 31, 40, and 80 GeV/c beam momentum measured by NA61/SHINE at the CERN SPS*, Eur. Phys. J. C **84** (2024) 820.

- NA61/SHINE Collaboration, H. Adhikary et al., *Evidence of isospin-symmetry violation in high-energy collisions of atomic nuclei*, Nature Commun. *16* (2025) 1, 2849

- NA61/SHINE Collaboration, H. Adhikary et al., Measurement of the mass-changing, charge-changing, and production cross sections of ^{11}C, ^{11}B, and ^{10}B nuclei in ^{12}C+p interactions at 13.5GeV/c per nucleon Phys.Rev.C **111** (2025) 5, 054606

- NA61/SHINE Collaboration, H. Adhikary et al.,

  Multiplicity and net-electric charge fluctuations in central Ar+Sc interactions at 13A, 19A, 30A, 40A, 75A, and 150A GeV/c beam momenta measured by NA61/SHINE at the CERN SPS, Eur.Phys. J.C **85** (2025) 8, 918

Conference activities

- PhD Forum of the Jan Kochanowski University of 2022, Kielce, Poland, June 2022. *Status of intermittency analysis for Xe+La at 150A GeV/c with higher-order factorial moments*.

- NASixtyOne Collaboration Meeting, Wroclaw, Poland, September 26-30, 2022. *Negatively charged hadron intermittency at Xe+La 150A GeV/c*.

- NA61/SHINE Collaboration Meeting, Jura Krakowsko-Częstochowska, Poland, March 27-31, 2023. *Negatively charged hadron intermittency at Xe+La 150A GeV/c*.

- PhD Forum of the Jan Kochanowski University of Kielce 2023, Kielce, Poland, June 6-7, 2023. *h minus intermittency analysis*.

- NA61/SHINE Collaboration Meeting, CERN, Geneva, Switzerland, September 15-19, 2023. *Organizer*. *Negatively charged hadron intermittency at Xe+La 150A GeV/c*.
- NA61/SHINE Collaboration Meeting, Sofia, Bulgaria, April 15-19, 2024. *Negatively charged hadron intermittency at Xe+La 150A GeV/c*.
- CPOD 2024 - 15th Workshop on critical point and Onset of Deconfinement, Berkeley, California (US), May 20-24, 2024. *Measurements of negatively charged hadron intermittency in central Xe+La at 150A GeV/c by NA61/SHINE at CERN SPS*.
- PhD Forum of the Jan Kochanowski University of Kielce 2024, Kielce, Poland, June 6-7, 2024. *Puzzle of h minus intermittency analysis*.
- NA61/SHINE Collaboration Meeting, CERN, Geneva, Switzerland, September 15-19, 2024. *Negatively charged hadron intermittency: Xe+La energy dependence*.
- New Trends in High-Energy and Low-x Physics, Sfantu Gheorghe, Romania, September 2-5, 2024. *Search for the critical point via intermittency analysis in NA61/SHINE at CERN*.
- 24th ZIMÁNYI SCHOOL WINTER WORKSHOP ON HEAVY-ION PHYSICS, Budapest, Hungary, December 3, 2024. *Search for the critical point via intermittency analysis in NA61/SHINE at CERN*.
- XVII Polish Workshop of Relativistic-Ion Physics, Warsaw, Poland, December 14-15, 2024. *Search for the critical point in NA61/SHINE*.
- Quark Matter 2025, Frankfurt, Germany, April 5-13, 2025. *Search for the critical point via intermittency analysis in NA61/SHINE at CERN*.

Conference proceedings

- V. Z. Reyna Ortiz (Jan Kochanowski U.) for the NA61/SHINE Collaboration, *Search for the critical point via intermittency analysis in NA61/SHINE*, Ukr. J. Phys. **69** (2024) 858.

Grants

- NCN Grant No. 2020/39/O/ST2/00277 for PhD studies at the Jan Kochanowski University of Kielce.
- UJK Rector grant 2022.
- NAWA Preludium Bis 2: for a 6-month internship at CERN, Geneva, Switzerland.
- UJK Rector grant 2023.

- Regional Initiative for Excellence (RID) Young Researcher (2024) nr. RID/2024/MB/06, funding for two conferences related to PhD studies.

Awards

- Best talk at the PhD Forum of the Jan Kochanowski University of Kielce 2024.

Other scientific activities

Workshops/Schools

- CERN School of Computing (CSC 2023). Tartu, Estonia.
- 2025 CERN-Fermilab Hadron Collider Physics Summer School (HCP 2025). Geneva, Switzerland.

Activities related to NA61/SHINE

- Presentation: "El experimento NA61/SHINE, quark-gluon plasma, neutrinos y rayos cósmicos". Seminar of Particle Physics, Benemerita Universidad Autónoma de Puebla. Puebla, Mexico. January 2024.
- Deputy expert for the Detector Control System (DCS) during NA61/SHINE neutrino data taking campaign, July 2024.
- Deputy expert for the Detector Control System (DCS) and Run coordinator during NA61/SHINE heavy-ion and cosmic ray data-taking campaign in November 2024.
- NA61/SHINE Outreach deputy 2023–2025.
- NA61/SHINE Outreach coordinator 2024 – today.
- Status of "Preliminary results of NA61/SHINE experiment" for analysis: Negatively charged hadrons intermittency at ^{129}Xe+^{139}La 150A GeV/c.

CHAPTER 1

INTRODUCTION

1.1 The QCD phase diagram overview

The Standard Model of particle physics is a quantum field theory that describes the fundamental constituents of matter – fermions (quarks and leptons) – and their interactions via three of the four known fundamental forces: electromagnetism, the weak interaction, and the strong interaction. These forces are mediated by gauge bosons: the photons, W and Z bosons, and gluons, respectively. Gravity, although fundamental, is not included in the Standard Model and is described separately by general relativity. Quarks combine to form hadrons such as protons and neutrons, and interact through quantum chromodynamics (QCD), the non-Abelian gauge theory of the strong force.

At extreme temperatures and baryon densities, as realized in relativistic heavy-ion collisions, QCD predicts a transition from hadronic matter to a deconfined state known as the quark-gluon plasma (QGP). These transitions are mapped to the QCD phase diagram, which encodes different states of strongly interacting matter. Understanding matter in its different states is one of the most fundamental problems in science. Matter exists in various forms, which are determined by the conditions governing the transitions between phases. These conditions can be summarized in phase diagrams. A phase transition refers to the transformation of a substance from one state of matter to another, occurring due to variations in external conditions such as pressure and temperature. During these transitions, specific quantities often change in a discontinuous manner.

One example of a phase transition and its corresponding phase diagram is that of water, which we use daily in its liquid, solid, and gas phases by changing its external conditions (pressure and

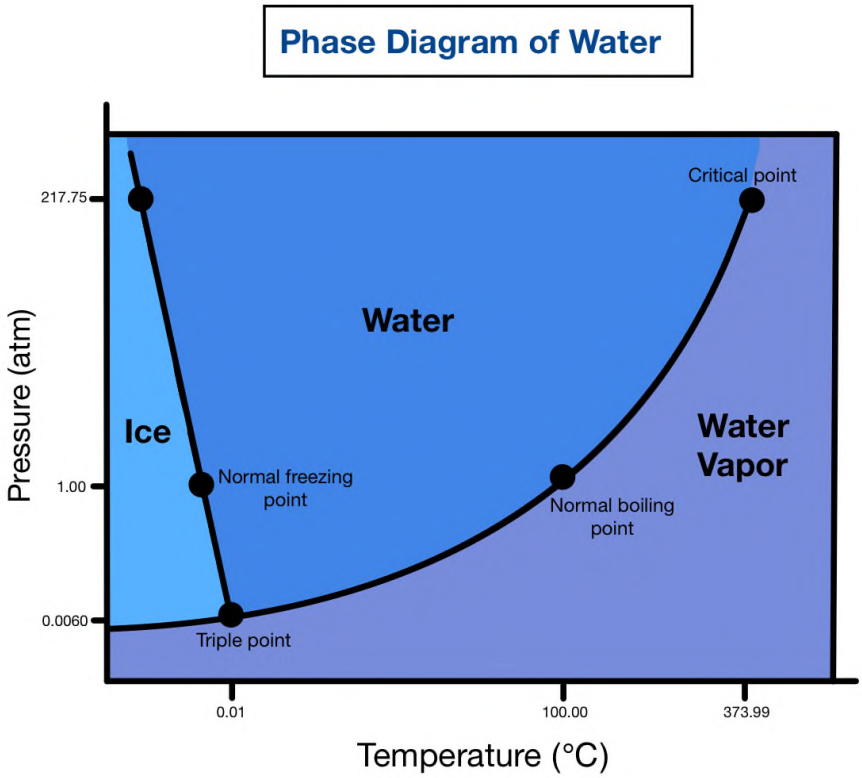

Figure 1.1: Phase diagram of water. Image from `https://www.expii.com/t/phase-change-diagram-of-water-overview-importance-8031`

temperature). A water diagram is shown in Fig. 1.1, where the solid black lines represent the values of temperature and pressure at which phase transitions occur. Notice in the figure that there is a triple point where the three phases coexist, and the phase transition lines intersect.

The research discussed in this thesis is related to the phase diagram of strongly interacting matter, known as the QCD phase diagram, which, as we mentioned, is not yet well explored. The conjectured QCD phase diagram shown in Fig. 1.2 is the temperature-baryon chemical potential ($T-\mu_B$ diagram). The baryon chemical potential is the chemical potential defined as $\mu_B = \delta E/\delta N|_{S,V}$ where E is the system energy, N is the number of particles, S is the entropy, and V is the volume. Therefore, its meaning is the energy cost to add a particle to the system while its entropy and volume are fixed.

In principle, QCD could lead to a three-state phase structure as a function of the temperature T and the baryochemical potential μ_B as shown in Fig. 1.2 [1]. In this diagram, we can describe specific scenarios: The quarks are *dressed*, in more formal terms, confined and bonded by gluons.

[1] It is not the intention of the author to give a whole lecture on this topic, for a full text and discussion please review [1]–[3]

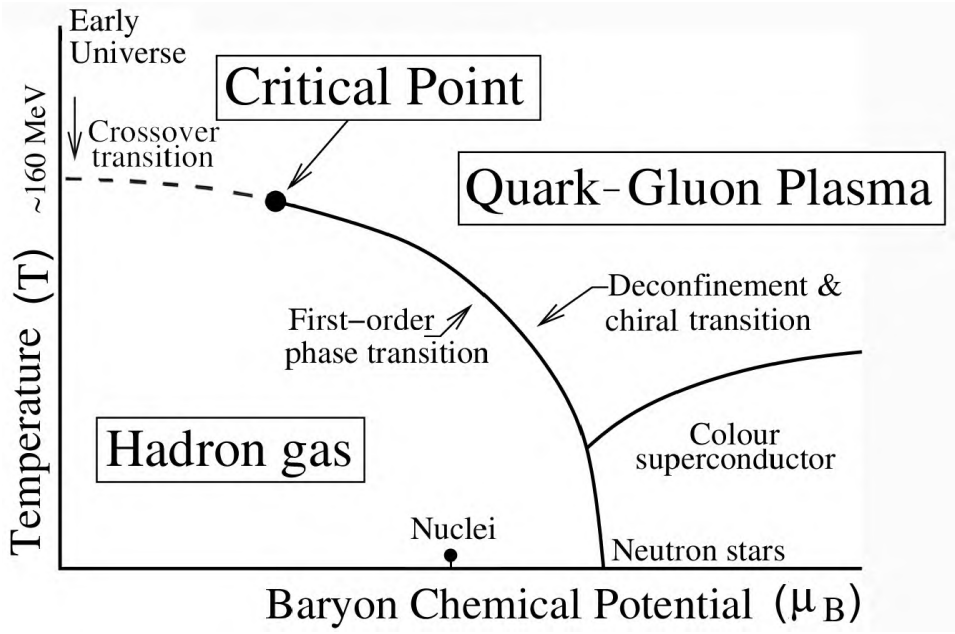

Figure 1.2: QCD Phase diagram. Image from `https://www.gauss-centre.eu/results/elementaryparticlephysics/the-qcd-phase-diagram-and-equation-of-state`

But at very high T and/or μ_B, this gluonic dressing *evaporates*, leaving pointlike quarks and gluons, a plasma where quarks and gluons are deconfined; this is the quark gluon plasma.

At low temperatures and density, hadronic matter consists of interacting mesons and baryons. By increasing the temperature or system density, the system approaches limits beyond which a description of interacting hadrons breaks down. The result is the boundary curve of the hadronic matter regime in Fig. 1.2 that is expected to correspond to different transition patterns at low and high μ_B.

The QCD phase diagram is one of the central topics in strong interaction studies; however, although it has been studied both theoretically and experimentally over the years, no firm theoretical basis has been established so far. The phase and transition structure is non-perturbative, and the only tool we have in that domain is lattice QCD [1], [2]. Our current understanding of evaluating lattice QCD is based on numerical simulations using Monte Carlo techniques, which break down for finite baryon densities. For this reason, much of what is presently discussed for the QCD phase structure is based on effective field theory models.

1.2 The critical point

In between the regions of confinement and deconfinement; the diagram in Fig. 1.3 shows a non-singular *cross-over* region for $0 \leq \mu_B < \mu_c$, a critical point (continuous transition) at μ_c, and

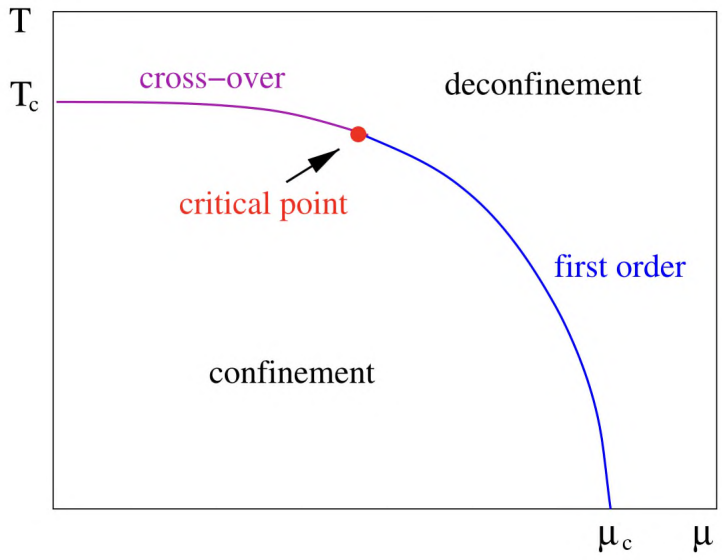

Figure 1.3: Expected QCD phase structure with critical point and crossover region.

finally a line of first-order transitions that separates the phases down to $T = 0$, μ_c. However, the predictions of the position of the critical point depend entirely on the details of the model, the number of flavors, and the parameters chosen.

The question remains: could one find evidence for a critical point at some μ_B and T, at which the "rapid cross-over" would terminate in a critical point and turn into a discontinuous transition?

Considering the different model proposals for the phase diagram of QCD as a function of temperature and baryon density, various attempts have been made from the lattice evaluation point of view, from rewriting the method of lattice configurations [4], using analytical continuation [5], [6], and a power series approach [7].

All mentioned methods have in common at least two main ideas: they start from $\mu_B = 0$ calculations and then extend approximately. This does not permit a quantitative error determination for the results obtained. Given the more or less analytic extension procedure used, the difficulty of these methods increases uncertainties when the critical point is reached. Whether such a difficulty indicates such a point is not evident, but it certainly interferes with studies in the region of large μ_B and low T [1].

However, as pointed out at the beginning of this chapter, the field has different overlapping investigations, the experimental approach involves seeking experimental evidence of the critical point in relativistic heavy-ion collisions, building on existing knowledge.

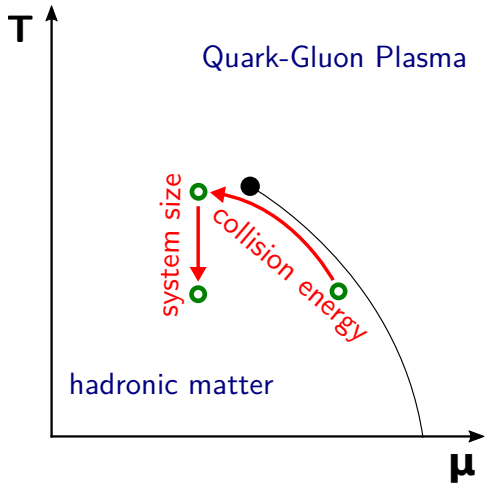

Figure 1.4: How to look for the QCD critical point in heavy-ion collisions.

1.3 Heavy-ion physics experiments

The initial relativistic heavy-ion collision experiments took place at the Bevatron in Berkeley about seventy years ago, utilizing energies between 1–2 GeV [8], and from that point onward, heavy-ion community collided ions at higher energies at different facilities across the world, such as the Alternating Gradient Synchrotron (AGS) at the Brookhaven National Laboratory (BNL) and the Super Proton Synchrotron (SPS) at CERN, providing evidence and unveiling the secrets of QGP formation.

As time has passed, advancements and developments have evolved, leading to the construction of more powerful accelerators. In previous years, the path to understanding heavy-ion collisions was paved through experiments like NA35 and NA49 at the SPS at CERN, which were the first to study the properties of the quark-gluon plasma. The scientific contributions of NA49 encouraged generations and teams worldwide to build larger experiments and more extensive, robust interaction programs that are still in operation today. Such as:

- The Relativistic Heavy-Ion Collider (RHIC) at the BNL, which started operations in 2000, and the Beam Energy Scan-II (BES-II) program that has generated a comprehensive set of results, providing a solid foundation for further discussion.
- NA61/SHINE at CERN SPS, heritage of NA49 knowledge and facility with a solid, strong interactions program alongside a neutrino and cosmic ray programs.
- ALICE at CERN LHC that can achieve colliding energies without precedents.

These facilities use complex detectors and techniques to track and study the millions of par-

ticles produced in each collision[2]. Relevant to the present work are the results from STAR at RHIC, which will be discussed in the following section, and previous results from NA49 and NA61/SHINE, related to the search for the critical point; these detectors take the lead in technology combining hardware and software, physics and data analysis to unveil the products of heavy-ion collisions.

As shown in Fig. 1.4, experimental exploration of the QCD phase diagram involves a two-dimensional scan in collision energy and system size. By varying parameters such as the beam energy, mass number of the nuclei, and collision centrality – quantities that can be precisely controlled in the laboratory – experiments effectively access different combinations of temperature (T) and baryochemical potential (μ_B) [9]–[11].

1.4 The experimental search for the QCD critical point

The critical point in QCD phase transitions was first speculated on in the early 1970s as part of the study of phase transitions [12], particularly in the context of first-order phase transitions. However, at this time, the exact nature of the QCD phase diagram was still uncertain.

Early experimental efforts

Before the large-scale experiments, various nuclear physics facilities conducted heavy-ion collision experiments to explore the behavior of nuclear matter at high temperatures and densities. These facilities include the Bevalac at Lawrence Berkeley National Laboratory (LBNL) and the CERN Super Proton Synchrotron (SPS).

In the 1980s, the Bevalac accelerator at the Lawrence Berkeley National Laboratory (LBNL) in the United States was one of the first to conduct experiments with heavy-ion collisions at relatively high energies. These early experiments primarily aimed to study nuclear matter under conditions that could lead to the creation of QGP. They provided the first hints of the kind of energy and collision conditions needed to study the QCD phase diagram.

The CERN Super Proton Synchrotron (SPS) was one of the first major facilities to increase collision energies for heavy-ion collisions in the early 1990s. The experiments conducted by the CERN collaborations WA98 and NA49 at the SPS focused on high-energy lead-lead (Pb+Pb) collisions, where they studied the production of strange particles, jets, and other signatures of Quark-Gluon Plasma (QGP). These experiments played a crucial role in confirming the theoretical predictions of QGP, leading to the initial indications of a QGP-like state in these high-energy collisions.

[2]In the future, we expect that the list of facilities and knowledge will expand by building complexes like FAIR at GSI and NICA at JINR.

During the 1990s, the SPS experiments at CERN also began to show the first signs of collective flow and strangeness enhancement, phenomena that are expected to occur with the formation of QGP. Although these experiments provided evidence for the formation of QGP, they did not directly probe the critical point. Nonetheless, they emphasized the need for further exploration of the QCD phase diagram at different energies and baryon densities.

Contemporary efforts

By the mid-2000s, both LBNL and CERN began to focus more on searching for the critical point. This search was driven by experimental signatures that could provide evidence for the first-order phase transition, such as enhanced fluctuations, critical slowing down, and non-monotonic behavior of certain observables as a function of collision energy [13].

In 2010, RHIC initiated a series of experiments with lower collision energies, aiming to explore the transition from a QGP to a hadronic phase in greater detail, and to explore areas of the phase diagram where the presence of the critical point has been theoretically anticipated. One significant effort was the BES program at RHIC, which aimed to map out the behavior of the QCD phase diagram at lower temperatures and higher baryon densities.

As of the 2010s, heavy-ion collision experiments have made significant progress in narrowing the search for the critical point. RHIC, SPS, and the LHC continue to study the properties of the QGP and fluctuations that may indicate the presence of a critical point. In addition, new experimental techniques have been developed to measure particle correlations and fluctuations with greater precision, which could provide hints of the existence of the critical point.

NA61/SHINE is particularly important because it explores low-to-intermediate energies in heavy-ion collisions, which are unavailable to study at other facilities like RHIC or LHC that focus on higher energies. These lower-energy collisions are crucial because they allow for exploring high baryon densities, where the localization of the critical point is predicted. A resume of the energy scan done by experimental search at SPS can be seen in Fig. 1.5.

The search for the QCD critical point in heavy-ion collisions employs sophisticated techniques aimed at detecting signatures of critical phenomena, including enhanced fluctuations, correlations, and non-monotonic behaviors. Below is a summary of the most relevant methods currently in use:

- **Fluctuations and Cumulants:** Near the critical point, fluctuations in the number of produced particles in the *net-baryon number of* (difference between the number of baryons and anti-baryons) and *net-charge* (difference between positively and negatively charged particles) are expected to be enhanced. These fluctuations are a direct signature of the critical point. Using *cumulants*, which quantify the higher-order moments of distributions, is crucial in analyzing these fluctuations. For example, the *net-proton cumulants* and *net-*

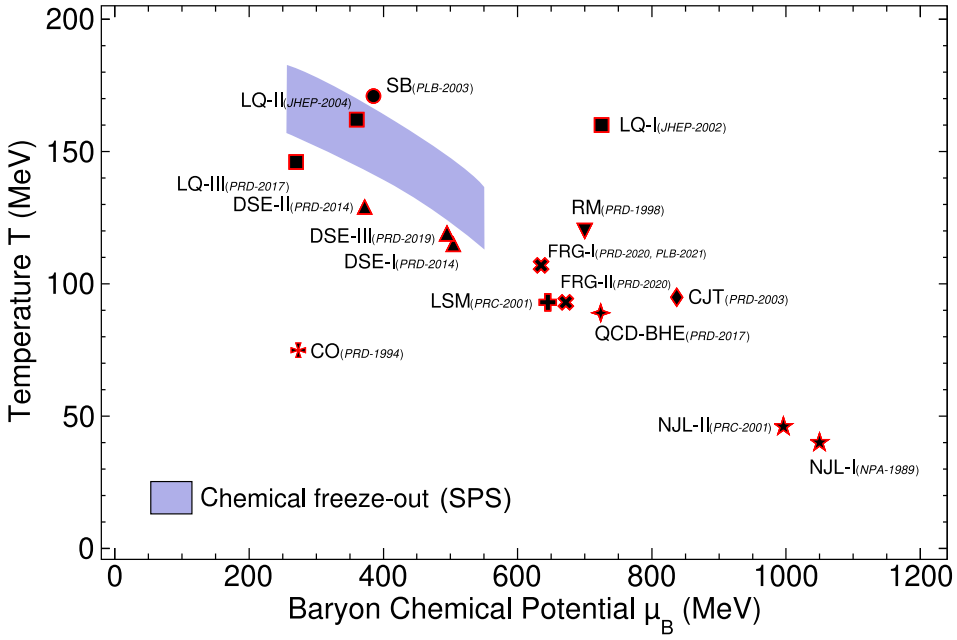

Figure 1.5: Experimental search for the critical point at SPS

charge cumulants can provide insight into the system's approach to the critical point by revealing enhanced fluctuations or deviations from normal statistical behavior [14], [15].

- **Femtoscopy:** *Femtoscopy* techniques, such as *Hanbury Brown-Twiss (HBT)* interferometry, are used to study the *space-time structure* of the collision zone. Femtoscopy measures the correlations between pairs of particles in the final state, revealing information about the size, shape, and evolution of the particle-emitting source. The *space-time evolution* of the system is sensitive to the dynamics near the critical point. The critical point could manifest as a change in the size or correlation radii of the source due to the system's transition from hadronic matter to a quark-gluon plasma and back to hadrons.

- **Intermittency** refers to the scaling behavior of multiplicity fluctuations over small phases of space or time. In heavy-ion collisions, intermittency is expected to become more pronounced as the system approaches the critical point. The particles are not uniformly distributed in space, and small-scale fluctuations might follow a power-law scaling, indicative of *fractal-like behavior* in the particle distributions. Intermittency provides a signature of the critical point by demonstrating how fluctuations in particle production intensify at smaller scales. More details will be discussed in the following chapter.

These techniques aim to detect the critical phenomena associated with the QCD critical point. However, there is no precise calculation in the currently existing models that can determine its exact location. At the same time, the results given by the RHIC BES-II program and NA61/SHINE

converge at one point: definitive evidence of the critical point has not been found. The results are inconclusive or not physically understood; therefore, they are open to discussion in the community of high-energy physics. The results obtained in the elaboration of this thesis contribute to the debate that there exist "misleading signals," i.e., results that, if not correctly understood, could be interpreted as a signal of the critical point. However, these fake signals could be nothing more than the physics of phenomena unrelated to the critical point. This discussion will be addressed from the experimental point of view throughout this text, and will also include the most recent comments from the community.

CHAPTER 2

INTERMITTENCY ANALYSIS

Intermittency characterizes irregular, scale-dependent fluctuations that deviate from smooth statistical behavior. As a simplified example, consider placing N particles into a volume R, which e study heavy-ions is then divided into n subregions (cells) of size L, with $n = R/L$. Define k_m as the particle count in the m-th cell, constrained by $\sum k_m = N$. By varying n while holding R and N constant, we investigate how the system responds to finer resolution. Uniform distributions yield minimal variance, while strong clustering, such as all particles falling in a single cell, produces pronounced fluctuations [16]. Analytical methods introduced in this chapter will quantify such behavior, revisiting the conceptual basis of this approach.

2.1 The original concept

The concept of *intermittency* has evolved significantly over time, now encompassing a broad class of phenomena characterized by irregular, non-uniform behavior. Observed initially in fluid turbulence, intermittency was first identified by O. Reynolds [17], [18], who described **temporal intermittency** as brief, intense fluctuations interrupting otherwise calm flow conditions. Later studies revealed that energy dissipation in fully developed turbulence occurs in small, localized regions – an effect known as **spatial intermittency**. These findings showed that turbulence does not evolve smoothly but rather through sporadic bursts in both time and space. In chaos theory, intermittency further describes systems that alternate unpredictably between ordered and chaotic behavior. Though the concept played a foundational role in understanding complex systems, especially in fluid dynamics and chaos, its exploration in high-energy and particle physics remains limited [19].

Intermittency in multiparticle production

It was 1986 when A. Białas and R. Pechanski, inspired by the concept in chaos theory, formally introduced the concept of intermittency through a scientific publication into multiparticle production [20] and extended it two years later [21]; they were inspired by the search for new ways to understand the abundance of new multiparticle data becoming available. These two publications depart from two key ideas: firstly, the self-similar cascades, a possible mechanism for particle production and the effect of self-similarity on the behavior of bin-to-bin fluctuations; secondly, the relationship between the theoretical particle distribution function and the experimental distribution, which includes the impact of trivial fluctuations due to finite particle number.

In these publications, the authors proposed to study Scaled Factorial Moments of the number of particles produced in high-energy collisions as a function of the resolution size of rapidity interval[1], as fluctuations of self-similar cascading [22].

2.2 Scaled Factorial Moments

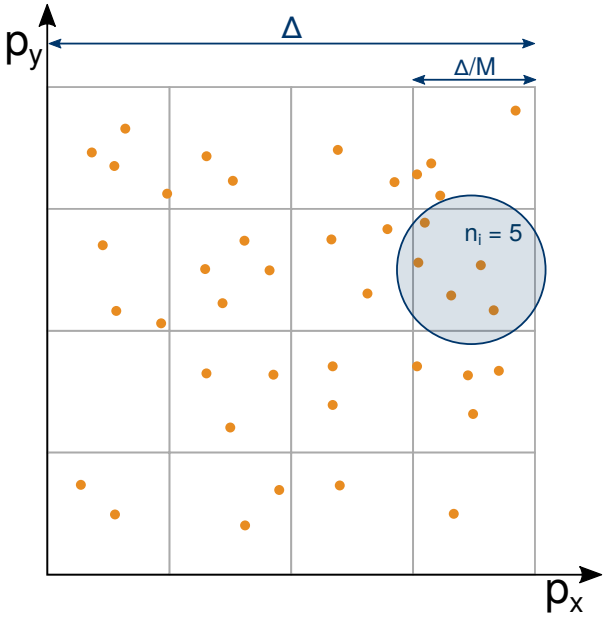

Figure 2.1: Two-dimensional transverse momentum space sub-divided into $M \times M$ number of equally sized cells. Where n_i corresponds to the particle multiplicity in a cell, Δ is the momentum region, and δ is the bin-width. Figure is taken from [23].

Scaled Factorial Moments (SFMs) help to reduce statistical bias caused by the finite number of particles produced in a single collision. At the same time, this measure is sensitive to significant dynamic phenomena, such as the emergence of new scales in particle production or the presence

[1]Rapidity y is used as an example, but the mechanism can be (and will be) set up with any variables in any number of dimensions.

of "intermittent" background-cascading fluctuations across different scales. Additionally, this method enables the identification of significant fluctuations, such as those occurring at the second-order phase transition [20].

The Scaled Factorial Moments, $F_r(M)$ of order r are defined for a two dimensional phase-space as shown in Fig. 2.1 :

$$F_r(M) = \frac{\left\langle \frac{1}{M}\sum_{i=1}^{M} n_i ... (n_i - r + 1) \right\rangle}{\left\langle \frac{1}{M}\sum_{i=1}^{M} n_i \right\rangle^r}, \tag{2.1}$$

where M is the number of 2-dimensional cells in which the 2-dimensional space is partitioned, n_i is the particle multiplicity in the $i-$th cell, angle brackets denote averaging over the analyzed events, and r is the momentum order. The $F_r(M)$ equals one for all values of r and M, provided that the particle density across the subdivision space is uniform and that particle production processes are uncorrelated.

For the ideal gas of particles in the grand-canonical ensemble, these conditions are satisfied in the configuration space, where the particle density is uniform throughout the volume, multiplicity fluctuations are Poissonian, and particles are uncorrelated.

If the dynamics of the particle production is scale-invariant [24], that could be reflected in the power-law behavior of the SFMs [20], i.e, if the system is self-similar, factorial moments will follow a power-law dependence on momentum cell-width [20], [25]–[27]:

$$F_r(M) \simeq (M)^{\phi_r}, \tag{2.2}$$

where the intermittency indices ϕ_r for different orders will obey the linear relation:

$$\phi_r = (r-1)\cdot(d_r), \tag{2.3}$$

with d_r, the anomalous fractal dimension of the set formed by the order parameter density fluctuations, in other words, this last equation means that a cascade of self-similar fluctuations manifests itself in a power-law dependent on the moment's bin width. In Fig. 2.2 (*left*), a linear dependence of the logarithm of SFMs generated by the Power-law Model [28] as a function of the logarithm of M, while Fig. 2.2 (*right*) shows linear dependence of ϕ_r on r. Details of the Power-law model are covered in Sec. 4.5.

In summary, intermittency in the context of multiparticle production is defined as a power-law behavior of the normalized factorial moments of particle number distributions as a function of

decreasing cell size. If such power-law behavior were observed, it could indicate the existence of self-similar fluctuations in the underlying distribution.

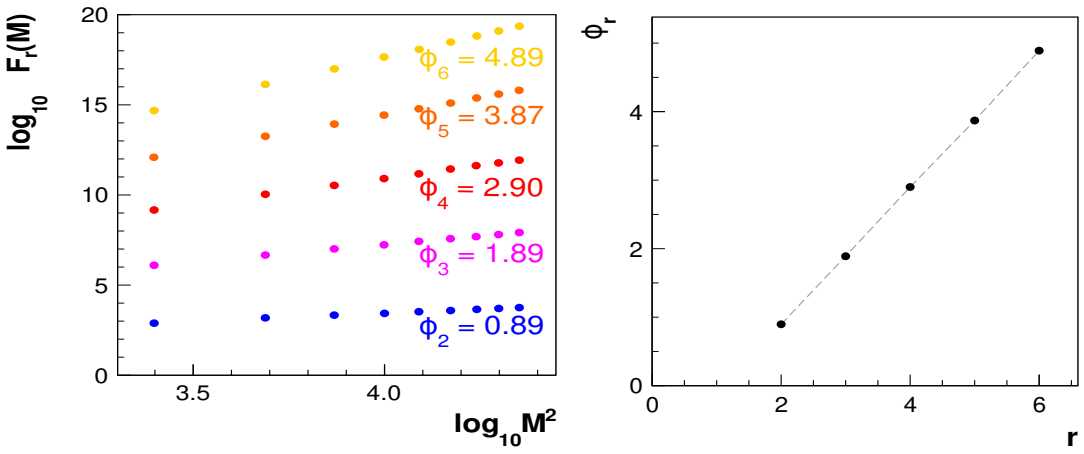

Figure 2.2: *Left:* The log-log plot of the SFMs of order $r = 2-6$ from Power-Law model [23] with intermittency indices (ϕ_{2-6}) values are shown. *Right:* Linear dependence of intermittency indices on the order of moments, r, is shown.

2.2.1 Intermittency and the search for the critical point

The current discussion has explored intermittency as a diagnostic tool within the context of multiparticle production analysis. However, this is a technique that is associated with the search for the critical point, as it was mentioned in Sec. 1.4. Let us talk about how these ideas are linked before continuing to the experimental discussion. Before advancing to the experimental section, this chapter will summarize the connections between the discussed concepts.

A couple of years after Białas and Pechanski published their ground-breaking work, J. Wosiek [25] found evidence of intermittent behavior in the critical region of the two-dimensional Ising model, raising the general question of whether or not intermittency and critical behavior are related. Wosiek investigated the presence of intermittency within the two-dimensional Ising model at its critical temperature. The primary objective was to determine whether such behavior manifests in statistical physics models, particularly during second-order phase transitions.

In the mentioned publication, Wosiek employs Monte Carlo simulations to analyze the two-dimensional Ising model[2]. To detect intermittency, Wosiek partitions the lattice into smaller subregions – or cells – and computes the magnetization within each cell. He then calculates the

[2]In brief, the Ising model is a mathematical representation used to describe ferromagnetism in statistical mechanics. In this model, discrete variables called "spins" can take values of +1 or -1 and are arranged on a lattice, interacting with their nearest neighbors. The system undergoes a phase transition at a critical temperature, where the macroscopic magnetization changes from zero (in the disordered phase) to a non-zero value (in the ordered phase).

SFMs of the magnetization distribution across these cells. The study reveals that at the critical temperature, the **SFMs exhibit a power-law dependence on the cell size**. This power-law behavior indicates self-similar fluctuations across different scales, a feature of intermittency. Wosiek's results suggest that as the system approaches the critical point, it displays complex, scale-invariant structures in magnetization fluctuations.

Shortly after, Helmut Satz proved that the critical behavior of the Ising model indeed leads to intermittency, with indices determined by the critical exponents [16]. The study concludes that intermittency is intrinsically linked to the critical behavior observed in second-order phase transitions. This implies that near the critical point, systems exhibit complex fluctuation patterns that are not apparent away from the critical point. Satz's findings provide a deeper understanding of the nuanced behaviors that emerge in statistical systems undergoing phase transitions.

One of the last breaking points, before igniting a considerable interest among the experimental strong interactions community, was in 1991. Again, Białas and Hwa, after the first set of published experimental results (see Sec. 2.3.1.1), proposed that analyzing particle number fluctuations in high-energy heavy-ion collisions can serve as an indicator for the formation of quark-gluon plasma [26]. They suggest that measuring anomalous dimensions in particle spectra derived from intermittency studies can signal the QGP formation and its subsequent hadronization phase transition.

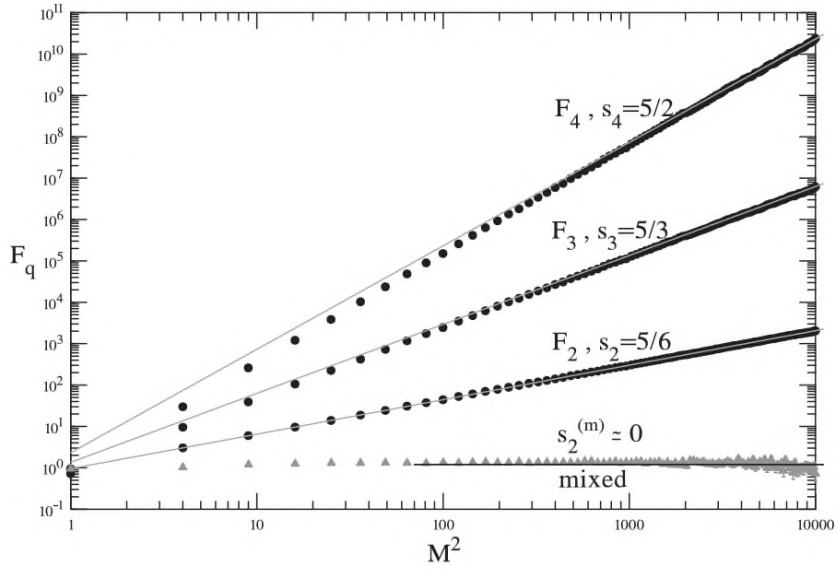

Figure 2.3: The log-log plot of the factorial moments of order $q = 2 - 4$ (solid circles) for an ensemble of 600 critical events generated by the Monte Carlo algorithm described in [29]. The corresponding theoretical power-law predictions are shown with solid lines.

As a result of these findings, researchers in different facilities began using SFMs to study particle

multiplicity fluctuations in high-energy collisions, aiming to explore the structure of the phase transition region. In 2006, N. Antoniou, F. Diakonos, A. S. Kapoyannis, and S. Kousouris in [29] investigated the phenomenon of critical opalescence within the context of QCD matter [3]. In this study, it was discussed that a similar effect, termed "critical intermittency," can be observed in high-energy nuclear collisions as a signature of a second-order phase transition in QCD matter.

Also in the same publication, it was stated that critical intermittency manifests in QCD matter produced during high-energy nuclear collisions, analogous to critical opalescence in conventional matter. This behavior is characterized by power-law patterns in factorial moments across all orders, particularly associated with baryon production. The study emphasizes that observing these power-law behaviors in transverse momentum spectra can serve as experimental signatures of the QCD critical point. Specifically, the analysis of baryon production and the isoscalar sector of pions (sigma mode) is highlighted as a key observable. Identifying critical intermittency patterns provides a set of observables to aid the experimental search for the QCD critical point in high-energy nuclear collision experiments.

This work bridges the concept of critical phenomena observed in conventional matter with the behavior of QCD matter under extreme conditions, offering a different approach to detecting phase transitions in high-energy physics experiments.

2.3 Experimental results of intermittency in heavy-ion collisions

The publication by Białas and Hwa [26] motivated several experiments at the CERN SPS to initiate the search for intermittency signals in the early 1990s. This line of investigation has continued through the 2000s and remains an active area of research in multiple international experiments to this day[4].

These studies use power-law fits to determine intermittency indices based on the cell size dependence of the SFMs. This section briefly reviews the most important results and the discussions they have generated.

The Table 2.1 provides a summary of the experiments, comparing the collision types, beam momenta, and approximate center-of-mass energies to facilitate a clear comparison of their scales. For consistency, all results discussed in this chapter will be presented in terms of beam momentum unless indicated otherwise. Intermittency results were not published in all the systems provided in this table. Where GeV/c refers to the momentum of an individual particle, such as pions in the case of NA22, while A GeV/c refers to momentum per nucleon in beams of heavy ions where A is the mass number of a nucleus (protons + neutrons).

[3] Critical opalescence refers to the increased scattering of light near a critical point of a phase transition, leading

Table 2.1: Experiment comparison, in the study of intermittency related to the phase diagram and search for the critical point, energy of collisions is compared in beam momenta and center of mass. Results discussed in this section will be commented on in the beam momenta.

Experiment	**Type of collisionn**	**Beam momenta**	$\sqrt{s_{NN}}$
EMU07 (CERN SPS)	A + Emulsión of (Pb, S, O + Em)	60–200A GeV/c	8–17 GeV
NA22 (CERN EHS)	$\pi^+ + p$, $p + p$	250 GeV/c	22 GeV
EMC (CERN SPS)	$\mu + p$, $\mu + A$	100–280 GeV (muons)	—
NA35 (CERN SPS)	p + A, O + A, S + A	up to 200 AGeV/c	17–20 GeV
WA80 (CERN SPS)	O+Au, S+Au	60, 200 AGeV/c	8–17 GeV
NA49 (CERN SPS)	p+p, p+Pb, C+C, Pb+Pb	up to 158 AGeV/c	6.3–17.3 GeV
NA61/SHINE (CERN SPS)	p+p, Be+Be, Ar+Sc, Xe+La, Pb+Pb	13A–150 AGeV/c	5.1–16.8 GeV
STAR (BNL RHIC)	p+p, d+Au, Au+Au	up to 100 AGeV	7.7–200 GeV

2.3.1 Early experimental results

2.3.1.1 EMU-07/KLM

In 1989, the Krakow-Louisiana-Minnesota (KLM) Collaboration at CERN analyzed data obtained from nuclear interactions coming from nuclear emulsions[5] of oxygen at 60A GeV/c and 200A GeV/c. An intermittent behavior of the fluctuations in the pseudorapidity phase space was observed in both beam interactions, as shown in Fig. 2.4 [30].

The proposed SFMs analysis was still in progress and needed to be understood. The KLM collaboration stated that the origin of the intermittent fluctuations remained unclear and represented a new challenge for both theoretical and experimental studies. The results were compared with Monte Carlo simulations; however, the models of multiparticle production (up to this day) do not predict intermittent behavior. On the other hand, it was pointed out that a *jet model* with a scale-invariant decay function was consistent with intermittent behavior; however, the source of this intermittent signal needed to be studied further.

to a milky appearance in fluids.

[4]Intermittency has also expanded to Cosmic Ray studies, but is not discussed in this thesis.

[5]EMU-07 is not a proper name of a collaboration, rather it was tracked to a SPS-CERN research program of nuclar emulsions this been number 7, having interactions of 60A GeV/c to 200A GeV/c ^{16}O and ^{32}S Nuclei in Light and Heavy Absorbers. Other key names for this experiment are IONS/KLM.

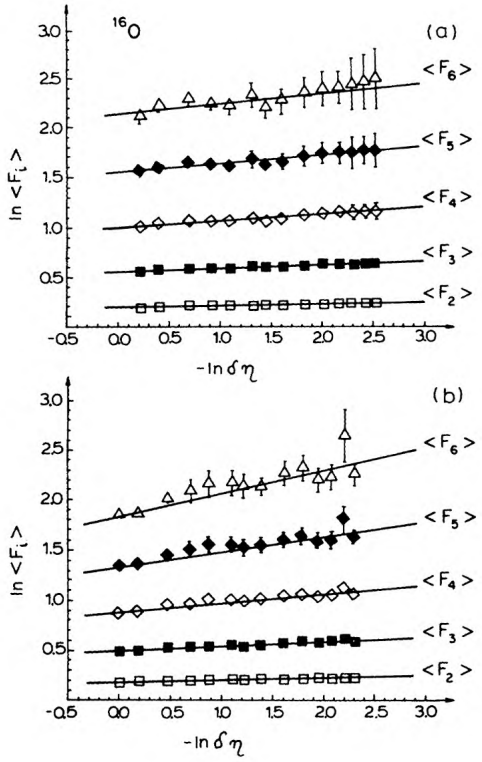

Figure 2.4: intermittency results from KLM collaboration, extracted from [30]. The dependence of the averaged moments of order 2-6 on the rapidity bin size for oxygen interactions at 60*A* GeV/*c* (*up*) and 200*A* GeV/*c* (*down*). Solid lines represent linear fits to the data. Plot taken from [30].

2.3.1.2 EHS/NA22

Intermittent behavior was observed $\pi + p$ and $K + p$ collisions at beam momentum 250 GeV/c and published in [31], (the results can be seen in Fig. 2.5), where the authors found an increase of the normalized factorial moments. The physics behind this increase was attributed to the jet cascading mechanism as the most likely interpretation. The fragmentation models used to compare with experimental data in the same publication do not (fully) reproduce the effect, suggesting that an improvement of the hadronization picture was needed.

2.3.1.3 EMC

The European Muon Collaboration (EMC) was a consortium of particle physicists formed in 1973 to study high-energy muon interactions at CERN. In 1990, the collaboration published the results of intermittency analysis in hadron production of muon-proton interactions at beam momenta 100-280 GeV/c [32]. The results present an intermittent behavior in the dependence of the SFMs on the 1D rapidity bin width. Results are displayed in Fig. 2.6.

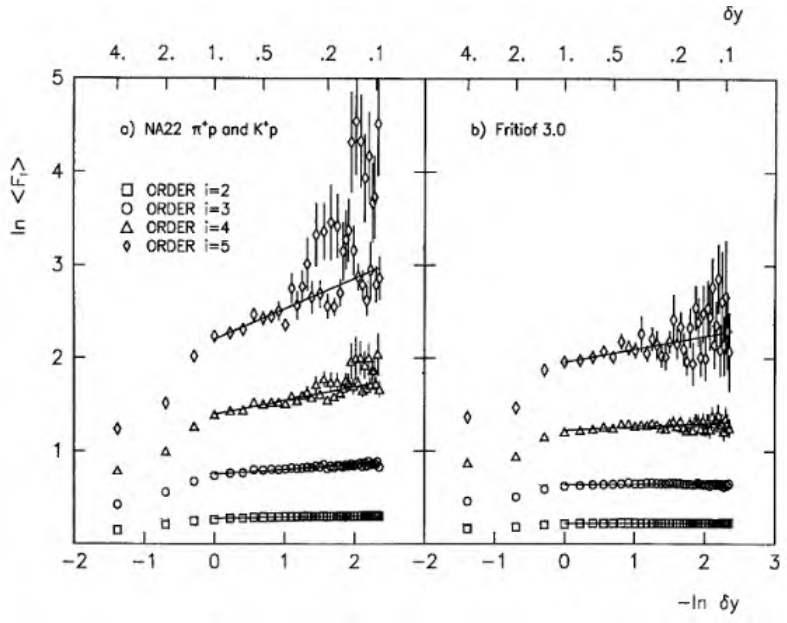

Figure 2.5: Intermittency results for EHS/NA22. Double logarithm plot of SFMs as function of rapidity, $In\langle F_i\rangle$ vs $In\ \delta y$ for *(left)* $\pi + p$ and $K + p$ collisions at 250 GeV/c and *(right)* the expectations from FRITIOF 3.0 simulations. Image taken from [31].

Białas and Seixas interpreted this outcome as a consequence of the projection procedure, which averages out fluctuations [33]. They proposed that, moving forward, factorial moment analysis should be conducted in three dimensions as a standard approach when investigating critical behavior.

2.3.1.4 NA35

Following the first discussion, and motivated by previously published results, the NA35 experiment at CERN SPS also analyzed SFMs' behavior within the frame of their strong interactions program using nucleus-nucleus collisions, proton-gold, oxygen-gold, sulphur-gold, and sulphur-sulphur collisions at 200*A* GeV/*c* beam momenta. The reported results of intermittency done in the (y, ϕ, p_T) phase space [34], using two methodologies, include an increase in factorial moments with the number of subdivisions of phase space. Still, this power law did not accurately describe the rise. These results (see Fig. 2.7 were key motivations for further experimental studies, alongside other reports from the same collaboration in the studies of the structure of the phase transition region.

2.3.1.5 WA80

Negative results on intermittency have also been reported. The WA80 collaboration analyzed SFMs on S+S and S+Au collisions in one- and two-dimensions [35]. For all systems studied,

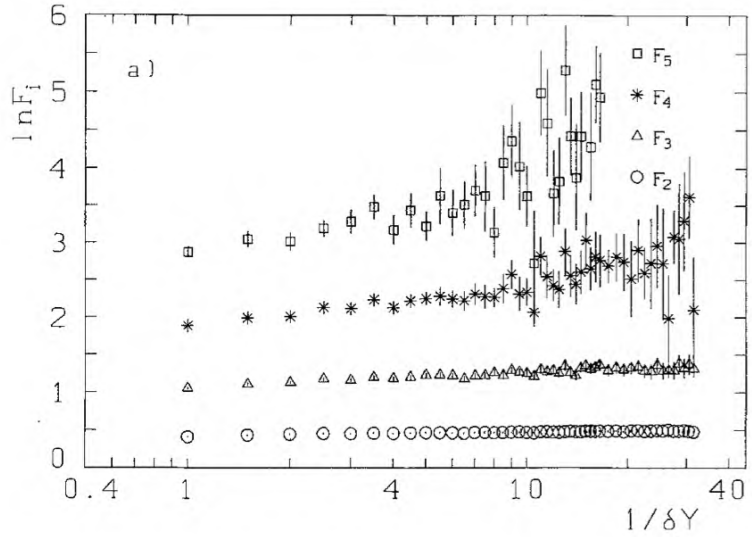

Figure 2.6: Measured SFMs F_i from EMC in [32] $F_i(i = 2,3,4)$ as functions of the inverse bin width for positive hadrons in the rapidity interval $-3 < y < 3$.

comparisons with predictions of the FRITIOF event generator coupled with a detailed model of the WA80 detector show no observed correlated particle emission beyond that predicted by FRITIOF.

2.3.2 Contemporary results

Despite the assertions of the KLM, EMC, and NA22 collaborations, the original author of the SFMs' analysis addressed two interesting perspectives of these results that should not be ignored, and was crucial in the discussion of the results of the present thesis. The main conclusions are summarized below:

After the experiments reported an approximate power-law behavior of normalized factorial moments, as predicted by the hypothesis of intermittency, it was considered that the first statements in the study of factorial moments were premature, and more complete measurements were needed to determine the actual size and range of fluctuations in article spectra. Białas and Seixas showed in [33] that projections of two- or three-dimensional intermittent distribution in momentum space on rapidity and/or azimuthal angle, lead to a dramatic reduction of intermittency parameters and to deviations from the power-law behavior at very small intervals. Implementing this idea could result in the effects seen in joint rapidity and azimuthal angle spectra. This can be interpreted as evidence that the effect may be much stronger when measured in the whole 3-dimensional momentum space.

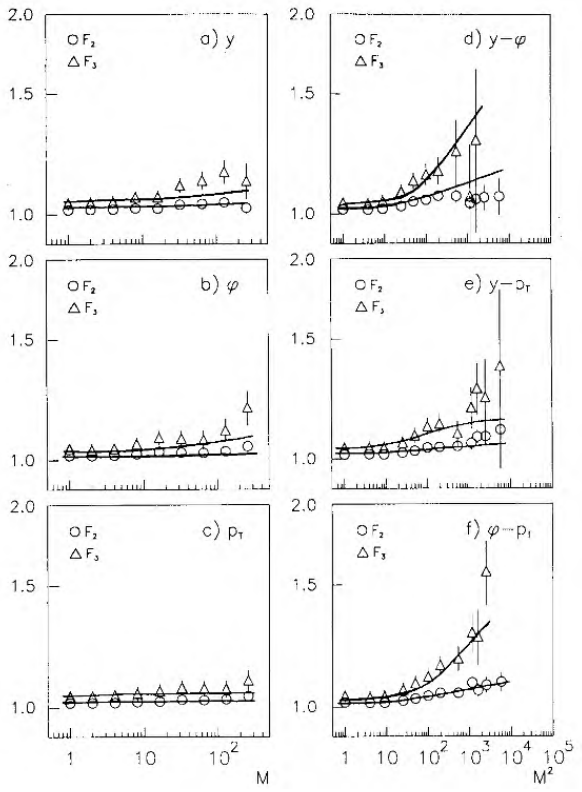

Figure 2.7: Intermittency results from NA35. Log-log plots of the corrected normalized factorial moments F_q vs the number M^d of cells for negative hadrons in O-Au collisions, in one dimension a) y, b) ϕ, c) p_T; and in two dimensions $y-\phi$, e) $y-p_T$, f) $\phi-p_T$ f. The curves show the results from the MC calculation. Figure extracted from [34].

The results to be summarized in this section share the main goal: to search for the critical point of strongly interacting matter. Advocating to find the predictions in [29], SFMs have been used to look for a power-law behavior. However, it was pointed out recently in the Quark Matter 2025 conference that existing collaborations in the heavy-ion community have results that do not agree with each other, and an effort should be made to achieve consistency in the way SFMs are studied [36].

2.3.2.1 NA49

The NA49 experiment at the CERN SPS initiated its investigation into the critical behavior of strongly interacting matter in 2000. Its findings on the analysis of SFMs, aimed at locating the critical point, represent a cornerstone in this area of research. NA49 explored signals of intermittency in the production of low-mass $\pi^+\pi^-$ pairs [37] and protons [38] during central collisions at mid-rapidity for systems such as C+C, Si+Si, and Pb+Pb at a beam momentum of 158A GeV/c. The experiment measured the second scaled factorial moment $F_2(M)$ and addressed the problem of interference from a background of misidentified and non-critical protons using the

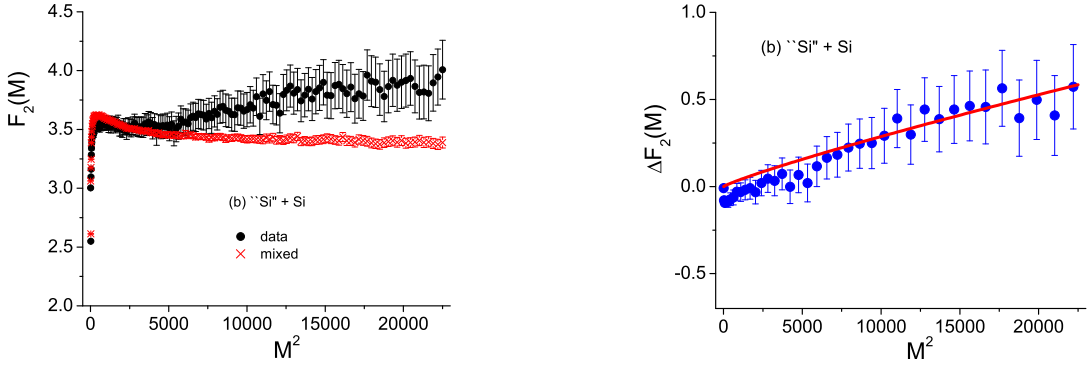

Figure 2.8: Results for proton intermittency analysis of NA49 in transverse-momentum space at forward rapidity ($-0.75 < y < 0.75$) for central collisions of Si+Si at 158A GeV/c. *Left*: Results of $F_2(M)$, the black circles represent $F_2(M)$ of the data, and the red crosses represent the mixed events. *Right* the background subrsacted moments $\Delta F_2(M)$, for the same collisions, a power-law fit for $M^2 > 6000$ with an exponent of 0.96 is shown. Figures were extracted from [37].

mixed event method. The background-subtracted moments are defined in this publication as:

$$\Delta F_2(M) \approx F_2^{\text{data}}(M) - F_2^{\text{mix}}(M), \tag{2.4}$$

and analyzed as a function of M^2. Fig. 2.8 presents the results for the second scaled factorial moment F_2 of the $\pi^+\pi^-$ pair multiplicity distribution as a function of the number of subdivisions in transverse-momentum space. These pairs were selected from the forward rapidity region ($y \geq 0.5$). In the case of Si+Si collisions, a power-law increase was observed, characterized by an exponent $\phi = 0.33 \pm 0.04$. This extracted value suggests a notable intermittency effect; however, it remains below the theoretical prediction for the critical point, $\phi_2 = 0.67$. It should be noted that no investigation of potential systematic biases was carried out.

While in proton intermittency analyses on C+C and Pb+Pb collisions, there were no intermittency signals obtained, the results for Si+Si for $\Delta F_2(M)$ were fitted to a power-law in the region $M^2 > 6000$. The result found was $\phi_2 = 0.96^{+0.38}_{-0.25}(stat) \pm 0.16(syst)$ with $\chi^2 = 6/d.o.f \approx 0.09 - 0.51$. This fit is consistent with the critical point predictions.

2.3.2.2 STAR

One of the primary motivations for this thesis is the results obtained by the STAR collaboration. These results were discussed within a closed "task-group-force" between NA61/SHINE and STAR before 2021, and opened an intriguing discussion between collaborations that continued the studies independently.

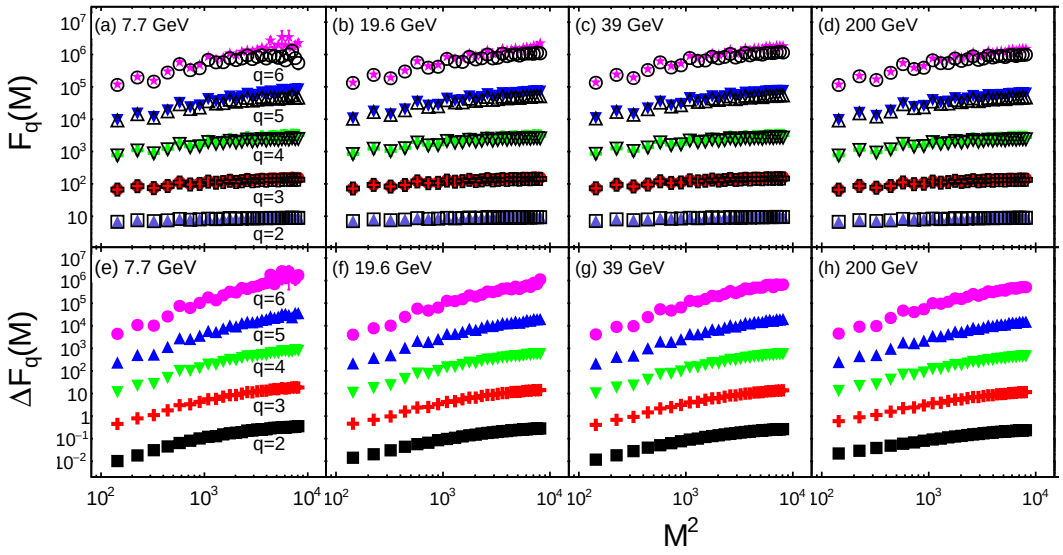

Figure 2.9: STAR collaboration results on intermittency. (*top*) SFMs F_r(r=2-6) of identified charged hadrons ($h^{\pm}$) multiplicity in central Au+Au collisions at four example energies. Solid(open) markers represent $F_r(M)$ of data (mixed) events as a function of M^2. (*bottom*) Results for $\Delta F_r(M)$ of the same data set as a function of M^2 in double-logarithmic scale. Plots from [39].

The STAR collaboration is looking for the QCD critical point at RHIC, as part of their BES-II agenda [39] using intermittency analysis of *all charged particles* within a pseudorapidity interval $|\eta| < 0.5$ in Au+Au collisions in a wide energy range from $\sqrt{s_{NN}} \approx 7.7 - 200$ GeV and reported in 2023 in Ref. [39] using a modified version of the NA49 definition:

$$\Delta F_r(M) \approx F_r^{\text{data}}(M) - F_r^{\text{mix}}(M). \tag{2.5}$$

Many intriguing discussions were born from these results. Figure 2.9 $(a)-(d)$ shows $F_r(M)$ [6] of data and mixed events corrected for reconstruction efficiency for $r = 2-6$ in the range of M^2 from 1 to 100^2 in the most central (0-5%) collisions at $\sqrt{s_{NN}} \approx 7.7 - 200$ GeV. At the bottom, we see the results for the same data set but for $\Delta F_r(M)$ for $r = 2-6$; these results are significantly larger than zero in the large M^2 region where the increase starts slowing down for $M^2 > 4000$. Originally, this unusual intermittency-like pattern was interpreted as potentially related to the critical point. However, in the report's conclusions, the collaboration suggests that the observed increase in $\Delta F_r(M)$ warrants further investigation.

[6] Note that $F_i(M) = F_r(M) = F_q(M)$ and $i = q = r$. There is an inconsistency in the selection of subindices. Still, meaning remains the same as pointed out before.

It is important to note that a formal definition or derivation of SFMs for higher-order moments of $\Delta F_r(M)$ in eq. 4.8 was never performed in a proper mathematical way. The original formulation of eq. 4.8 was developed in the context of proton-pair intermittency and specifically for $\Delta F_2(M)$ [37], [40]. Consequently, the calculations performed by the STAR collaboration are based on an intuitive extension of eq. 4.8, assuming that the same relation remains valid for $r > 2$. Nonetheless, this does not exclude the possibility of locating the critical point using this approach. This, in turn, reintroduces a question that remains unaddressed: why does $\Delta F_r(M)$ exhibit an increasing trend? Is it perhaps a similar physics as the one reported in rapidity intermittency analyses? Or is there another physical causation not discussed previously?

2.3.2.3 NA61/SHINE: a different approach

NA61/SHINE can be regarded as the direct successor to the NA49 experiment, not only due to the continuity of personnel (many of whom were trained within NA49 before contributing to other collaborations) but also because the experimental facility itself evolved into what is now NA61/SHINE. This will be discussed in greater detail in Chapter 3.

Latest intermittency results of NA61/SHINE are done using as a ground base the results of NA49, doing proton intermittency analysis, instead of $\pi^+\pi^-$. These results have been reported in [23], [41]. In summary, the results include two approaches. The methodology used in the NA49 experiment for background subtraction from eq. 4.8, as well as the implementation of *a new variable to study intermittency: Cumulative variables*. M. Gaździckiproposed this idea in [42]. This methodology will be fully covered in Chapter 4.1.3.

In brief, instead of using p_x, p_y phase space it is proposed to use cumulative quantities Q_x, Q_y, this transformation have the following features: it transforms any distribution into uniform one and removes the dependence of $F_r(M)$ on the shape of the single-particle distribution, but the intermittency index of an ideal power-law correlation function remains approximately invariant [43].

In response to the challenges associated with calculating $\Delta F_r(M)$ for higher-order moments, as well as the difficulty of properly excluding contributions from non-critical sources that may lead to fake-intermittency or constitute noise, the use of cumulative variables provides an effective solution.

In the latest time, and since the Critical Point and Onset of Deconfinement Workshop in 2024 [44], the results displayed using this methodology are called **cumulative p_T binning** and are shown as:

$$\Delta F_r(M)_c = F_r(M) - F_r(1)$$

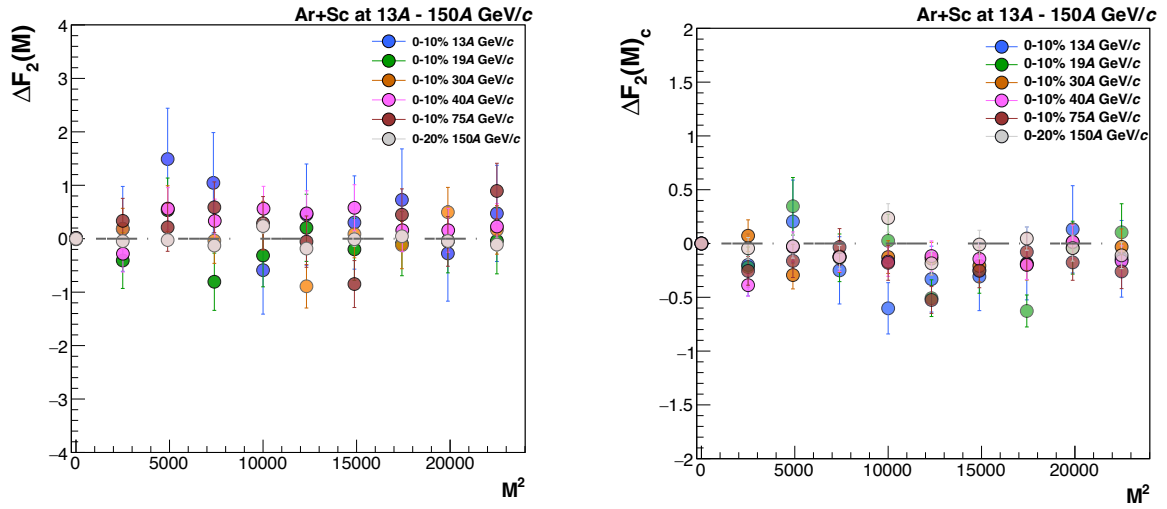

Figure 2.10: Extracted from [23], [41]. Results of proton intermittency analysis of central Ar+Sc collisions at 13A – 150A GeV/c beam momenta for the NA61/SHINE. On *left* Results for p_T binning. On *right* Results for cumulative p_T binning.

where $F_r(M)$ and $F_r(1)$ are calculated by employing the cumulative $\mathrm{p_T}$ binning. $F_r(1) = F_r(M)$ for uncorrelated particles in $\mathrm{p_T}$.

The results of proton intermittency analysis (with a very similar methodology as the one followed in this thesis) come from central Ar+Sc collisions from 13A–150A GeV/c in beam momenta, an adapted version of the results is shown in Fig. 2.10 where the results using just p_T *binning* and *cumulative* p_T *binning* show one final outcome: none of the results show a power-law behavior or increase with M^2.

2.3.3 Results discussion

Although this chapter may seem like an unconventional historical overview of experimental intermittency studies, it serves an important purpose. The discussion begins with early findings on rapidity intermittency, particularly the proposal by Białas and Seixas [33] to extend the analysis from one to two dimensions. However, their contributions go beyond this.

1. The Handbury-Brown-Twiss effect

In the mid-1990s (1994 and 1996), Białas and collaborators reignited a less frequently acknowledged debate. They explored alternative explanations for intermittency observed in experiments such as NA22 and EMU, proposing that Hanbury Brown–Twiss (HBT) correlations, rather than critical phenomena, could account for the rise in SFMs [45], [46].

It is discussed in the 1994 publication [45] and summarized in Sec. 2.3.1 that there was strong evidence for power-law behavior in momentum spectra across various high-energy processes, which potentially points to a universal scaling feature. The early results suggest that the exponents of intermittency appear to be process-independent. At the same time, short-range correlations between identical pions offer insight into the size of the particle-emitting source. These observations challenge the assumption that intermittency and the HBT effect are unrelated. Instead, they suggest that there is compatibility between the two, reflecting scale-invariant fluctuations in the interaction region.

This implies that intermittency parameters should vary between identical and non-identical particles. Experimental data from NA22 and EMC reinforce this, demonstrating a power-law in like-charge particle correlations. Despite HBT accounting for much of the short-range structure in momentum space, unexpectedly large source-size fluctuations persist. If HBT drives the intermittency, the interaction volume must fluctuate following a power-law distribution.

Further insight comes from Tadeusz Wibig's 1996 study [46], which linked Bose-Einstein correlations with intermittency. He emphasized the central role of the particle-emitting source in shaping both SFMs' behavior and HBT effects. The study critiques the standard exponential Bose-Einstein parametrization, tracing it back to string fragmentation models, and explores two- and three-particle correlations. Simulations without Bose-Einstein symmetrization reveal that applying full-event symmetrization can artificially enhance small-bin correlations, suggesting it may overstate the actual effect.

It wasn't until 2006, A. Białas [47], discussed the relation between intermittency and Bose-Einstein correlations was discussed, starting from the point that intermittency, at its core, seeks evidence of self-similarity in particle spectra. While exact self-similarity is unattainable, the challenge lies in defining it statistically and identifying its presence through resolution-

dependent studies. Power-law behavior in factorial moments and cumulants [14], [15] signals such self-similarity.

From the discussion of the first experiments, some have concluded that HBT correlations fully account for intermittency. However, while HBT effects explain short-range correlations in momentum space, they do not account for the defining feature of intermittency: power-law scaling and self-similar structures. Explaining this behavior requires understanding how the geometry of the emission region in configuration space gives rise to such scaling in momentum space. Achieving that power-law behavior in momentum space implies a similar structure in configuration space. However, a pure power-law over the whole phase space will lead to non-normalizable distributions, necessitating modifications that introduce theoretical ambiguities.

Brax and Peschanski [48] in 1994 applied Lévy distributions to momentum spectra, obtained key relations for intermittency exponents, and also proposed that configuration space follows a stable (Lévy) distribution, potentially due to QCD cascades governed by renormalization group constraints [49], [50].

In recent years, specifically 2024 and 2025, the fact that the scaling behavior is not uniquely tied to critical phenomena has been studied in depth in the context of the STAR intermittency results. Suggesting that the pattern observed emerges more generally as a consequence of the phase-space partitioning procedure intrinsic to the analysis [51].

In this last-mentioned study, it is stated that the division of phase space into progressively finer bins naturally induces a power-law-like behavior in SFMs. Even in the absence of critical dynamics, a localized cluster of correlated particles confined within a single bin can produce an "intermittency-like" enhancement in $\Delta F_q(M)$. For sufficiently small bin sizes $\Delta^2(M)$, the multiplicity within a cluster of characteristic size exhibits scale-invariant behavior, manifesting as a simple power-law.

It was also discussed that density fluctuations within phase-space cells naturally give rise to the power-law-like behavior observed in SFMs. [52] A correlated cluster of particles localized within a single cell can produce an "intermittency-like" enhancement in $\Delta F_q(M)$ because the behavior of these moments is governed by both the multiplicity distribution within a cluster and the spatial distribution of particles in transverse momentum space.

Whether any of these simplified mechanisms can account for the wide range of experimental intermittency patterns remains an open question. Addressing this requires further investigation through dynamical modeling of heavy-ion collisions.

CHAPTER 3

NA61/SHINE EXPERIMENT

The NA61/SHINE experiment [53], [54] (SPS Heavy Ion and Neutrino Experiment) is a fixed-target facility located in the **North Area** of the **Super Proton Synchrotron** at CERN. It was designed to study hadron production in a wide range of collision systems and energies. Thanks to its large rapidity acceptance and coverage of low transverse momentum, NA61/SHINE is well suited for investigating heavy-ion physics, neutrino beam properties, and cosmic-ray interactions.

Since the beginning, the experiment's physics program has grown significantly. It now supports a variety of research goals, including input for long-baseline neutrino experiments and air-shower modeling for cosmic-ray studies. All the developments have been made possible by steady upgrades to the SPS accelerator complex and beamlines. The experiment is expected to continue operating at least until September 2026, a few months after the start of CERN's accelerators Long Shutdown 3 (LS3) [55]. [1]

This chapter introduces the main goals of the physics program and describes the detector systems and reconstruction methods used in this analysis, with a focus on the Xe+La data-taking setup.

3.1 Physics heavy-ion program

Fixed-target experiments like NA61/SHINE offer significant advantages in the study of heavy-ion collisions in comparison to hadron colliders. Their broad rapidity coverage and sensitivity to low transverse momentum particles allow for detailed investigations of the strong nuclear force, as well as research in neutrino physics and cosmic-ray interactions. While the latter two topics are

[1] LS3 calendar was consulted for the last time in September 2025.

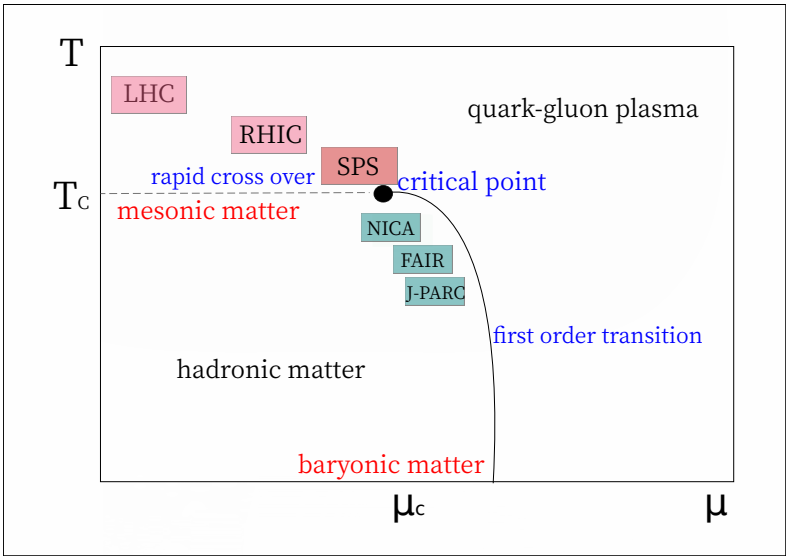

Figure 3.1: A sketch of the phase diagram of strongly interacting matter with current (red) and future (green) experiments studying the transition region of strongly interacting matter.

not the primary focus of this thesis, recent results of those topics reinforce the broad scientific scope and impact of the experiment [56], [57].

The strong interaction program of NA61/SHINE was initially framed by findings from earlier experiments such as KLM, EMC, and NA49 (see Sec. 2.3.1). As introduced in Chapter 1, one of the central questions in modern nuclear and particle physics is the structure of the phase diagram of strongly interacting matter. While the existence of QGP has been confirmed through extensive theoretical and experimental work – based on data from $A+A$ collisions at the LHC, SPS, and RHIC – the nature of the transition between the hadron gas phase and the QGP remains unresolved. In Fig. 3.1, a sketch of the phase diagram of strongly interacting matter is shown; the red labels indicate the regions explored by the early stage of heavy-ion collisions in current experimental programs, while the green labels refer to regions targeted by future programs.

In particular, identifying the structure of the transition region and the possible location of a critical point remains a significant challenge. As discussed in Chapters 1 and 2, previous studies using scaled factorial moments revealed fluctuations in particle multiplicities that hinted at critical phenomena (see Sec. 2.3.1). These results strongly motivated NA61/SHINE to conduct a systematic scan across beam energies and system sizes [58]. The goal of this extended program was to help clarify the nature of the phase transition region and to search for direct evidence of the critical point in strongly interacting matter.

This two-dimensional scan varies the size and energy of the collision system [59] the completed scan is shown in left of Fig. 3.2, the scan was performed in the range of 13A–150A GeV/c beam

momenta; the right the panel displays the chemical freeze-out points of nucleus-nucleus collisions studied with the NA49 and NA61/SHINE strong interactions programmes at SPS. The experiment studies the interactions of different-sized nuclei, ranging from small $p+p$ to heavy nuclei. The data analyzed in this thesis corresponds to the collected data of Xe+La interactions in 2017.

The structure of the transition region is explored by studying the final states produced in nucleus-nucleus collisions with these variations of collision energy and sizes of colliding nuclei. As the collision energy rises, the number of pions produced per colliding baryon increases, leading to a decrease in the baryon chemical potential (μ_B). When the size of the colliding nuclei grows, the volume of the created matter becomes larger, making hadron-hadron interactions more important during the later stages of evolution. This increased interaction lowers the freeze-out temperature as the system size increases. By scanning across different collision energies and system sizes, researchers aim to position the freeze-out conditions closer to the phase transition region of strongly interacting matter, as can be seen on the right of Fig. 3.2.

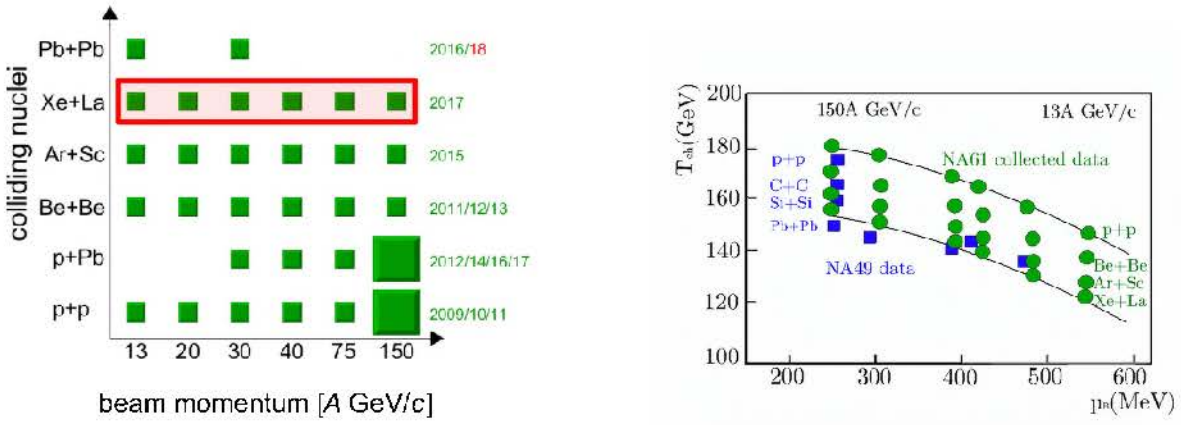

Figure 3.2: (left) Overview of NA61/SHINE 's system size and collision energy scan. The boxes display the data collected, and the large boxes indicate systems for which extensive statistics were obtained. The Xe+La data sets marked in red were studied for this thesis. (right) Display of the chemical freeze-out points of nucleus-nucleus collisions studied within the NA49 and NA61/SHINE strong interactions programmes at SPS. Images adapted from [58], [59].

The search for the critical point in nuclear collisions is promising only at energies above the onset of deconfinement, which occurs at low SPS energies [60], [61]. This is because the energy density needed for deconfinement at the collision's early stage is higher than the freeze-out energy density relevant for detecting the critical point. Near a second-order phase transition like the critical point, the correlation length diverges, making the system scale invariant and causing large, characteristic fluctuations in particle multiplicity. Other system properties are also expected to be sensitive to this region. Detecting the critical point involves scanning the phase diagram for regions with increased fluctuations. However, studying fluctuations is more

challenging than analyzing single-particle spectra or mean multiplicities, as conservation laws, resonance decays, volume variations, and limited experimental acceptance influence particle fluctuations and correlations.

The current scope of the strong interactions program of NA61/SHINE, has evolved, after the LS2 of CERN accelerators in 2018-2021, the NA61/SHINE experiment was upgraded [59], [62] and continues taking new measurements at CERN SPS, focussing now on the open charm hadron production in Pb+Pb collisions [63], [64], nuclear fragmentation cross sections for cosmic ray physics [57] and hadron production in hadron-induced reactions for neutrino physics [56]. After the planned LS3 in 2026-2028, NA61/SHINE will continue working with a new Light Ion program [65].

3.2 Facility

This section describes the principal components of the NA61/SHINE detector, step-by-step, and how the data is collected. Details concern only the data-taking campaign of Xe+La in 2017. An overall view of the detector can be seen in Fig. 3.3.

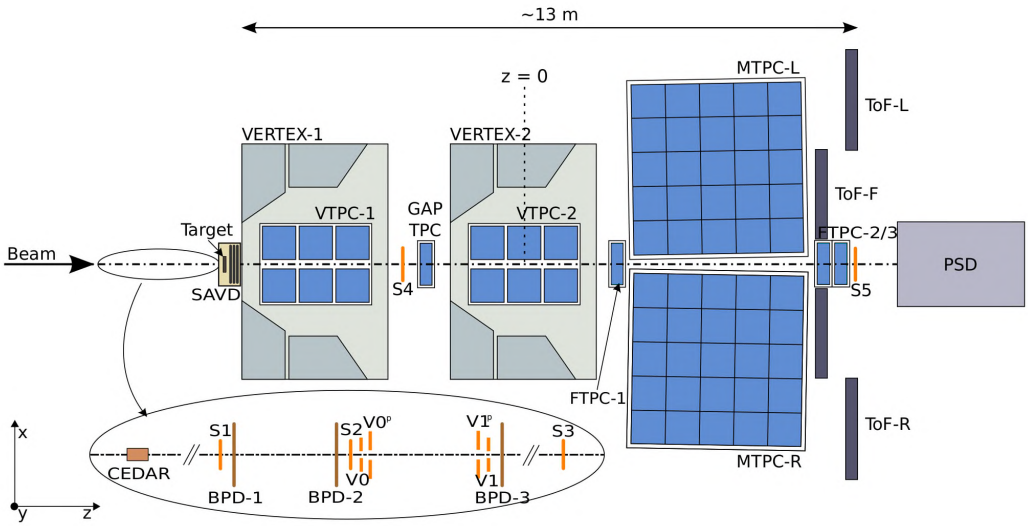

Figure 3.3: Overview of NA61/SHINE detector setup as for 2017. (not to scale).

3.2.1 Beamline and the ion-accelerator chain

In NA61/SHINE, the ability to perform a systematic energy and system size scan was only possible thanks to the flexibility of the SPS accelerator chain and the customized beamline setup delivering various nuclei at different energies. Knowing the beam and target descriptions

is essential to accurately reproduce and simulate events, as well as interpret fluctuations or systematics in the results.

The CERN accelerator complex provides NA61/SHINE primary and secondary beams of various ions. The SPS provides a beam at six momenta 13A, 19A, 30A, 40A, 75A, and 150A GeV/c; the designated beam line that delivers to NA61/SHINE is the H2 beamline [66] that was designed for the maximal SPS momentum (150A GeV/c), the minimum value provided (13A GeV/c) is dictated by the beam stability and quality that the H2 beamline requires.

The beams of ions go through several acceleration steps to achieve the requested momentum in the SPS accelerator. Afterward, they are extracted to the North Area and delivered to NA61/SHINE. This process is known as the ion accelerator chain.

The starting point is at the Electron Cyclotron Resonance (ECR), where repetitive microwave pulses accelerate the ions. Then, the ions are electrostatically extracted into the separator, which selects the particular charge state depending on the beam type, and right after the separator, the momentum of the beam is raised to 250A keV/c by the Radio Frequency Quadrupole (RFQ).

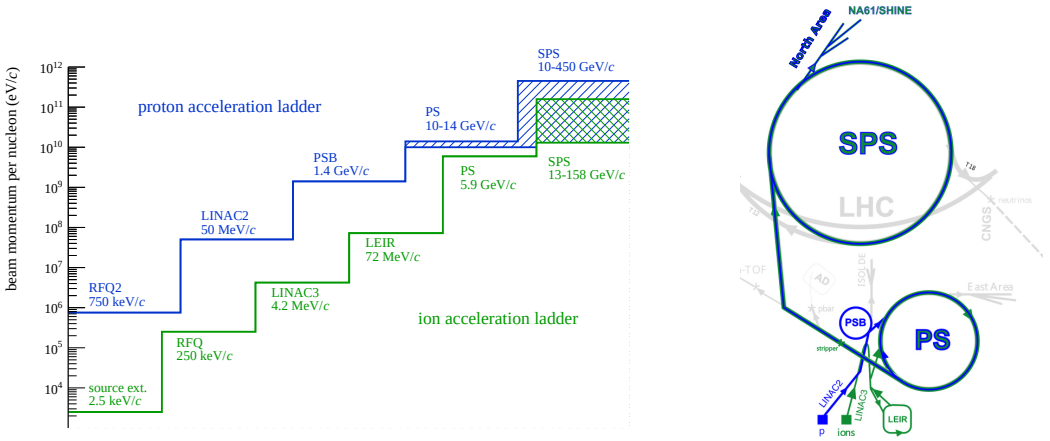

Figure 3.4: *(Left)* Diagram of the SPS accelerator chain, final destination is NA61/SHINE, in CERN North Area. *(Right)* Representation of beam values steps, as they get accelerated in the Ion accelerator chain, and delivered to NA61/SHINE.

The next step is CERN's linear accelerator (LINAC3), which increases the beam momentum to 4.2A MeV/c. The beam is then injected into the Low Energy Ion Ring (LEIR), in which it reaches the momentum of 72A MeV/c and is passed on to the Proton Synchrotron (PS); here, the ion beam is accelerated even more, up to 5.9A GeV/c and is extracted to the SPS, where the final acceleration takes place. The beam reaches a momentum of up to 150A GeV/c and is extracted to the North Area, and in the case of NA61/SHINE, the beam will be delivered in the H2 beamline.

The H2 beamline delivers the beam using a pair of large spectrometers. The beamline selects a beam type based on its rigidity, allowing the production of secondary hadrons and ions. Downstream collimators lower the beam intensity and then collect precise information on the beam's position, intensity, and profile [66].

3.2.1.1 The Xe+La data taking campaign

The choice of beam and target is crucial in any data-taking campaign, as it directly impacts the type, quality, and scope of the physics measurements possible (see Fig. 3.2, right). The Xe+La collisions represent a key component of NA61/SHINE 's strong interaction program. To support this, from October to December 2017, the experiment recorded Xe+La collisions at six different beam momenta, enabling a two-dimensional scan across nuclear mass and collision energy.

The Xenon beam

Before 2016, the SPS provided mainly lead (Pb) and argon (Ar) ion beams. In 2017, a new ion species, ^{129}Xe, was successfully commissioned and delivered to several CERN facilities. These included NA61/SHINE for fixed-target experiments, the LHC for Xe+Xe collisions, UA9 for Gamma Factory studies, and the PS for the CHARM irradiation facility [67].

The ^{129}Xe beam was produced by ionizing xenon gas using an ECR ion source. In this process, electrons are stripped from xenon atoms to form positively charged ions. The ion source utilizes strong electric fields or plasma to efficiently remove electrons, generating a stable beam suitable for acceleration and delivery to the experiment, as discussed in the previous subsection.

The Lantanum target

The ^{139}La target used in the Xe+La data-taking campaign in NA61/SHINE consisted of a stack of three lantanum plates of $25 \times 25 \times 1$ mm^3. The material was obtained by the collaboration, originally in 2014, and stored under a nitrogen atmosphere until 2017. Prior to the data-taking period, three smaller targets were cut from the least oxidized regions and installed in a helium-filled box inside the detector, as shown in Fig. 3.3.

After four weeks of beam exposure, a visual inspection revealed white oxidation on the target surface and traces of lanthanum oxide powder below the target. No intervention was made, and data taking continued until the end of the run, when significant oxidation had occurred. However, a second batch of lanthanum was purchased with the exact measurements, but these vacuum-packed plates appeared more oxidized than the initial ones and were not used. Later purity tests confirmed their inferior quality [68].

The data of the collisions was taken using two target configurations: target inserted (target IN) and target removed (target OUT); approximately 90% of the accumulated statistics were collected

with target IN [69].

3.2.2 Detectors

The following subsection provides a concise overview of the key components of the NA61/SHINE facility that were employed during the 2017 Xe+La data-taking campaign, with a summary of the subsystems directly relevant to the analysis presented in this dissertation. The description provided corresponds only to the mentioned data-taking campaign and might vary for other NA61/SHINE analyses, as well as being different from data taken after the CERN LS2. The detectors are described in terms of their function and role within the experimental setup, highlighting how each contributed to event reconstruction and data quality.

Beam detectors and trigger counters

Beam Position Detectors (BPDs), as the name suggests, precisely measure and monitor the position and trajectory of the particle beam as it travels toward the target in a particle physics experiment. Other important issues that BPDs focus on are:

- Beam alignment and steering: ensure the beam is always centered and aimed at the target; the lack of this could lead to inefficient collisions.
- Event-by-event tracking: to record the position of the beam for each event, information that is crucial for data reconstruction during data analysis
- Quality control of the beam: BPDs detect instabilities of the beam path in real time.
- Improve detector performance: an accurate knowledge of the beam position allows a better detector acceptance and calibration.

NA61/SHINE has three gaseous BPDs, filled with a gas mixture made of Ar and CO_2, and they are located along the beamline upstream of the target, as shown in Fig. 3.5. Each BPD consisted of two orthogonal planes of readout strips that allowed for position measurement in the x-y plane. This measurement can extrapolate the trajectory of beam particles to the target z-plane. See Fig. 3.6

In addition to the BPDs, NA61/SHINE uses scintillator detectors and counters; these detectors are used to identify specific types of events or conditions in real time and generate information to decide whether to record the data from a given particle collision. They generate a *trigger signal* when a predefined set of criteria is met. These devices detect charged particles by converting their energy loss into light, which is then measured by photomultiplier tubes (PMTs).

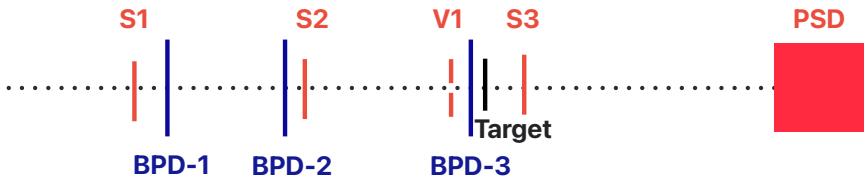

Figure 3.5: Schematic diagram of the beam counters used in ^{129}Xe+^{139}La data-taking campaign in 2017

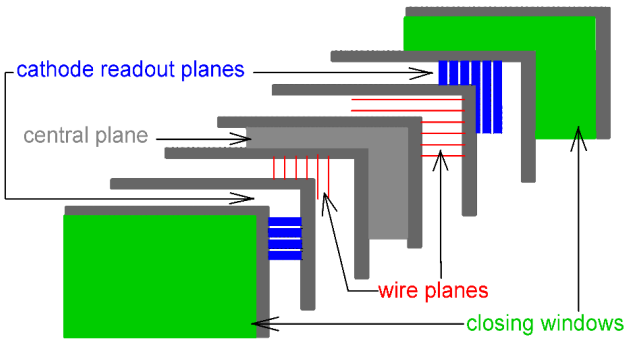

Figure 3.6: Schematic layout of the BPD detector.

The NA61/SHINE setup included three scintillating detectors (S1, S2, V1) located on the beamline upstream of the target as indicated in Fig. 3.5 and one scintillator counter (S3) placed downstream of the target. In brief:

- **S1, S2** capture the signals for readout and trigger electronics, providing precise timing for the experiment.
- **V1:** is known as a veto counter, a scintillator detector used to exclude unwanted events. The goal of the veto detectors is to allow the triggering only on the central part of the beam, therefore removing the beam halo. It consists of a plastic scintillator with a small hole in the middle.
- **S3:** is an interaction counter, and also a veto counter. They are placed downstream of the target to detect interactions of the beam particles. The interaction between the last counter running in coincidence and the given interaction counter is signaled by the absence of the beam particle signal in this counter. Hence, to detect interactions, these counters are used in anti-coincidence (veto) mode in the trigger logic.

In summary, the BPDs and scintillator counters ensure the precision and reliability of data collection in NA61/SHINE. The BPDs provide accurate spatial information about the incoming beam particles, while the scintillators define the timing and nature of each desired event. And their signals are key to the complete trigger system.

Time Projection Chambers

A Time Projection Chamber (TPC) is a type of gas detector used in particle physics to track charged particles in three dimensions. It is a commonly used detector in particle physics due to its large acceptance and detailed spatial resolution. It is primarily used for reconstruction of particles with high precision or *tracking*, momentum measurement, particle identification using dE/dx, and event reconstruction.

A TPC operates by detecting the ionization caused by a particle that passes through the gas-filled volume. As the particle travels, it ionizes the gas along its path, producing free electrons. These electrons drift under a uniform electric field towards a readout plane that is typically composed of pads or wires located at the end of the chamber. The time it takes for the electrons to reach the redout plane, combined with its position, allows for a very accurate reconstruction of the particle's trajectory. Additionally, if the amount of energy lost per unit length (dE/dx) during ionization is measured, the TPC can provide information for identifying the type of particle that produced the track.

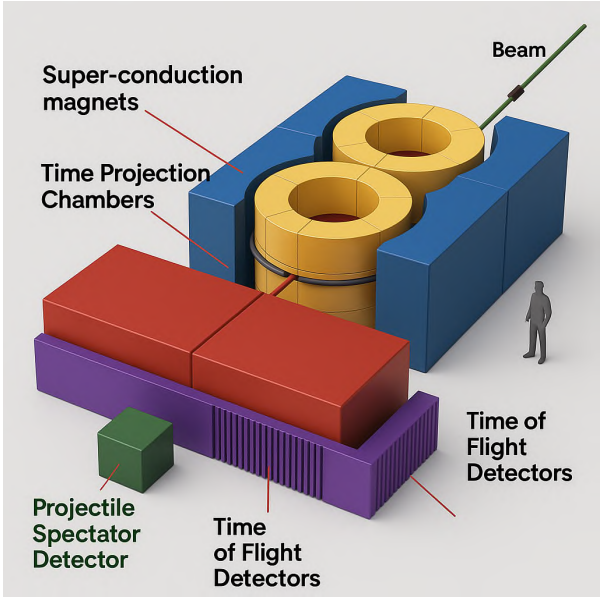

Figure 3.7: A 3D picture of the NA61/SHINE experiment highlighting the detector's position and size.

The NA61/SHINE tracking system comprises four large-volume TPCs, which detect charged par-

ticles by measuring their three-dimensional position and energy deposition within the detector's active volume. A 3D model of the NA61/SHINE setup pointing to the TPCs can be seen in Fig. 3.7.

The Vertex TPCs (VTPC-1 and VTPC-2) (colored in yellow in Fig. 3.7) are positioned between the coils of two large superconducting dipole magnets (blue), VERTEX-1 and VERTEX-2. The magnetic fields in these magnets are oriented anti-parallel to the y-axis (pointing downward), providing a bending power of up to 9 Tm. This provokes positively charged particles to curve towards the positive direction and negatively charged particles towards the negative direction. The precise measurement of particle deflection in these magnetic fields allows for determining the particle's momentum and charge sign. The magnetic field strength is adjusted for each beam momentum to optimize the acceptance in the collision center-of-mass frame.

Downstream of the magnets, there are two additional large-volume TPCs, MTPC-L and MTPC-R (red), that are symmetrically placed around the beamline. These TPCs help improve energy loss measurements and track charged particles that move toward the Time-of-Flight (ToF) detectors (purple).

The TPCs are the primary tracking devices in NA61/SHINE, and provide key data for the reconstruction of charged particle trajectories. Their precise spatial and momentum resolution makes them fundamental to studying the dynamics and products of nuclear collisions.

Projectile Spectator Detector

In heavy ion collisions, the centrality of the collision is a key measurement (see Appendix B). To determine how central a collision was, fixed-target experiments use forward calorimeters, where *forward* refers to the region along the beam axis, typically in the direction that the incoming particle was traveling. These detectors enable event centrality estimation by detecting non-interacting spectators, and they also provide crucial information about the longitudinal energy flow, which is essential for understanding the geometry and dynamics of collisions. This information helps to separate the signal from the background in high-energy physics experiments.

In brief, a forward calorimeter typically consists of an absorber material that forces incoming hadrons to interact and produce a hadronic shower, and active detector layers that detect the secondary particles produced in the shower. As hadrons interact and lose energy in the absorber, the energy is sampled by the active layers, allowing the detector to estimate the total energy of the original hadron.

The Projectile Spectator Detector (PSD) is a zero-degree hadron calorimeter of NA61/SHINE that measures with high precision the energy of projectile spectators in nucleus-nucleus collisions. The energy deposit measured by the PSD is used in offline analyses to determine collision centrality.

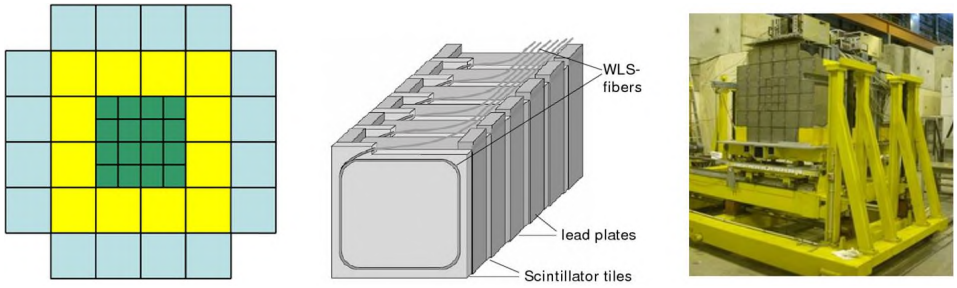

Figure 3.8: Schematic of PSD detector

A detector schematic is shown in the left-most panel of Fig. 3.8. The PSD consists of 44 modules of different sizes: 16 smaller modules (10×10 cm^2) are located at the center, and 28 larger modules (20×20 cm^2) are located in the outer part.

The PSD measures the energy of projectile spectators, enabling centrality of collisions in NA61/SHINE, to help classify how head-on or peripheral an event is. Its measurements provide a critical reference for interpreting fluctuation and correlation data in heavy-ion physics.

Two missing detectors, illustrated in Fig. 3.3, will not be detailed in this section: the Time of Flight detector (ToF) and the Vertex Detector (VD), both of which were used during this data campaign; however, during this analysis, both were excluded, see ref. [69] for details.

Trigger system

The trigger system in high-energy physics experiments, including the NA61/SHINE, plays a key role in event selection, significantly reducing data throughput and experiment complexity. The NA61/SHINE trigger system uses analog signals from beam detectors (excluding BPDs), generating trigger decisions through coincidences of these signals. Signals with delays of up to 300 ns relative to the S1 signal can be included in the trigger, enabling online event centrality selection using signals from other detectors.

The system supports up to four independent configurations (T1-T4), combining coincidences and anticoincidences to generate trigger signals. The configurations used during data collection with Xe+La at 150A GeV/c with secondary hadron beams are detailed in Table 3.1. After the triggers are generated, they are processed by a prescaler module, which selects a fraction of triggers for inclusion in the data sample, reducing the overall data volume. Further details can be found in Ref. [70].

The NA61/SHINE experiment offers a uniquely versatile platform for studying the phase diagram of strongly interacting matter. The goals of the strong interactions program are supported by a

Table 3.1: Trigger definitions used during the Xe+La data-taking campaign.

Trigger	Definition	Description
T1	$S1 \cdot S2 \cdot \overline{\text{V1}}$	identified beam
T2	$S1 \cdot S2 \cdot \overline{\text{S3}} \cdot \overline{\text{V1}} \cdot PSD$	identified interaction
T3	varied (See Ref. [69])	unidentified beam
T4	$S1 \cdot S2 \cdot \overline{\text{S3}} \cdot \overline{\text{V1}}$	unidentified interaction

flexible and well-equipped facility that includes a wide range of detectors and beamline components tailored to different collision systems and energies. Together, the design and capabilities of NA61/SHINE position it as a vital tool in advancing our understanding of strong interaction physics. In the last section, we turn to the final step of NA61/SHINE before the analysis, the processing and reconstruction of the data.

3.3 Data processing and Monte Carlo simulations

In high-energy physics experiments, there is a crucial step between the raw detector output and a meaningful scientific analysis: data processing. Without proper execution, any attempt at physics analysis would be biased, unstructured, or even misleading. In this section, the steps for NA61/SHINE data processing will be discussed.

Reconstruction

Data collected is stored as **events**; each corresponds to a single recorded trigger and contains digitized signals from all detector components. These data, often referred to as raw data, undergo a reconstruction process to convert raw measurements into particle trajectories and related quantities. An example of a reconstructed Xe+La collision is shown in Fig. 3.9.

The event reconstruction procedure, starting from the raw data, consists of several sequential steps:

- **BPD:** An algorithm extracts the positions of beam particles recorded by the three BPDs. Three measured points are fitted with a straight line, providing the trajectory of the beam particle.
- **TPC:**

  - *Cluster Finding:* This reconstruction algorithm searches for signals in TPC pads and time slices. Grouped signals are labeled as clusters. If two distinct maxima are detected within a connected charge region, the algorithm splits them into separate clusters. Then, the position of each cluster is calculated using the center of gravity method, using measured charges as weights.
  - *Local Tracking:* local tracks in each chamber are constructed of clusters for each TPC, always considering the cluster's proximity and the geometrical topology of tracks in MTPCs and curved tracks in VTPCs due to the magnetic field.
  - *Global Tracking:* Local track fragments from different TPCs are merged into global tracks. The track momentum is determined from the curvature of the track in the known magnetic field.

- **Vertices:**

  - *Primary vertex fitting:* The beam particle trajectory measured by the BPDs is extrapolated to the target plane, providing x and y coordinates of the interaction vertex in the NA61/SHINE coordinate system (see Appendix A). All global tracks are extrapolated to the approximate target z plane ($z = -580$ cm), and then, a global track fit is used to find the z coordinate of the interaction vertex. The vertex fitting algorithm returns a result flag indicating the quality of the fit.

- **PSD:** The final step consists of using the tracks recorded by the PSD readout electronics and translating them into energy deposits in sections of modules, single modules, and the whole calorimeter. The new result is that each event contains information on the beam particle trajectory, trigger configuration, energy deposit in the PSD, and a list of tracks. Each track possesses momentum, charge sign, mean energy loss, and the number of measured clusters.

Monte-Carlo simulations

Monte Carlo (MC) simulations are integral to the NA61/SHINE analysis, usually helping to correct for various effects related to detector efficiency, geometric acceptance, and the performance of reconstruction algorithms; however, they are also used for comparison with current theoretical physics models.

A dedicated MC generator simulates particle production in an actual physical interaction. The EPOS 1.99 model was chosen due to its strong agreement with experimental results and continuous support from its developers.

The interaction of generated particles with the detector material is simulated using the GEometry ANd Tracking (GEANT) 3.21 framework. Additionally, a specialized detector response simulation

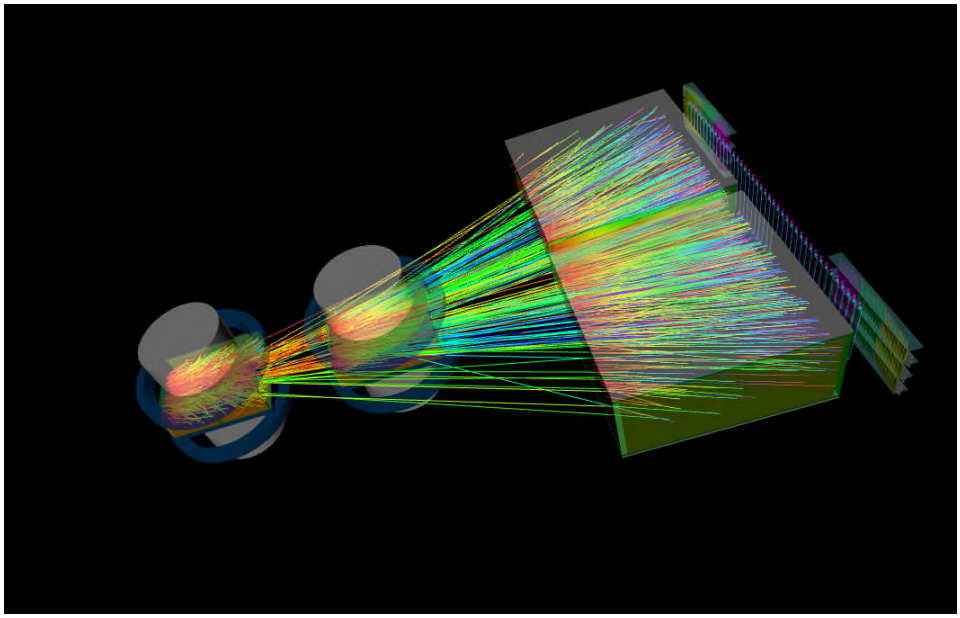

Figure 3.9: Xe+La collision at 150A GeV/c in NA61/SHINE.

is integrated into the NA61/SHINE software of the GEANT framework. The simulation output is stored in a format identical to the data recorded by the detector. It is subsequently processed using the same reconstruction algorithms as those applied to experimental data. In a more simulation output consists of two components:

- Generated Events (EPOS 1.99): These are pure simulated events originating from EPOS . They include information on the momenta, species, trajectories, and origins (whether from primary interaction, decay, or secondary interaction) of the produced particles.
- Reconstructed Events (EPOS + detector effects): These events are processed through the detector response simulation based on the GEANT package and then reconstructed using the same algorithm as the experimental data. The MCrec sample includes most of the information in the reconstructed experimental data.

The two outcomes – MC-generated and MC reconstructed – are used for comparison with the analyzed data as well as determination of systematic uncertainties. In subsequent chapters, a detailed discussion of the use of Monte Carlo analyses in Xe+La simulations will be presented.

Throughout this chapter, it was discussed that the success of the strong interactions program of NA61/SHINE relies on the integration of its high-quality detector components, raw data collection, and its transitions to reconstructed data. The raw data recorded from the collisions in the detector serve as a foundation for all subsequent analyses, capturing the fundamental

signatures of the physical processes being studied. However, it is during the reconstruction process that these signals are transformed into meaningful observables, such as particle trajectories and identities, which enables a detailed exploration of the key phenomena aimed to study in the strong interactions program, including the QCD phase diagram and the search for the critical point. Together, these elements form the pillars of the NA61/SHINE experimental approach, ensuring that the physics goals are pursued with accuracy.

CHAPTER 4

ANALYSIS METHODOLOGY

With the research questions defined, previous studies on SFMs explained, and instrumentation detailed, the next step is to turn to the core of this dissertation: the methodology. This chapter explains the design and reasoning behind the analytical framework employed with a qualitative focus, as well as the application in the current analysis.

To study the fluctuations and correlations previously discussed within the framework of intermittency analysis, the proper variables must be selected. The sensitivity of SFMs (as discussed in Chapter 2) is the primary purpose of this dissertation. We selected the two-dimensional transverse momentum space as a domain where a selection of negatively charged hadrons is made for the calculation of SFMs of rank $r = 2, 3, 4$. Starting from the definition of SFMs for the mentioned 2D phase-space:

$$F_r(M) = \frac{\left\langle \frac{1}{M^2} \sum_{i=1}^{M^2} n_i \ldots (n_i - r + 1) \right\rangle}{\left\langle \frac{1}{M^2} \sum_{i=1}^{M^2} n_i \right\rangle^r}, \tag{4.1}$$

where, $F_r(M)$ referes to the 2D transverse-momentum space that is divided into $M \times M$ equal-size cells and n_i is the number of particles in the i-th cell. For a fixed value of M, the numerator and the denominator are averaged over cells and then over events.

Following the discussion in Chapters 1 and 2, this dissertation covers the NA61/SHINE approach. The next sections will target discussions around the mitigation of background effects, uncertain-

ties, the contribution of two-particle correlations due to detector effects and physics, and model comparison:

- p_T binning or mixed event method (see also Sec. 2.10),
- cumulative p_T binning,
- independent sub-sample of events for each data point,
- analytical calculation of statistical uncertainties,
- momentum-based Two-Track Distance (mTTD),
- systematic uncertainties.

4.1 SFMs dependence on single particle distribution

Various effects and correlations can easily affect the predicted intermittency signal of the critical point. The first type is due to SFMs' sensitivity to the shape of the single-particle momentum distribution; this dependence biases the possible signals of critical fluctuations. Secondly, spurious correlations are due to detector effects, while others are due to physical correlations.

4.1.1 Equivalent expressions and uncertainties

The standard expressions for the SFMs or order $r = 2,3,4$, Eq. 4.1, can be reduced to a more brief expression:

$$F_r(M) = \frac{\left\langle \frac{1}{M^2}\sum_{i=1}^{M^2} n_i ...(n_i - r + 1) \right\rangle}{\left\langle \frac{1}{M^2}\sum_{i=1}^{M^2} n_i \right\rangle^r} = \frac{\frac{1}{M^2}\left\langle \sum_{i=1}^{M^2} n_i ...(n_i - r + 1) \right\rangle}{\frac{1}{M^{2r}}\left\langle \sum_{i=1}^{M^2} n_i \right\rangle^r},$$

but in the denominator, the expression: $\sum_{i=1}^{M^2} n_i$, is nothing more than the event multiplicity N, therefore:

$$= \frac{\frac{1}{M^2}\left\langle \sum_{i=1}^{M^2} n_i...(n_i - r + 1) \right\rangle}{\frac{1}{M^{2r}}\langle N \rangle^r}$$
$$= \frac{(M^2)^{r-1}}{\langle N \rangle^r}\left\langle \sum_{i=1}^{M^2} n_i...(n_i - r + 1) \right\rangle,$$

and knowing that $n_i(n_i-1)...(n_1-r+1) = r!\sum_{i=1}^{M^2}\binom{n_i}{r}$, the summation from the numerator is reduced

$$\sum_{i=1}^{M^2} n_i(n_i-1)...(n_i-r+1) = r!\sum_{i=1}^{M^2}\binom{n_i}{r},$$

giving as a result the form

$$F_r(M) = \frac{r!(M^2)^{r-1}}{\langle N \rangle^r}\left\langle \sum_{m=1}^{M}\binom{n_m}{r}\right\rangle. \tag{4.2}$$

This equation can be further simplified for more straightforward calculations during analysis if we fix $r = 2,3,4$ separately.

For $r = 2$

$$F_2(M) = \frac{2!(M^2)^{2-1}}{\langle N \rangle^2}\left\langle \sum_{i=1}^{M^2}\binom{n_m}{2}\right\rangle = \frac{2M^2}{\langle N \rangle^2}\left\langle \sum_{i=1}^{M^2}\binom{n_m}{2}\right\rangle = \frac{2M^2}{\langle N \rangle^2}\left\langle \sum_{i=1}^{M^2}\frac{n!}{(n-2)!2!}\right\rangle$$
$$= \frac{2M^2}{\langle N \rangle^2}\left\langle \sum_{i=1}^{M^2}\frac{n_i(n_i-1)\cancel{(n_1-2)!}}{\cancel{(n_i-2)!}2!}\right\rangle = \frac{2M^2}{\langle N \rangle^2}\left\langle \sum_{i=1}^{M^2}\frac{n_i(n_i-1)}{2}\right\rangle,$$

but the term in brackets is the average of the total number of pairs in M^2 cells in one event $\langle N_2(M)\rangle$,

$$\boxed{F_2(M^2) = \frac{2M^2}{\langle N \rangle^2}\langle N_2(M)\rangle}. \tag{4.3}$$

A similar process is followed when fixing $r = 3$, and $r = 4$,

$$\boxed{F_3(M) = \frac{6M^4}{\langle N \rangle^3} \langle N_3(M) \rangle}. \tag{4.4}$$

$$\boxed{F_4(M) = \frac{24M^6}{\langle N \rangle^4} \langle N_4(M) \rangle}. \tag{4.5}$$

where the terms in brackets are the average number of triplets for $r = 3$ and quadruplets for $r = 4$ in M cells in one event.

With the help of the modified SFMs' expression, the statistical uncertainties can be calculated using error propagation for Eq. 4.3 $F_2(M)$ notice that M^2 is a fixed parameter without uncertainty, $\langle N \rangle$ is the average multiplicity with variance $Var(N)$) and also $\langle N_2(M) \rangle$ es is the average of pairs with variance $Var(N_2(M))$.

By taking $g := \langle N_2(M) \rangle$, $\quad h := \langle N \rangle$ it is posible to rewrite F_2 like:

$$F_2(g,h) = \frac{2M^2}{h^2} g.$$

By applying error propagation formula, the derivatives of $F_2(g,h)$ respect to g and h are:

$$\frac{\partial F_2}{\partial g} = \frac{\partial}{\partial g}\left(\tfrac{2M^2}{h^2} g\right) = \frac{2M^2}{h^2}, \tag{4.6}$$

$$\frac{\partial F_2}{\partial h} = \frac{\partial}{\partial h}\left(2M^2 g h^{-2}\right) = 2M^2 g \frac{\partial}{\partial h}(h^{-2}) = 2M^2 g(-2)h^{-3} = -\frac{4M^2 g}{h^3}. \tag{4.7}$$

Substitution of the derivatives

$$\sigma^2_{F_2} = \underbrace{\left(\frac{2M^2}{h^2}\right)^2}_{(\partial F_2/\partial g)^2} Var(g) + \underbrace{\left(-\frac{4M^2 g}{h^3}\right)^2}_{(\partial F_2/\partial h)^2} Var(h) + 2\left(\frac{2M^2}{h^2}\right)\left(-\frac{4M^2 g}{h^3}\right) Cov(g,h)$$

$$= \frac{4M^4}{h^4} Var(g) + \frac{16M^4 g^2}{h^6} Var(h) - \frac{16M^4 g}{h^5} Cov(g,h).$$

Also, it would be very useful to normalize for F_2 by

$$F_2 = \frac{2M^2}{h^2} g \implies F_2^2 = \left(\tfrac{2M^2}{h^2} g\right)^2 = \frac{4M^4 g^2}{h^4}.$$

And finally,

$$\frac{\sigma^2_{F_2}}{F_2^2} = \frac{\frac{4M^4}{h^4}Var(g) + \frac{16M^4g^2}{h^6}Var(h) - \frac{16M^4g}{h^5}Cov(g,h)}{\frac{4M^4g^2}{h^4}}.$$

Simplifying each term,

1. $$\frac{\frac{4M^4}{h^4}Var(g)}{\frac{4M^4g^2}{h^4}} = \frac{Var(g)}{g^2} = \frac{Var\big(\langle N_2(M)\rangle\big)}{\langle N_2(M)\rangle^2},$$

2. $$\frac{\frac{16M^4g^2}{h^6}Var(h)}{\frac{4M^4g^2}{h^4}} = \frac{16}{4}\frac{h^{-6}}{h^{-4}}Var(h) = 4\frac{Var(h)}{h^2} = 4\frac{Var\big(\langle N\rangle\big)}{\langle N\rangle^2},$$

3. $$\frac{\big(-\frac{16M^4g}{h^5}\big)Cov(g,h)}{\frac{4M^4g^2}{h^4}} = -\frac{16}{4}\frac{gh^{-5}}{g^2h^{-4}}Cov(g,h) = -4\frac{Cov(g,h)}{gh} = -4\frac{Cov\big(\langle N_{pp}\rangle,\langle N\rangle\big)}{\langle N_{pp}\rangle\langle N\rangle},$$

one obtains

$$\frac{\sigma^2_{F_2}}{F_2^2} = \frac{Var\big(\langle N_2(M)\rangle\big)}{\langle N_2(M)\rangle^2} + 4\frac{Var\big(\langle N\rangle\big)}{\langle N\rangle^2} - 4\frac{Cov\big(\langle N_2(M)\rangle,\langle N\rangle\big)}{\langle N_2(M)\rangle\langle N\rangle}.$$

Finally,

$$\boxed{\frac{\sigma_{F_2}}{|F_2|} = \sqrt{\frac{Var\big(\langle N_2(M)\rangle\big)}{\langle N_2(M)\rangle^2} + 4\frac{Var\big(\langle N\rangle\big)}{\langle N\rangle^2} - 4\frac{Cov\big(\langle N_2(M)\rangle,\langle N\rangle\big)}{\langle N_2(M)\rangle\langle N\rangle}}}.$$

Procceding similarly for the 3rd, and 4th SFM, we obtain:

$$\boxed{\frac{\sigma_{F_3}}{|F_3|} = \sqrt{\frac{Var\big(\langle N_3(M)\rangle\big)}{\langle N_3(M)\rangle^2} + 9\frac{Var\big(\langle N\rangle\big)}{\langle N\rangle^2} - 6\frac{Cov\big(\langle N_3(M)\rangle,\langle N\rangle\big)}{\langle N_3(M)\rangle\langle N\rangle}}},$$

$$\boxed{\frac{\sigma_{F_4}}{|F_4|} = \sqrt{\frac{Var\big(\langle N_4(M)\rangle\big)}{\langle N_4(M)\rangle^2} + 16\frac{Var\big(\langle N\rangle\big)}{\langle N\rangle^2} - 8\frac{Cov\big(\langle N_4(M)\rangle,\langle N\rangle\big)}{\langle N_4(M)\rangle\langle N\rangle}}}.$$

The results obtained in this section are necessary for the following steps. The display of results splits at this point, where two methodologies were analyzed.

4.1.2 Transverse momentum binning

To address the dependence of the SFMs on the shape of single-particle distribution, NA49 proposed to study ΔF_2 (see Sec. 2.8), and is referenced in some NA61/SHINE conferences and papers as *mixed event method*. In this text, from now on this term will be referred to as p_T *binning*, where instead of studying $F_2(M)$ we study $\Delta F_2(M)$, defined as follows:

$$\Delta F_r(M) \approx F_r^{\text{data}}(M) - F_r^{\text{mixed}}(M), \tag{4.8}$$

In the case of this method, particles from different data events are used to generate a mixed event set. To create a mixed event, we select particles from other events in the original dataset while preserving the original dataset's multiplicity distribution. This removes all correlations between particles in the events, but the multiplicity distribution of data and mixed events remains identical.

It was shown in [40] that this procedure approximately removes the dependence of $\Delta F_2(M)$ on the shape of a single-particle transverse momentum distribution [38], [40].

4.1.3 Cumulative transverse momentum binning

Since the experimental results on $F_r(M)$ depend on the shape of the single-particle distribution and the selection of variables used for analysis, as said in Sec. 2.3.2.1, Białas and Gaździcki [42] proposed to study intermittency in terms of variables for which the single-particle density is constant. It was also shown in the same paper that this method reduces the bias caused by a non-uniform single-particle distribution, leaving the critical point signal approximately unchanged [43]. The premise and results of this thesis are derived from a comparison of the two methodologies.

How does the cumulative transformation work?

Assume that the single particle distribution in a variable x is measured and given by a (non-negative) function $f(x)$. For a one-dimensional distribution $f(x)$, the cumulative variable, Q_x, is defined as:

$$Q_x = \int_{x_{\min}}^{x} f(x')dx' \Big/ \int_{x_{\min}}^{x_{\max}} f(x')dx' \,, \tag{4.9}$$

where $x_{\min}$ and $x_{\max}$ are lower and upper limits of the variable x. For a two-dimensional distribution $f(x,y)$ and a given x the second variable, $Q_y(x)$, is defined as:

$$Q_y(x) = \int_{y_{\min}}^{y} f(x,y')dy' \Big/ \int_{y_{\min}}^{y_{\max}} f(x,y')dy' , \tag{4.10}$$

with $y_{\min}$ and $y_{\max}$ denoting lower and upper limits of the variable y.

Figure 4.1 shows example distributions to illustrate what the cumulative transformation looks like once it is applied to the transverse-momentum components p_x and p_y, The distributions are shown *before* (top) applying the transformation and *after* (bottom) using the transformation. Examples are from the analyzed data set Xe+La at 150A GeV/c. In Fig. 4.2, a visualization of the change of variables with the cumulative transformation, as defined in Eq. 4.1.3.

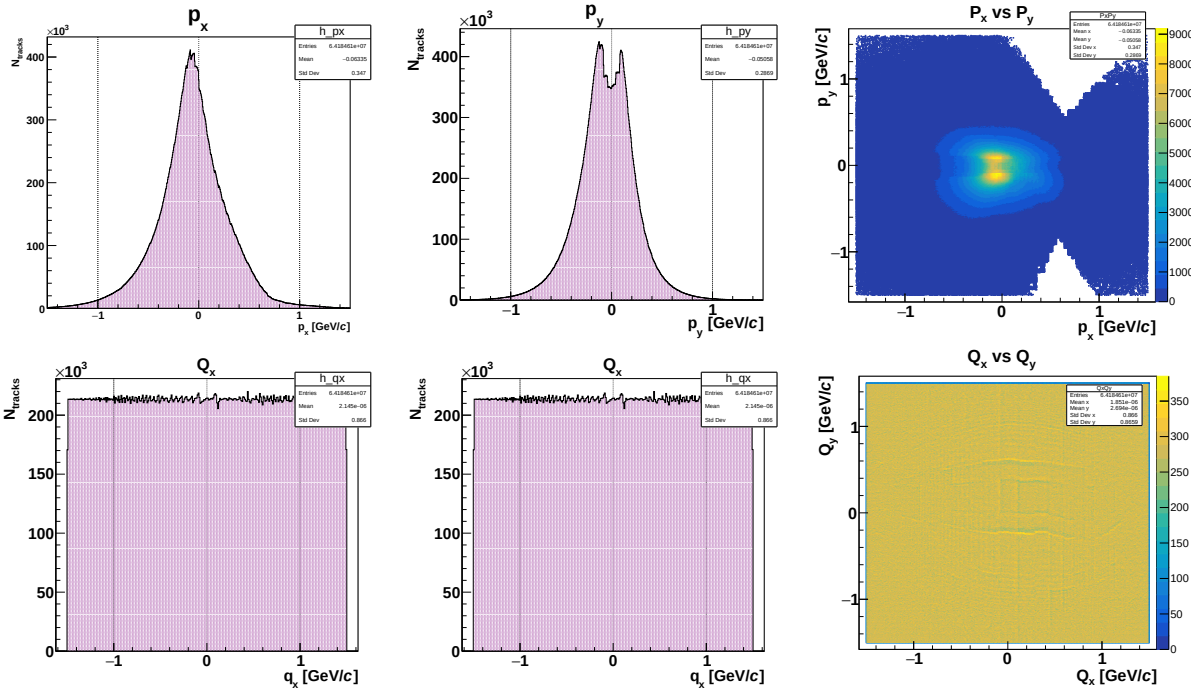

Figure 4.1: Example distributions of the p_x and p_y distributions before and after cumulative transformation [42]. Figures shown on the top panel are the distributions before, and those in the bottom panel are the distributions after applying the cumulative transformation. (*top*) Distributions from left to right of 1D p_x, p_y and 2D p_x vs p_y. (*bottom*) Cumulative distributions from left ot right Q_x, Q_y and 2D Q_x vs Q_y. Distributions correspond to the data set analyzed in this thesis ^{129}Xe+^{139}La 150A GeV/c.

4.2 Statistically independent data points

A significant difference between previous studies in SFMs (See Sec. 2.3.1) and those presented in this thesis consists of the following: previous results for each subdivision number M were derived

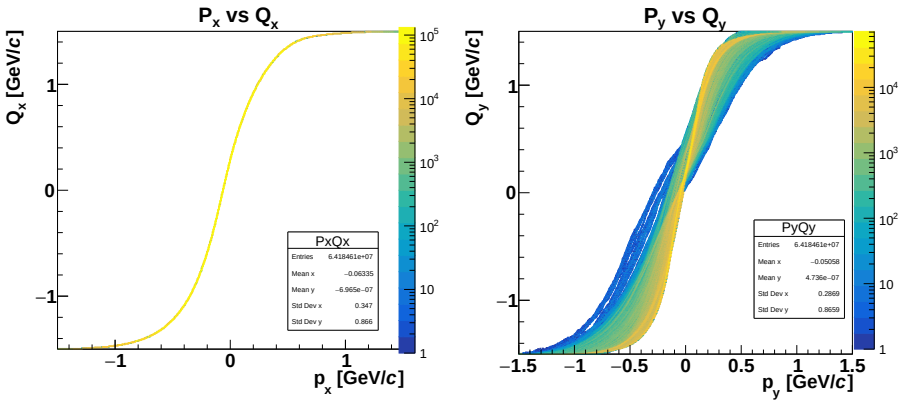

Figure 4.2: Visualization of how variables change before and after applying the cumulative transformation in the form of a 2D histogram following Eq. 4.1.3. *Left* p_x to Q_x, is transformed unambiguously (by definition). *Right* p_y to Q_y is transformed slightly smeared (by definition).

from the same data set. As a result, the measurements for different M values are statistically correlated, requiring the full covariance matrix for a rigorous statistical interpretation. This process is numerically demanding [25].

In contrast, the present and latest NA61/SHINE intermittency analysis [23], [41] use statistically independent subsets of events for each data point for M^2. This approach ensures that results for different M values are *uncorrelated*, with only the diagonal elements of the covariance matrix being non-zero.

4.3 Momentum-based Two-Track Distance cut

The TPCs of the NA61/SHINE (as seen in Sec. 3.2.2) are the primary tracking devices; unfortunately, however, they are not perfect, and the main limitation of particle fluctuation analysis is that the clusters tend to overlap when two particles are too close in space. Therefore, the TPCs cannot differentiate them. As a consequence, the TPC cluster finder typically rejects overlapping clusters, causing those tracks to be lost. Furthermore, the TPC track reconstruction can fail, merging two track fragments. This issue can generate two tracks from a single track, producing a false intermittency signal due to the sensitivity of the analysis.

The solution to this problem is a tool that eliminates all kinds of spurious correlations resulting from detector effects. The Momentum-based Two Track distance cut (mTTD from now on) is introduced to the intermittency analysis by NA61/SHINE as a two-particle acceptance map in momentum space.

The problem is illustrated in Fig. 4.3. In this illustration, a split track is presented. Although a *standard selection* of tracks enables reducing this problem (see Sec. 5.1.2), the problem is not

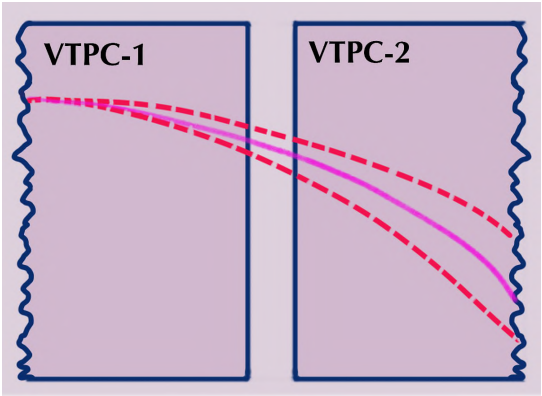

Figure 4.3: Illustration of the problem with tracking on NA61/SHINE TPCs. On the left column is a representation of split tracks.

entirely solved; therefore, the momentum-based Two-Track distance cut (mTTD) can effectively eliminate split tracks. A previous version of this cut, the geometric Two-Track Distance (gTTD) cut, was utilized to eliminate a set of tracks positioned too close to be reconstructed using geometrical two-track distance calculations. However, this process was inaccurate.

The gTTD is still used to determine the proper mTTD cut for the analysis. An example comparing the Two-Track Distance distribution without any cut, with gTTD cut, and mTTD cut can be seen in Fig. 4.4 for the ^{129}Xe+^{139}La data set at 13 A GeV/c. Notice in the left-most column the number of pairs that are too close in space to each other. In the right column, mTTD was determined and applied. Top distributions display the number of pairs of data and mixed sets. At the same time, the bottom shows the ratio of data to mixed sets, enabling a better understanding of the problematic particle pairs.

To apply the mTTD cut, one must first determine the gTTD cut. In this thesis, the NA61/SHINE detector geometry and magnetic field information are required, but access to this information is limited to those members of the NA61/SHINE Collaboration. Still, for other readers, the process will also be explained; we need to locate a set of points for each track along the experiment. This is why we need the magnetic field information and the detector geometry; the points for each track can be obtained using both.

The magnetic field bends the trajectory of charged particles in the $x-z$ planes. Once the location points have been obtained, it is reasonable at this point to express the momentum of each particle in the following momentum coordinates, which do not depend on the detector coordinates (see Fig. 4.5):

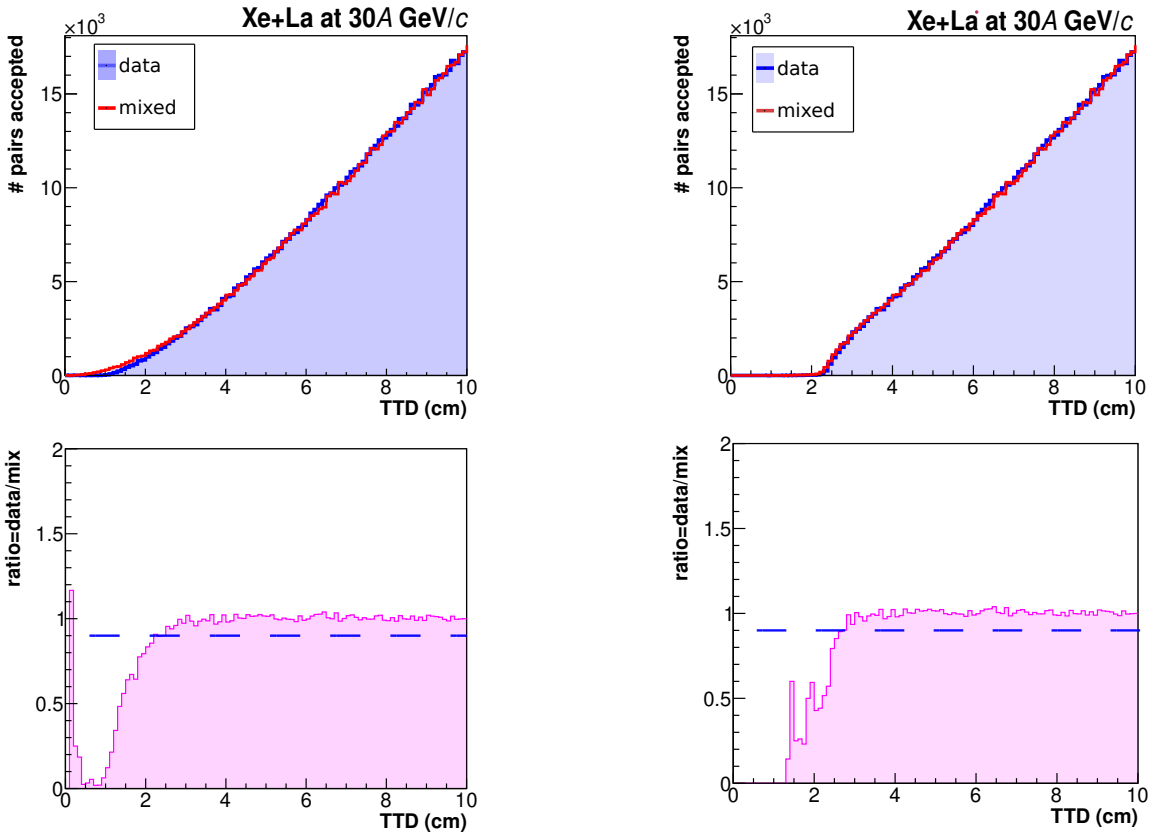

Figure 4.4: Comparison of pair distributions before and after applying the two-track distance cut. The top columns show the number of pairs for both data and mixed events, while the bottom columns display the data-to-mixed ratio, providing a clearer view of problematic split tracks. In the left column, a large number of pairs are found to be too close in space. In contrast, the right-most column shows the result of applying the mTTD cut, which more efficiently suppresses close pairs while preserving a larger number of valid pairs.

$$
\begin{aligned}
s_x &= p_x/p_{xz} = \cos(\Psi) \,, \\
s_y &= p_y/p_{xz} = \sin(\lambda) \,, \\
\rho &= 1/p_{xz} \,,
\end{aligned}
\tag{4.11}
$$

where $p_{xz} = \sqrt{p_x^2 + p_z^2}$.

Now, to determine the selection itself for each pair of particles, the difference in the new coordinates is calculated as follows:

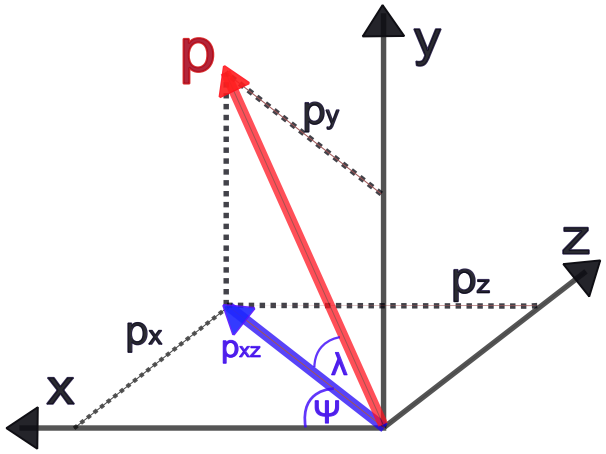

Figure 4.5: New momentum coordinate system to calculate mTTD cut.

$$\begin{aligned} \Delta s_x &= s_{x,2} - s_{x,1} \,, \\ \Delta s_y &= s_{y,2} - s_{y,1} \,, \\ \Delta \rho &= \rho_2 - \rho_1 \,. \end{aligned} \tag{4.12}$$

The distributions of particle pairs' momentum difference for pairs with gTTD less than x cm are parameterized with ellipses in the new momentum coordinates. Such parameterized elliptical cuts are defined as:

$$\begin{aligned} \left(\frac{\Delta\rho}{r_\rho}\right)^2 + \left(\frac{\Delta s_y}{r_{s_y}}\right)^2 &\leq 1 \,, \\ \left(\frac{\Delta s_x}{r_{s_x}}\right)^2 + \left(\frac{\Delta s_y}{r_{s_y}}\right)^2 &\leq 1 \,, \\ \left(\frac{\Delta\rho\cos\theta - \Delta s_x \sin\theta}{r_{\rho s_x}}\right)^2 + \left(\frac{\Delta\rho\sin\theta + \Delta s_x\cos\theta}{r_{s_x\rho}}\right)^2 &\leq 1 \,, \end{aligned} \tag{4.13}$$

where $r_{\rho s_x}$ and $r_{s_x\rho}$ represent the semi-major and semi-minor axes of the ellipse defined by $\Delta\rho$ and Δs_x, respectively, while θ denotes the angle between the positive horizontal axis and the ellipse's major axis. The semi-axes of the other ellipses are similarly defined in Eqs. 4.13. An illustration can be seen in Fig. 4.6.

One particle from each pair with a momentum value falling within any of the defined ellipses is rejected randomly. The mTTD cut, based on these momentum correlations, serves as a replacement for the gTTD cut as shown in Fig. 4.6. Due to its momentum-space definition, the mTTD

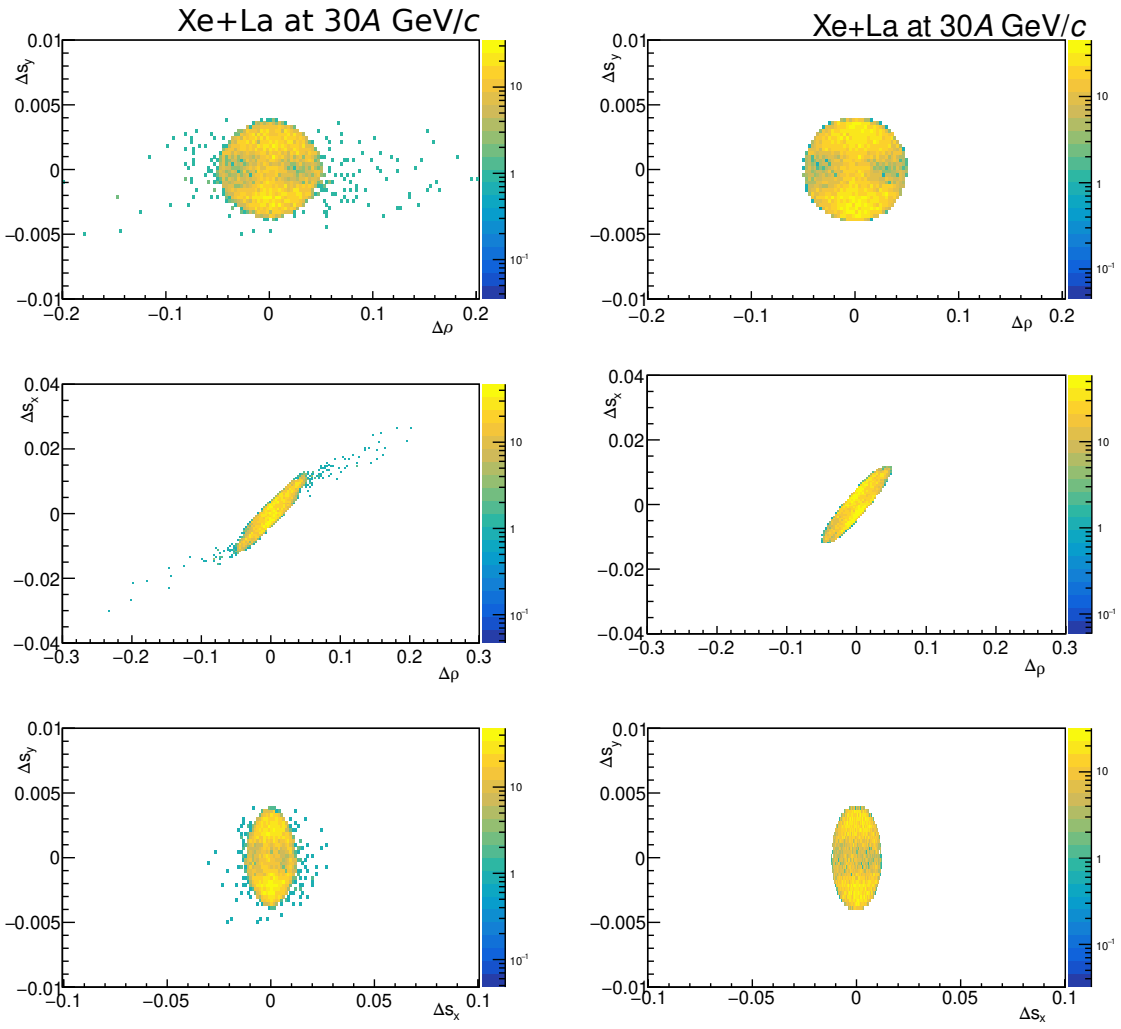

Figure 4.6: Example of the ellipses of rejected particles and in the mTTD coordinate system for the Xe+La 30*A* GeV/*c*. On the left are the ellipses formed by the gTTD cut; on the right are the ellipses after applying the mTTD cut.

cut is well-suited for comparing experimental results with model predictions, too. The specific parameters used for the mTTD cut vary with the collision system size and collision energy, and the values will be summarized in Chapter 5. This cut is applied throughout the data analysis and in the model comparisons.

4.4 Two-particle correlation functions

The two-particle correlation functions, Δp_T and q_{LCMS} of negatively charged particles within the analysis acceptance, were also studied in the frame of this thesis. These two functions can reveal the existence of correlation functions due to physics. The variables are defined as follows:

$$\Delta p_T = \sqrt{(p_{2,x} - p_{1,x})^2 + (p_{y,2} - p_{y,1})^2}, \tag{4.14}$$

$$q_{LCMS} = \sqrt{(p_{1,x} - p_{2,x})^2 + (p_{1,y} - p_{2,y})^2 + q_z^2}. \tag{4.15}$$

The subscript *LCMS* in q_{LCMS} stands for longitudinally co-moving system, and is widely used in the investigation of Bose-Einstein or HBT correlations in Femtoscopy analysis [71], and the variable q_z is defined as:

$$q_z^2 = 4 \cdot \frac{(p_{z,1} \cdot E_2 - p_{z,2} \cdot E_1)^2}{(E_1 + E_2)^2 - (p_{z,1} + p_{z,2})^2}, \tag{4.16}$$

where E_1 and E_2 are the energies of particles 1 and 2, assuming the mass of a pion (for more details see Appendix A).

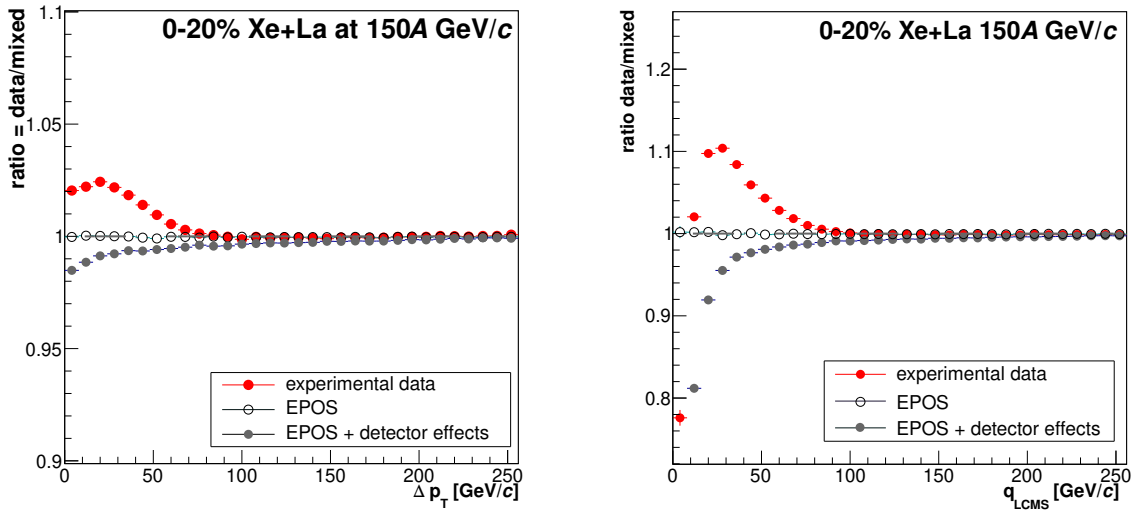

Figure 4.7: The example shown in this plot corresponds to negatively charged hadrons in Xe+La interactions at 150*A* GeV/*c* for real data (orange), EPOS MonteCarlo generator (red), and EPOS generator with NA61/SHINE detector effects (blue). (*left*) Δp_T correlation function; (*right*) q_{LCMS} correlation function.

The correlation function is the ratio of normalized Δp_T or Δq_{LCMS} distributions of data over mixed events. Example distributions for real Xe+La data at 150*A* GeV/*c* and EPOS can be seen in

Fig. 4.7. In both columns, we can see in orange the results that correspond to real data, displaying the expected form in the presence of short-range correlations. EPOS does not have this type of correlation in its model; therefore, the correlation functions do not present the same hill. The entire discussion of the results obtained can be found in the results chapter.

The final consideration regarding these correlations is their correspondence with each other. From the former equations, we understand that the first variable depends only on two dimensions. At the same time, the second is an extended version widely used in other types of studies, like Femtoscopy, which helps quantify other types of short-range correlations more extensively.

4.5 Power-Law Model

One very important question remains: what will intermittency actually look like? Critical point and QGP are not adequately modeled in all actual Monte Carlo tools available worldwide for simulation studies. How can we study the intermittency approach in the case of a power-law?

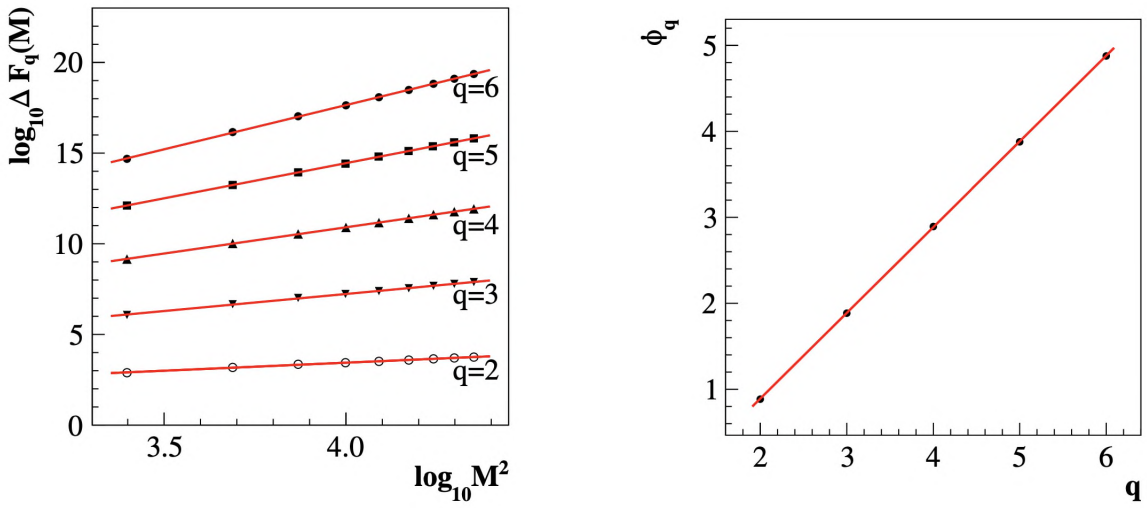

Figure 4.8: SFMs of the orders from $r = 2$ to $r = 6$ (*left*) and power-law exponents $\phi_2, ..., \phi_6$ obtained from their fits (*right*) for 10000 events with six correlated particles each, generated with the Power-law model, image extracted from [28].

A tool used in NA61/SHINE to solve this problem is the Power-law Model developed in [28], as a part of the search for the critical point, studying power-law fluctuations within the framework of intermittency analysis, which is ongoing. It is a simple model that generates power-law multi-particle correlations that can be introduced into datasets to be analyzed and studied. The main features of this model are:

- two controllable parameters: strength of the correlation (power-law exponent) and fraction

of correlated particles,

- configurable number of events,
- configurable multiplicity distribution,
- configurable inclusive transverse momentum distribution.

This means that the Power-law model can be configured to produce correlated pairs of particles, given the parameters obtained. Fig. 4.8 is a plot done with this model that gives back a perfect power-law, as would be expected in intermittency. The advantages provided by this model enable studies of how other variables behave in the presence of a power-law, as well as to quantify the results obtained. Results obtained under the Power-law model will be discussed in the following chapters.

CHAPTER 5

ANALYSIS DETAILS

The objective of this analysis is to investigate signals of intermittency (or the absence thereof) in systems different from those explored in Ref. [23], [41] by NA61/SHINE, and offer insights of power law reported such as the one in [39].

Reproducibility is a cornerstone of scientific research, ensuring that results can be independently verified and validated. For this reason, this chapter is dedicated to outlining the methods and protocols in full detail, allowing for the accurate replication of the experiments by other researchers for the present analysis, i.e., measuring the SFMs of negatively charged hadrons within the analysis acceptance in 0-20% central Xe+La collisions at 13A, 19A, 30A, 40A, 75A and 150A GeV/c beam momentum performed by NA61/SHINE.

5.1 NA61/SHINE data analysis

To ensure the quality of the results in this dissertation, a total of three data sets of the Xe+La energies mentioned were analyzed:

- Experimental **Xe+La** data recorded in the 2017 data campaign,
- Simulated EPOS 1.99 data,
- Simulated data after GEANT 3 and the standard NA61/SHINE reconstruction. From here on, it is referred to as EPOS RECONSTRUCTED .

Table 5.1: Number of events in millions for each beam momentum.

$p_{\mathbf{beam}}$ **[A GeV/**c**]**	$\sqrt{s_{NN}}$ **[GeV]**	**Number of events (in millions)**		
		Exp. data	**EPOS**	**EPOS RECONSTRUCTED**
13	5.12	3.0	20	20
19	6.12	3.8	20	20
30	7.62	4.6	20	20
40	8.76	3.8	20	20
75	11.94	2.1	20	20
150	16.83	4.7	20	20

The selection procedure for events and tracks is described below, with further details provided in each section.

5.1.1 Event selection

There are two distinct sets of criteria for event selection. The first set, *the non-biasing cuts*, does not involve variables whose values are influenced by the interaction. These cuts do not introduce bias into the analysis results; instead, they reduce the number of irrelevant events. They are based on beam position, composition, and time structure. The second set, *the biasing cuts*, may affect the analysis outcomes if not applied carefully. These cuts are primarily used to eliminate background from non-target interactions or to select events based on collision centrality.

A summary of the event selection will be explained and presented in this section, alongside examples of every selection mark. A list that shows how many events are rejected after each selection is applied can be consulted in Table 5.2. The code used can be consulted in Ref. [68].

Simulated data already contains only desired reactions; hence, no specific selection is needed. However, to correct for event losses due to the primary vertex position and the elastically scattered beam cuts, these selection criteria are applied to reconstructed simulated data. These are detailed in the Table 5.2.

Interaction trigger

Not all collisions are relevant for the analysis; for example, background and non-interacting events are excluded from the data set of analyzed events. To remove the events that don't fit this criterion, each event is required to have an interaction with the T2 interaction trigger (see

Table 5.2: Effect of event selection criteria on the Xe+La energy scan data. Shown are the percentages of total events retained after each successive selection stage.

Experimental data set	**Percentage of events retained**					
$\mathbf{p_{beam}}$ **[*A* GeV/*c*]**	**13**	**19**	**30**	**40**	**75**	**150**
Total number of events	100	100	100	100	100	100
Interaction trigger	80.32	81.25	81.24	81.30	83.85	82.81
Beam off-time particles	26.82	31.79	39.21	39.70	39.64	38.64
Beam quality	26.77	31.73	39.10	39.62	39.54	36.54
Beam charge	24.80	29.71	36.03	36.97	37.32	35.32
Beam particles position	24.57	29.37	35.43	36.00	36.68	34.68
Interaction vertex fit quality	24.47	29.25	35.29	35.68	36.51	34.52
PSD status	24.47	29.25	35.29	35.68	35.93	33.91
PSD peripheral energy	24.47	29.24	35.19	35.01	35.71	33.71
Interaction vertex z position	22.30	26.54	32.49	32.91	33.55	32.55
Tracks ratio	22.27	26.48	32.41	32.84	33.46	32.46
Centrality	14.86	12.16	17.24	13.01	33.46	32.12

Sec. 3.2.2). In addition to filtering for genuine interactions, this trigger is also used to isolate the most central collisions, which are of particular interest for the analysis.

Beam off-time particles

Events where an additional beam particle interacts near the trigger particle can distort fluctuation measurements by mimicking collision products or causing a second, indistinguishable interaction. To mitigate this issue, a timing-based selection criterion is applied to identify and remove such events. The primary method uses the time distribution of beam particles relative to the trigger signal, typically implemented through the WaveForm Analyzer (WFA) criteria. For Xe+La event selection, this cut ensures that no off-time beam particle is present within a 25 μs window around the S11 signal of the trigger particle.

Beam quality and charge

The quality of the reconstructed beam can be affected by an undefined trajectory or incorrect charge identification, which can introduce background events and compromise the accuracy of the analysis. To address this, two selection criteria based on the Beam Position Detector 3 (BPD-3) are applied.

The first criterion ensures that only events with well-defined beam signals are accepted. It selects events with a clear signal, identified charge, and accurate x and y position from BPD-3.

The second criterion specifically verifies the charge of beam ions measured by BPD-3. Figure 5.1 shows the distribution of the charge signals on the x and y planes; the accepted charge region is indicated with a red ellipse. The parameters of ellipses used to select valid events in the Xe+La data sets are listed in Table 5.3.

Table 5.3: Parameters of the ellipses (major and minor axis limits and axis ratios) used to define the BPD-3 charge selection for event filtering.

$\mathbf{p_{beam}}$ [A GeV/c]	X_μ	Y_σ	Y_μ	Y_σ
13	4227	336	3898	279
19	4266	291	3973	258
30	4354	343	4047	299
40	4287	334	3961	378
75	4449	320	4419	286
150	4984	323	4628	274

Beam particles positions

Beam particles with badly defined trajectories, like those that bend before reaching the target or bypass the beam detectors, can also interfere with the analysis. To eliminate such cases, a selection criterion is applied that requires a well-defined beam position, as measured by BPD-3. This ensures that the beam has passed through the expected trajectory and was accurately detected. Figure 5.2 shows the beam position distributions from BPDs, illustrating the applied cut for both the lowest and highest energy beams. The parameters of the ellipses used to select events passing this criterion are listed in Table 5.4.

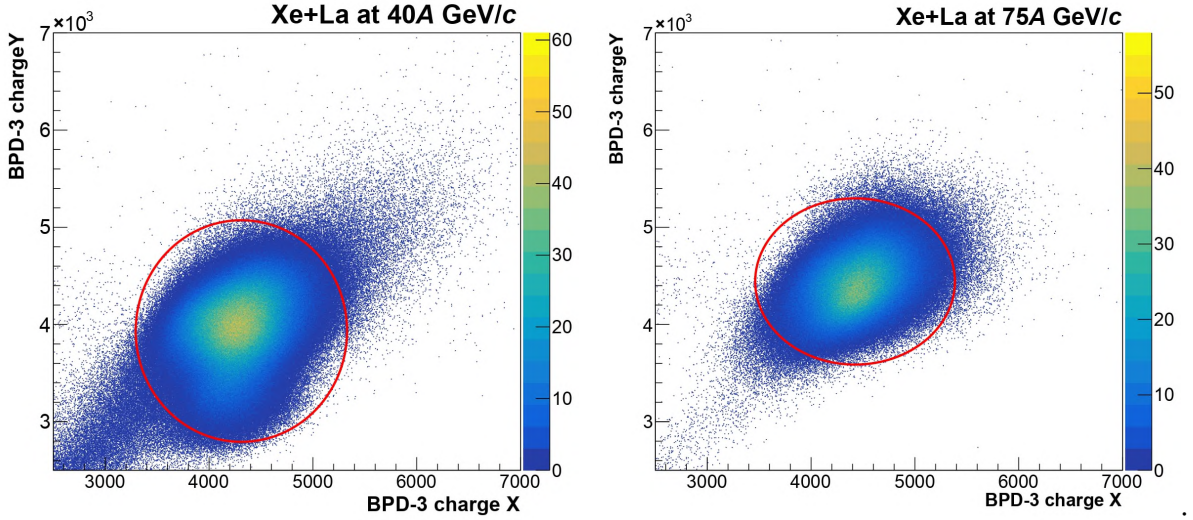

;

Figure 5.1: BPD-3 counter charge distributions for Xe+La at 40*A* GeV/*c* and 75*A* GeV/*c*. In the vertical axis, the charge is detected in the Y plane; in the horizontal axis, the charge is detected in the X plane. Red ellipses point to the right BPD charge signals selected.

Table 5.4: Parameters of the ellipses (major and minor axis limits and axis ratios) used to define the beam particles position selection for event filtering.

$\mathbf{p_{beam}}$ **[*A* GeV/*c*]**	X_μ	Y_σ	Y_μ	Y_σ
13	0.175	0.169	0.089	0.167
19	0.172	0.108	0.200	0.103
30	0.163	0.079	0.107	0.061
40	0.209	0.067	-0.098	0.049
75	0.098	0.029	0.120	0.054
150	0.214	0.076	-0.180	0.093

Interaction vertex fit quality

Poorly reconstructed or missing interaction vertices can lead to significant uncertainties in event characterization. To avoid such issues, a selection criterion is applied to ensure that a well-defined interaction vertex is reconstructed during the event reconstruction process. This selection accepts only events where the vertex fit converges and meets a minimum quality threshold. It guarantees that the event geometry is reliably determined.

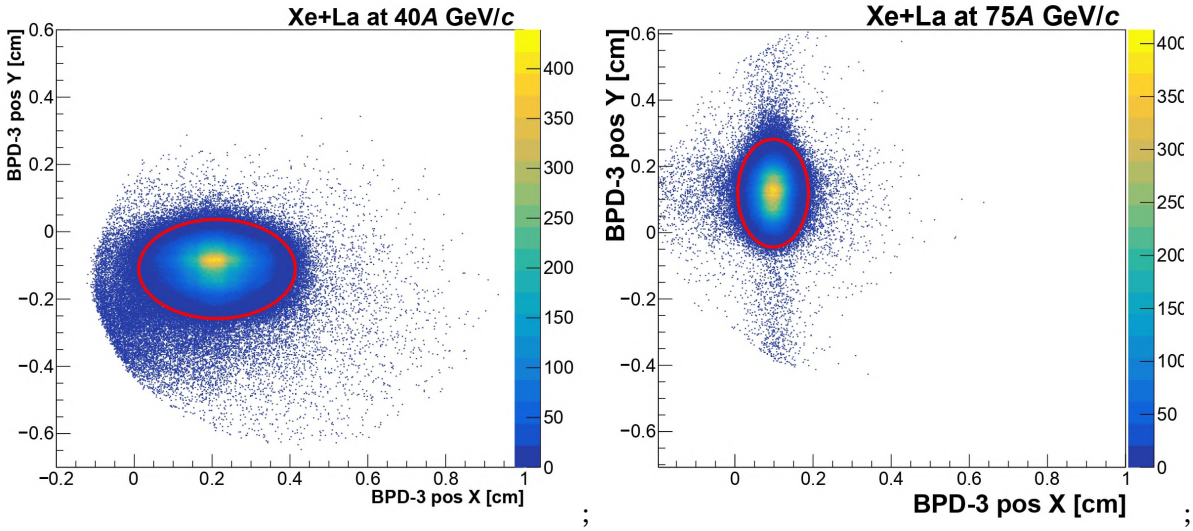

Figure 5.2: BPD-3 counter position distributions for Xe+La collisions at 40*A* and 75*A* GeV/*c*. In the vertical axis, the position detected in the Y plane; in the horizontal axis, the position detected in the X plane. Red ellipses point to the right BPD charge signals selected.

PSD status and PSD energy

While the PSD detector is described in Sec. 3.2.2, several issues that arose during the data-taking period were reported internally in NA61/SHINE. Specifically, some modules were non-functional or produced unreliable signals, which could compromise the accuracy of the recorded data. To mitigate this, only well-performing modules were used in the analysis, with selections made separately for each beam energy. The central modules included for each energy are shown in Fig. 5.3, and the selected peripheral modules are shown in Fig. 5.4.

For the *PSD status* criterion, the status of both selected and peripheral modules is reviewed and accepted if this status is *good*. For the *PSD per energy*, the energy of the peripheral modules is reviewed, and for each Xe+La energy, a limit is established. Limits can be seen in Table 5.5.

Interaction vertex Z position

The reconstructed vertex Z position corresponds to the location along the beamline where the collision occurs, but not all reconstructed vertices originate from the actual target region; some come from background interactions outside the target, detector material interactions, or mis-reconstructed events.

A selection on the vertex Z position is applied by identifying a sharp peak in the vertex distribution that corresponds to the actual target location. By selecting only events with vertex Z positions within a defined window around this peak, the values of which can vary with beam energy,

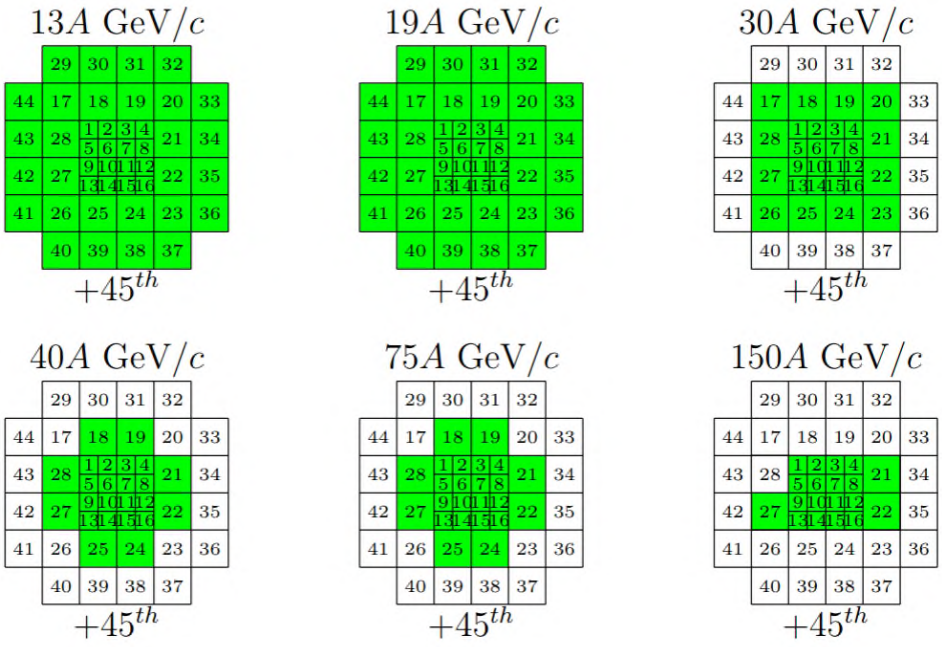

Figure 5.3: PSD modules selected for Xe+La analysis, selected modules are shown in bright green, excluded modules are colorless.

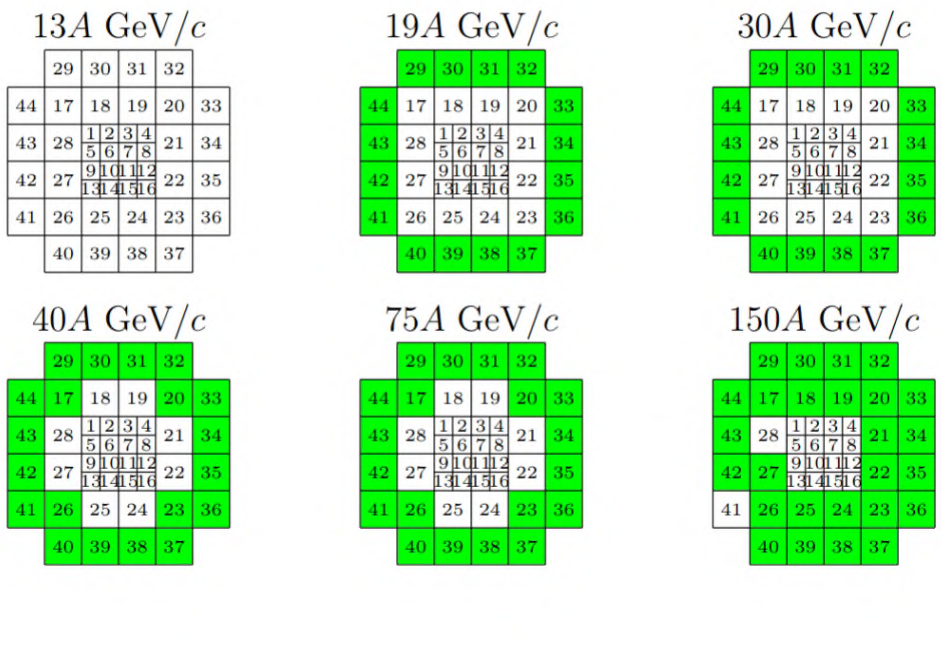

Figure 5.4: PSD peripheral modules selected for Xe+La analysis, selected modules are shown in bright green, excluded modules are colorless.

Table 5.5: List of PSD energy limit values, PSD peripheral limit values for event selection due to reported PSD modules malfunctioning.

$\mathbf{p_{beam}}$ [*A* GeV/*c*]	$\mathbf{PSD_{selected}}$	$\mathbf{PSD_{peripheral}}$
13	787	0
19	1382	50
30	2175	125
40	2875	300
75	5225	500
150	8925	2200

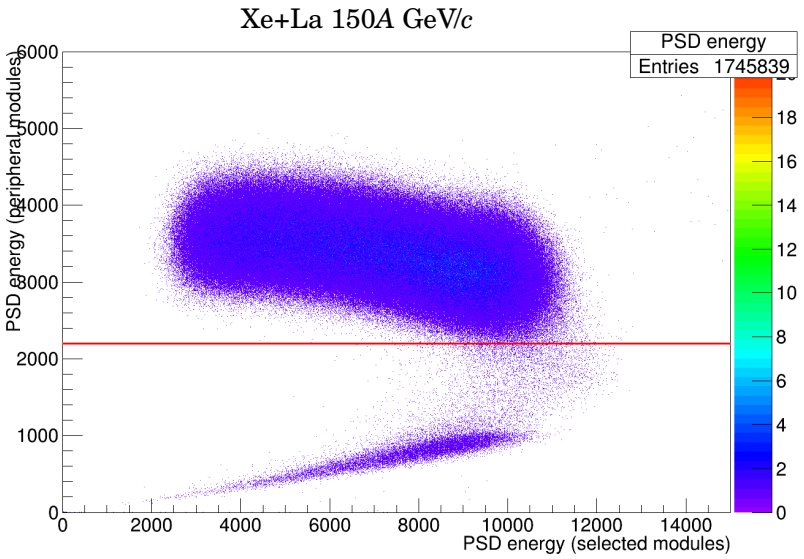

Figure 5.5: PSD energy distributions for Xe+La at 150*A* GeV/*c*. In the vertical axis, PSD energy of peripheral modules, in the horizontal axis, PSD energy of selected modules. The red line indicates the cut value.

background events are suppressed. The values of this Z-peak with the corresponding window selection are listed in Table 5.6.

All tracks vs tracks from the main vertex

During event reconstruction, not all tracks detected in an event necessarily come from the main collision vertex; some may originate from secondary interactions or background sources. To ensure that the reconstructed main vertex represents a genuine collision, a selection is applied

Table 5.6: Vertex z position list for each Xe+La beam momenta

$\mathbf{p_{beam}}$ [*A* GeV/*c*]	$\mathbf{Z_{peak}}$
13	-603.3
19	-602.9
30	-602.9
40	-602.9
75	-602.9
150	-602.7

based on the number of tracks used in the vertex fit compared to the total number of tracks detected in the event. Specifically, if the number of tracks included in the vertex fit is below a certain threshold (values for each energy are listed in Table 5.7), then the ratio of tracks used in the vertex fit to the total number of tracks in the event must exceed a minimum value. In this way, the requirement helps reject poorly reconstructed vertices or background events with many tracks not associated with the primary vertex. Example distributions illustrating this ratio can be found in Fig. 5.6.

Table 5.7: List of criterion value for all tracks vs tracks from main vertex selection

$\mathbf{p_{beam}}$ [*A* GeV/*c*]	**Tracks ratio**
13	0.10
19	0.10
30	0.15
40	0.15
75	0.20
150	0.20

Centrality selection

Experimental data

To determine the centrality of each collision event, the energy deposited in the PSD (Projectile Spectator Detector), denoted as E_{PSD}, is used as a measure. Centrality reflects how “head-on”

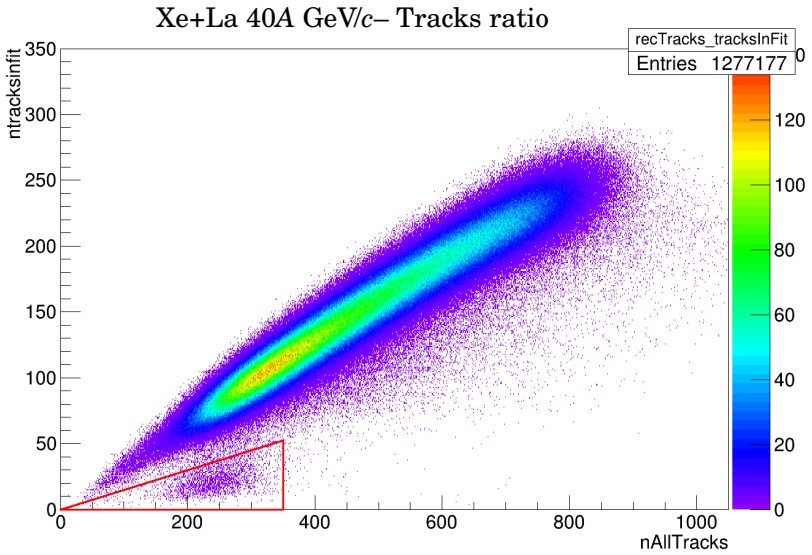

Figure 5.6: Visualization of the cut Xe+La at 40*A* GeV/*c* cut of All tracks vs tracks from main vertex (*Tracks ratio*). The red triangle indicates the cut.

or "central" a collision is, with more central collisions producing higher particle multiplicities and lower spectator energy. In this analysis, only the 0–20% most central Xe+La collisions are selected. This means that events with E_{PSD} values above a certain threshold – corresponding to more peripheral (less central) collisions – are rejected. These threshold values vary with the beam energy and are listed in the associated table. The detailed method for selecting centrality classes in Xe+La collisions is described in Ref. [72].

Table 5.8: PSD centrality selection for 20% central events in Xe+La interactions listed by beam momentum energy.

$\mathbf{p_{beam}}$ [*A* GeV/*c*]	PSD energy, GeV
13	728
19	1063
30	1744
40	2224
75	3716
150	6837

Table 5.9: Percentage of spectators accepted per each beam momenta in simulated data sets to match the 20% centrality of experimental data.

p_{beam}[*A* GeV/*c*]	Number projectile spectators rejected
13	89
19	87
30	83
40	82
75	79
150	67

Simulated data

Energy deposit cannot be directly simulated in Monte Carlo (see Sec. 3.3) simulations. Therefore, to select the same 20% most central events used in the experimental data, the centrality determination in simulated data sets is based on the number of projectile spectator nucleons in the collision. First, the total number of spectators is extracted from the simulation and subtracted from 139, which is the atomic number of Lanthanum. Treating all events as representing 100% of collisions, we then calculate the desired quantiles – in this case, the 20% most central events – based on the number of spectators. The spectator thresholds for each beam energy are listed in Table 5.9. Events with a number of spectators exceeding these thresholds are rejected, ensuring a consistent centrality selection between simulation and experiment.

5.1.2 Track selection

Several selection criteria were implemented to guarantee that the analyzed particles are accurately measured tracks of negatively charged hadrons originating from the primary interaction. The impact of each selection, expressed as a percentage of all tracks remaining in the analyzed datasets, is presented in Table 5.10; some cuts are unavailable or are applied differently to the simulated data sets.

Table 5.10: Track statistics retained after each selection criterion used in this analysis, listed by beam momentum energy

Track selection for h^-, percentage of tracks retained						
$\mathbf{p_{beam}}$**[*A* GeV/*c*]**	13	19	30	40	75	150
Track from main vertex	100	100	100	100	100	100
Tracks fit quality	66.5	65.7	63.2	66.7	65.8	66.38
Charged vertex tracks	64.9	64.0	64.2	65.1	65.1	66.30
Number of clusters	42.2	43.3	40.9	42.2	40.1	39.32
Number of clusters in VTPC	29.5	31.1	30.1	30.2	30.1	30.24
Ratio cut	28.5	27.8	28.9	28.9	29.9	29.02
Distance of closest approach	28.0	28.1	27.8	27.7	26.5	28.37
Transverse momentum	27.9	27.8	27.4	27.5	26.4	28.20
Electron removal	25.5	25.6	25.8	25.6	24.6	26.38
Negative particles	13.3	13.3	14.7	13.5	12.5	12.02
Acceptance map	11.8	10.5	10.9	11.8	11.1	10.83
mTTD	9.5	9.5	9.8	10.5	10.8	9.97

Track fit quality

In particle collision events, not all detected tracks correspond to well-measured particles originating from the main interaction vertex. Additionally, analyzing all charged particles without charge discrimination may dilute the sensitivity to specific physics signals that are more prominent in negatively charged particles.

To improve the data quality of the analysis, only particles with a successfully converged mo-

mentum fit at the main interaction vertex are chosen, ensuring that the selected tracks are well-reconstructed and truly associated with the primary collision.

Number of clusters and clusters in VTPCs

Tracks with too few reconstructed points can result in poor momentum measurement and lower overall track quality, which can compromise the reliability of the analysis. By requiring that each track has more than 30 reconstructed points, the selection guarantees better momentum reconstruction and track quality; in this way, well-measured tracks contribute to the results.

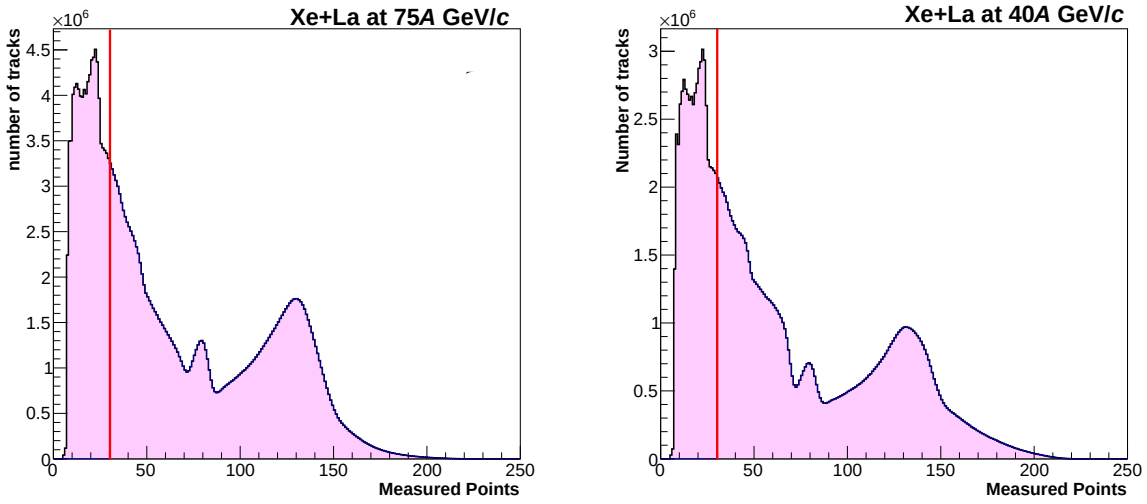

Figure 5.7: Example distribution of the Measured points selection, the red line indicates the value for selected tracks, examples correspond to collisions of Xe+La 75A GeV/c and 40A GeV/c

As reviewed in Sec. 3.2.2, TPCs are the main detectors used for tracking; therefore, a more focused criterion is applied to ensure a decent momentum reconstruction, the sum of the reconstructed points in VTPC-1 and VTPC-2 should be greater than 15.

Potential-point ratio

Split tracks, which occur when a single particle's trajectory is mistakenly reconstructed as multiple segments, can interfere with the data analysis. To reduce this issue, tracks are required to have a ratio of measured clusters to potential clusters across all TPCs between 0.5 and 1.1. This criterion ensures that tracks have a sufficient number of detected clusters relative to what is expected, removing split tracks that typically have a low ratio. The potential clusters were calculated for tracks associated with the main vertex, and Fig. 5.8 illustrates the improvement in the distribution after applying this requirement.

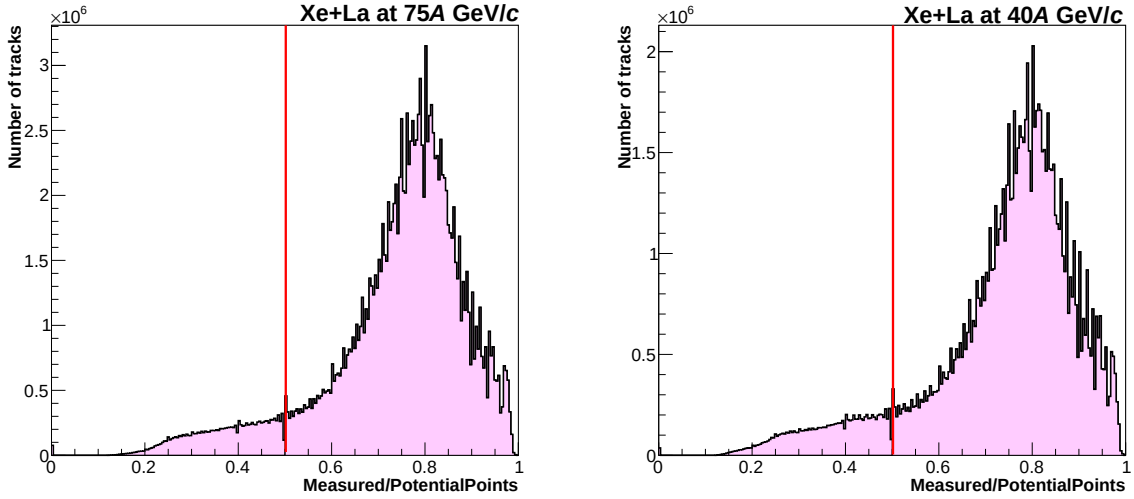

Figure 5.8: Example of the distributions of the potential-point ratio selection, the red line indicates the value of the selection, beam momenta correspond to Xe+La 40A and 75A GeV/c.

Distance of the closest approach

Some tracks do not originate from the main interaction vertex. To ensure that selected tracks truly come from the collision point, the difference between the track's extrapolated position at the target Z coordinate and the reconstructed vertex position in the transverse (X-Y) plane is limited (also known as *also impact parameter*). This track selection criterion enforces that the difference between the track extrapolation to the target Z position and the reconstructed interaction vertex is small enough in the X-Y plane.

It was required to be smaller than 4 cm in the horizontal (bending) plane (b_X) and 2 cm in the vertical (drift) plane (b_Y).

Transverse momenta

Other particles with high transverse momentum are not essential to this analysis; therefore, a window in $|p_x|$ and $|p_y|$ is established, rejecting particles that have transverse momentum values less than 1.5 GeV/c for the current work.

Electron removal

The selection of particles for this analysis is meant to focus primarily on negative particles that are easily detected due to the NA61/SHINE configuration (see See . 3.2). Particles that are not hadrons, like electrons, are not within the scope of this analysis and are rejected. To do this, a very simple cut, a geometrical cut based on the 2-dimensional distribution dE/dx vs $\log_{10} p$. An example of the distribution is shown in Fig. 5.9.

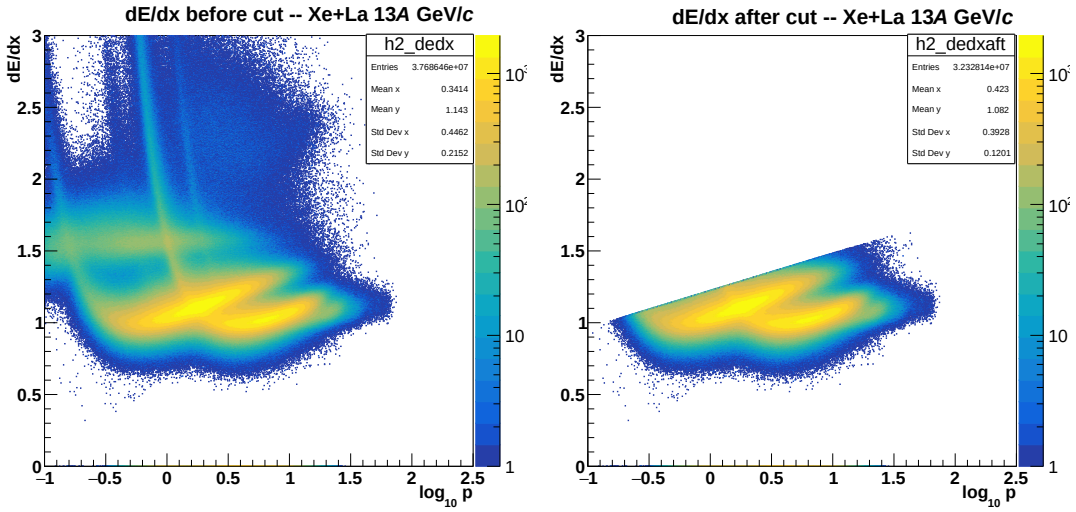

Figure 5.9: Example the 2D dE/dx distribution for Xe+La 13A GeV/c. Left distributions represent the original distribution; the left distribution is the result after the electron removal.

5.1.3 Single-particle acceptance maps

A three-dimensional (y_{cm}, p_x, p_y)[1] acceptance map was constructed to define the momentum region chosen for the analysis. This map was generated by comparing the number of negatively charged hadrons produced in Monte Carlo simulations before and after detector simulation and reconstruction, specifically using the EPOS and EPOS RECONSTRUCTED datasets described in this section. Only bins corresponding to regions with at least 70% of reconstructed particles were included in the acceptance map. An example of such a map, used for negatively charged hadrons intermittency analysis in Xe+La collisions at 150A GeV/c, is shown in Fig. 5.10. Single-particle acceptance maps for negatively charged hadrons in intermittency analysis of other datasets are presented in Ref. [73].

5.1.4 Momentum two-track distance cut

The momentum-based Two-Track Distance cut was introduced in Sec. 5.1.4. In this section, we will elaborate on the specific values and technical issues associated with it.

For convenience, here is a reminder of the steps needed to calculate the mTTD cut for each energy.

1. Calculate two-track distance distribution.
2. Determine the gTTD cut.
3. Examine the mTTD variables after the gTTD cut is implemented in the data set.

[1] Consult Appendix A for details on kinematic variables.

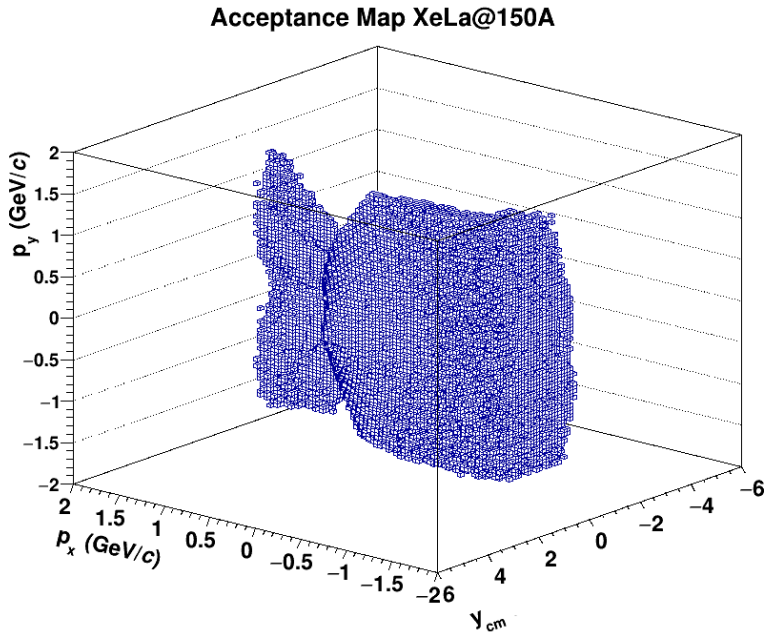

Figure 5.10: Example of single-particle acceptance map for Xe+La collisions at 150*A* GeV/*c* used for h^- intermittency analysis, see text for details.

4. Determine the ellipses, and apply the cut.

The mTTD cut defines the region with reduced efficiency for measuring two tracks in the NA61/SHINE experiment, where it removes remaining split tracks from the data following the potential point ratio selection. For each pair of selected particle candidates in both recorded and mixed events for Xe+La at 13*A*, 19*A*, 30*A*, 40*A*, 75*A*, and 150*A* GeV/*c*.

The TTD represents the average distance between tracks in the x-y plane at eight distinct z-planes (-506, -255, -201, -171, -125, 125, 352, and 742 cm). By applying the geometrical two-track distance cut, we reject pairs below the desired value in the distributions and start the study in momentum variables (See Fig. 5.11).

Then we study the variables obtained from this cut and get the main ellipses in these coordinates; see Fig. 5.12 *(left)*. Pairs with momentum inside the final three parametrized ellipses must be rejected. In Table 5.1.4, the mTTD values for each energy are displayed. Final ellipses examples can be seen in Fig. 5.12 (*right*).

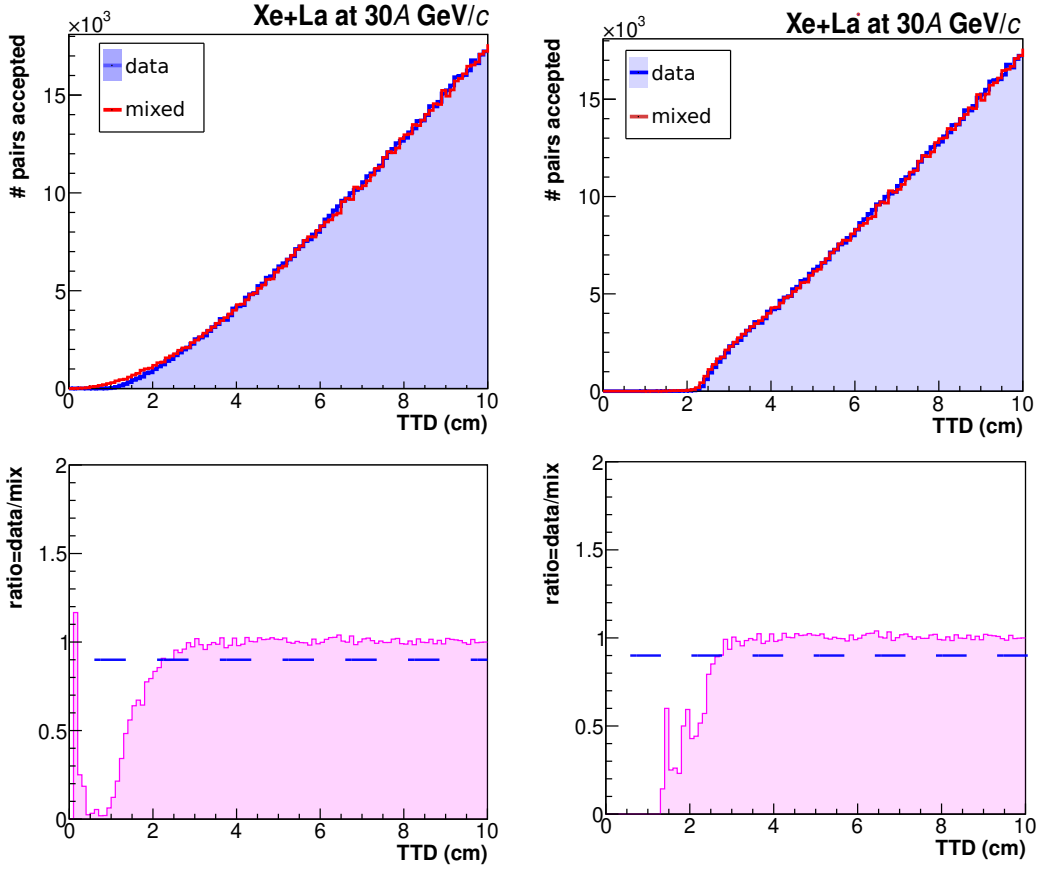

Figure 5.11: Example of the momentum Two-Track distance distribution and ratio of data/mixed before the rejection (left), and after the rejection (right).

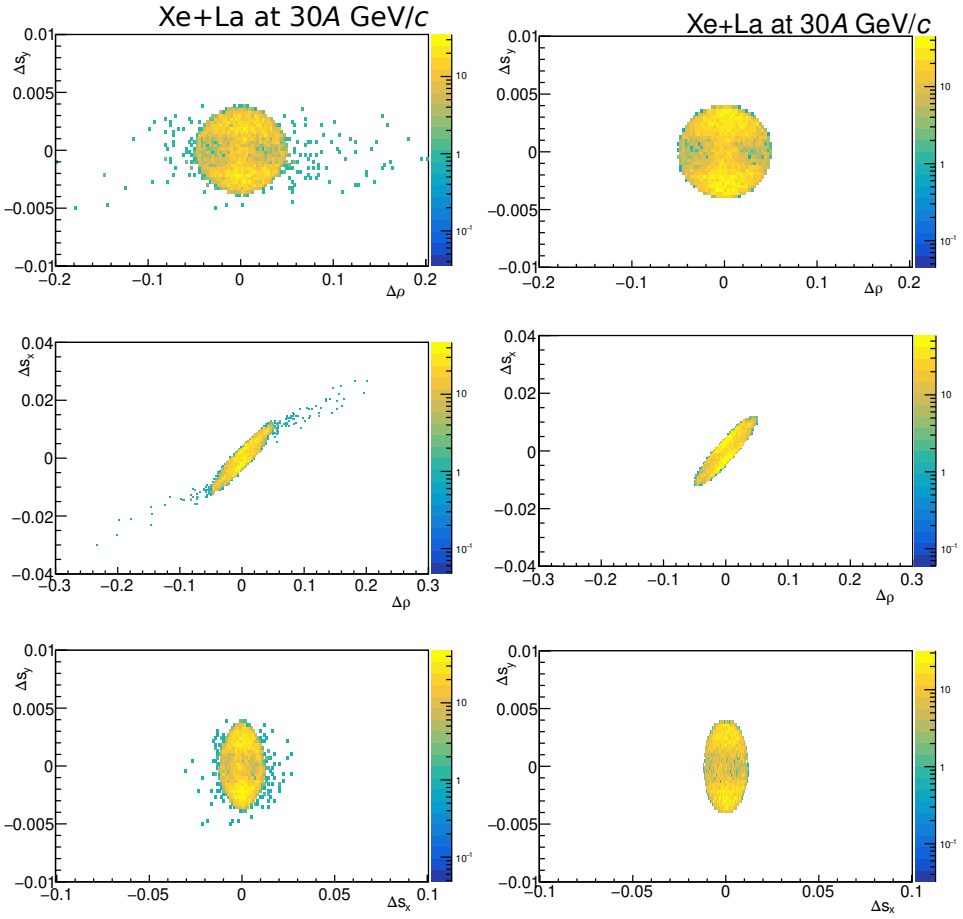

Figure 5.12: Examples of the distributions studied to obtain parametrized values in momentum coordinates obtained after applying the gTTD cut. Examples correspond to Xe+La at 30*A* GeV/*c*.

mTTD ellipse parameters Xe+La						
$\mathbf{p_{beam}}$**(*A* GeV/*c*)**		13	19	30	40	75
gTTD value (cm)		3.2	2.7	2.3	2.3	2.5
$\Delta\rho\Delta s_x$	r_1	0.17	0.098	0.055	0.042	0.027
	r_2	0.006	0.006	0.0045	0.0045	0.0049
	θ	5.3	7.8	12.8	16.6	30.5
$\Delta s_x\Delta s_y$	r_1	0.018	0.015	0.013	0.012	0.014
	r_2	0.005	0.0044	0.004	0.004	0.0043
	θ	0	0	0	0	0
$\Delta\rho\Delta s_y$	r_1	0.155	0.093	0.05	0.038	0.021
	r_2	0.005	0.0045	0.0039	0.004	0.0044
	θ	0	0	0	0	0

5.1.5 Systematic uncertainties

The systematic uncertainties of the results obtained are addressed by independently modifying selected biasing selection criteria from the ones described in Sec. 5.1.2. The complete analysis is performed with the selected alteration, and then the results are compared to those obtained with nominal selection values. Typically, two modifications for each selection criterion are defined: *tight*, with a more constraining value than nominal, and *loose*, which is less constraining than the nominal value.

The following alterations were selected for this analysis:

Event selection	nominal value	tight	loose
Beam off-time particles	4 μs	-2	+2

Track selection	nominal value	tight	loose
Number of VTPC clusters	15	-5	+5

To perform a quality evaluation on the effect of a given selection criterion on a parameter, a common method used in high-energy physics was performed, known as *The Barlow method* [74]. In short, this method introduces a quantitative comparison of the varied values to the statistical errors obtained in the results and checks if the error introduced by the varied value is significant or not. If yes, it proposes the calculation of the systematic error.

If the difference between standard and varied value is *larger than their statistical error difference*, i.e:

$$|P^{nom} - P^{var}| > \sqrt{|\sigma^2[P^{nom}] - \sigma^2[P^{var}]|} \quad ,$$

Then, the selection criteria introduced a systematic uncertainty to the parameter, and the systematic error must be calculated. The systematic uncertainty from the i-th source *(selection criteria)* for the j-th variation *(tight, loose)* is:

$$\sigma^j_{sys,i}[P] = \sqrt{|P^{def} - P^{var}|^2 - |\sigma^2[P^{def}] - \sigma^2[P^{var}]|^2} \quad ,$$

and the different settings for the i-th source:

$$\sigma_{\mathrm{sys},i}[P] = \sqrt{\left[\sum_{i=1}^{m}\left(\sigma^{i}_{\mathrm{sys},i}[P]\right)^2\right] \Big/ m} \quad ,$$

where m is the number of cut variations for the given cut, the overall systematic uncertainty from n systematic sources is:

$$\sigma^{\mathrm{tot}}_{\mathrm{sys}}[P] = \sqrt{\sum_{i=1}^{n}\sigma^{2}_{\mathrm{sys},i}[P]}\,.$$

The total uncertainty is calculated as the sum in quadrature of the statistical uncertainties and systematic uncertainties.

$$\sigma_{total} = \sqrt{\sigma^{2}_{stat} + \sigma^{2}_{sys}}\,.$$

The next chapter includes a section where the impact of the systematic uncertainties is compared to the statistical uncertainties before the calculation of the total uncertainty for this analysis.

CHAPTER 6

RESULTS ON SCALED FACTORIAL MOMENTS

This chapter presents the results of the SFMs of order $r = 2, 3, 4$ (see Eq. 4.1), for selected negatively charged hadrons produced within the analysis acceptances (see Sec. 5.1.2) in central (0–20%) ^{129}Xe+^{139}La collisions at beam momentum 13A, 19A, 30A, 40A, 75A and 150A GeV/c. All the mentioned cuts in Sec. 5.1.1 and Sec. 5.1.2 were applied to the present data sets.

The analysis investigates the dependence of SFMs on the number of subdivisions, M^2, in transverse-momentum space – an approach central to intermittency studies (see Chapter 2) using p_T binning and cumulative p_T binning analyzed. Independent data sets were used for each subdivision level (see Sec. 4.2), and statistical uncertainties were evaluated using standard uncertainty propagation methods (see Sec. 4.2).

The scaling behavior of $\Delta F_r(M)$ and $\Delta F_r(M)_c$ (see Sec. 4.1.2 and 4.1.3) as a function of M^2 was examined up to a maximum subdivision of $M = 150$. Additionally, a finer subdivision of $M = 32$ was introduced to reduce the impact of experimental momentum resolution effects. An insightful and complementary review of the multiplicity distributions can be found in Appendix A.

This chapter is organized as follows. First, several introductory plots pertinent to the two-particle correlation function are presented. Next, we display the results of the Scaled Factorial Moments (SFMs) with statistical uncertainties for the two methodologies detailed in the previous chapter. Subsequently, a subsection provides the results, including systematic uncertainties. Finally, all results are shown together with the combined final uncertainties. A discussion of these results is deferred to the concluding chapter. Point values of the plots in this section are available upon request.

6.1 Two-particle correlation function

As defined in Sec. 4.4, in this section, the results for the correlation functions of Δp_T as defined by eq. 4.4 are presented, for the data sets of Xe+La at $13A$, $19A$, $30A$, $40A$, $75A$, and $150A$ in Fig. 6.1. A small hill can be appreciated at all colliding energies, followed by a flat form. The hill at small values of Δp_T is the expected form of short-range correlations.

In Fig. 6.2, we present the results for the correlation function of q_{LCMS} defined by Eq. 4.4, for the same data sets; again, a small hill followed by a flat distribution is seen, which is the expected form of this correlation function in the presence of short-range correlations.

The presence of short-range correlations of HBT type has been reported in other intermittency phase-spaces as discussed in Chapter 2, and it was associated to a rising behaviour on SFMs althought similar plots to the ones presented in this thesis are not available within the scope of those analysis, this two-particle correlation functions are broadly studied in other analysis methodologies, in particular in Femtoscopy analysis, where q_{LCMS} is a variable better understood and key for the specific purposes of them.

It has also been discussed that a power-law in intermittency will also present a sharp peak within these correlation functions in the first bin, and was introduced in Chapter 3 Sec. 2.2. A proof and wider discussion of this will be presented in the next chapter when we compare the obtained results with the Power-law model.

Δp_T correlation function

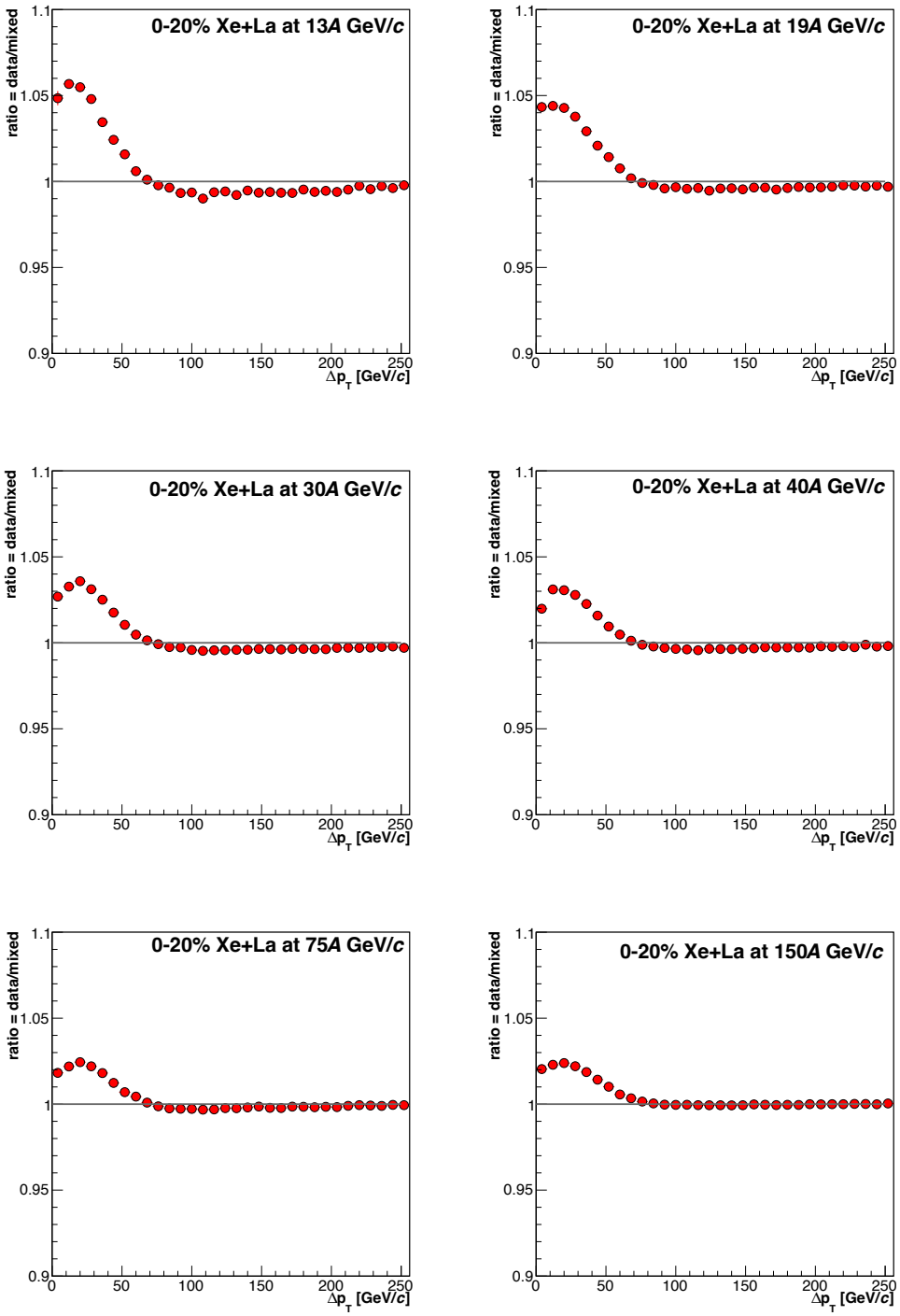

Figure 6.1: Δp_T correlation function of Xe+La energy scan, beam momentum energies: 13A, 19A, 30A, 40A, 75A, and 150A GeV/c, hill presented is associated with the presence of short-range correlations.

q_{LCMS} correlation function of Xe+La energy scan

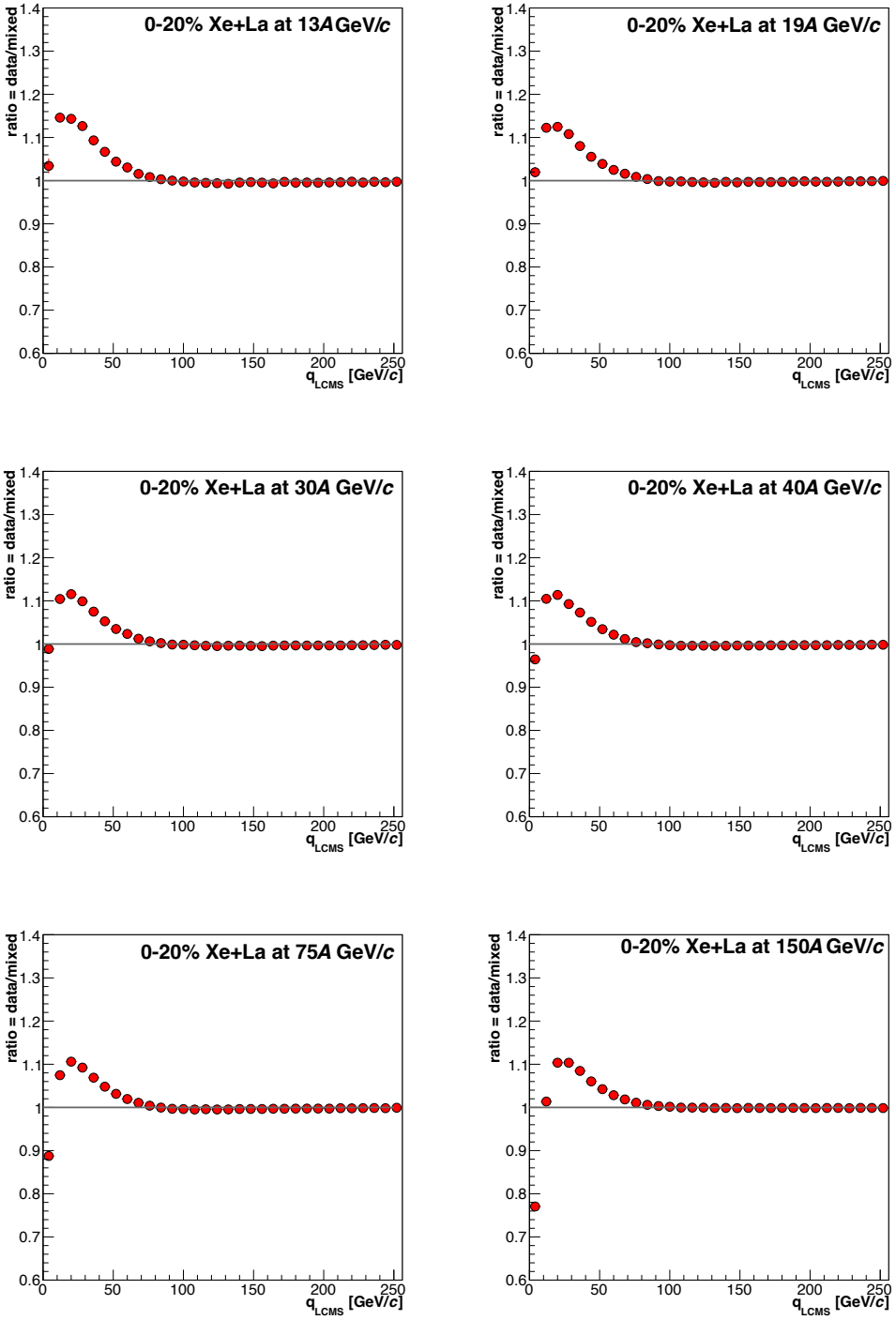

Figure 6.2: q_{LCMS} correlation function of Xe+La energy scan, beam momentum energies: 13A–150A GeV/c, hill presented is usually studied in the scope of HBT analysis like Femtoscopy.

6.2 Results with statistical values

Transverse momentum binning

The results on $\Delta F_r(M)$ (see Eq. 4.8) for subdivisions in p_T binning are displayed in Figs. 6.3 – 6.8. The results shown on the left of each column correspond to full binning (M up to 150), whereas the results shown on all right columns correspond to fine binning (M up to 32).

The first results obtained were those corresponding to Xe+La at 150A GeV/c, a system characterized by possessing very high multiplicity and a colliding energy similar to that of the STAR experiment (see Sec. 2.9 and appendix A). The premise of STAR collaboration was the report of an increase in the SFMs with bin size, which were very similar to a power-law signal [39].

At the same time, NA61/SHINE was reporting results on proton intermittency in Ar+Sc collisions at 13A–150A GeV/c, and Pb+Pb 150A GeV/c (see Sec. 2.8 or [23], [41]) and never reported seeing such a similar increase.

It was not until the present analysis, Xe+La at 150A GeV/c, that the NA61/SHINE collaboration was able to study a very similar and unexpected increase, displayed in Fig. 6.8. In the left column, we see the results for full M^2 binning, in the right column, the results for the short M^2 binning. In the left column, it is clear that there is an increase from point $M^2 = 1$ to $M^2 = 2500$, but this increase stops for larger values of M^2. The right column can be understood as a "zoom" on the interesting region from the left column, where we see a clear increase of $\Delta F_2(M)$ with M^2.

This *increase* is a behavior that propagates with higher order moments of SFMs, as shown in the same Fig. 6.3, middle and bottom columns. Furthermore, this behavior propagates even to lower energies of Xe+La interactions (see Figs. 6.3 – 6.8).

Xe+La at 13*A* GeV/*c*

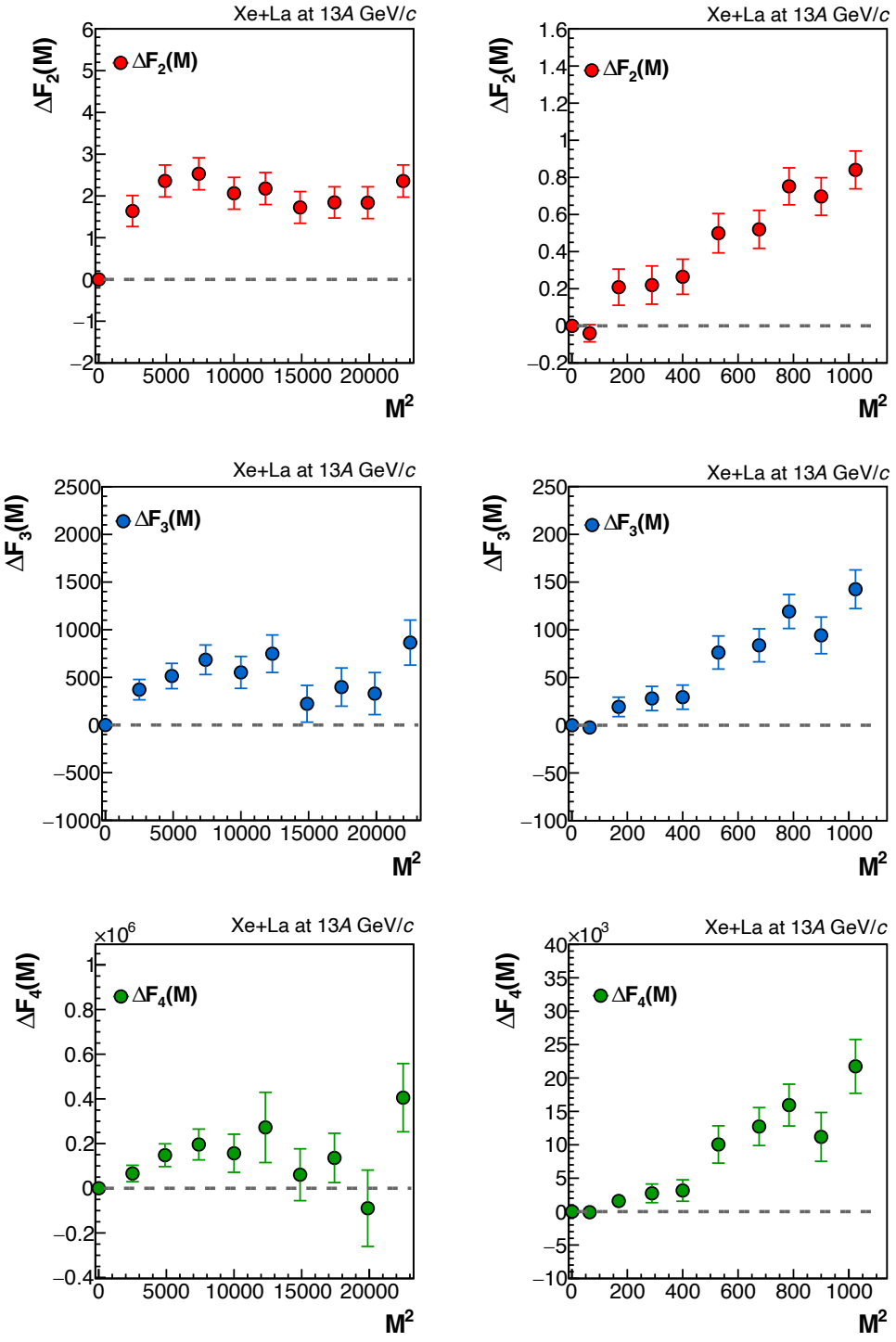

Figure 6.3: Results on the dependence of $\Delta F_r(M)$ of negatively charged hadrons multiplicity, the number of subdivisions in transverse momentum space M^2 is $1 \leq M^2 \leq 150$ on the left panel, and a magnification $1 \leq M^2 \leq 32$ on the right panel. Only statistical uncertainties are indicated.

Xe+La at 19*A* GeV/*c*

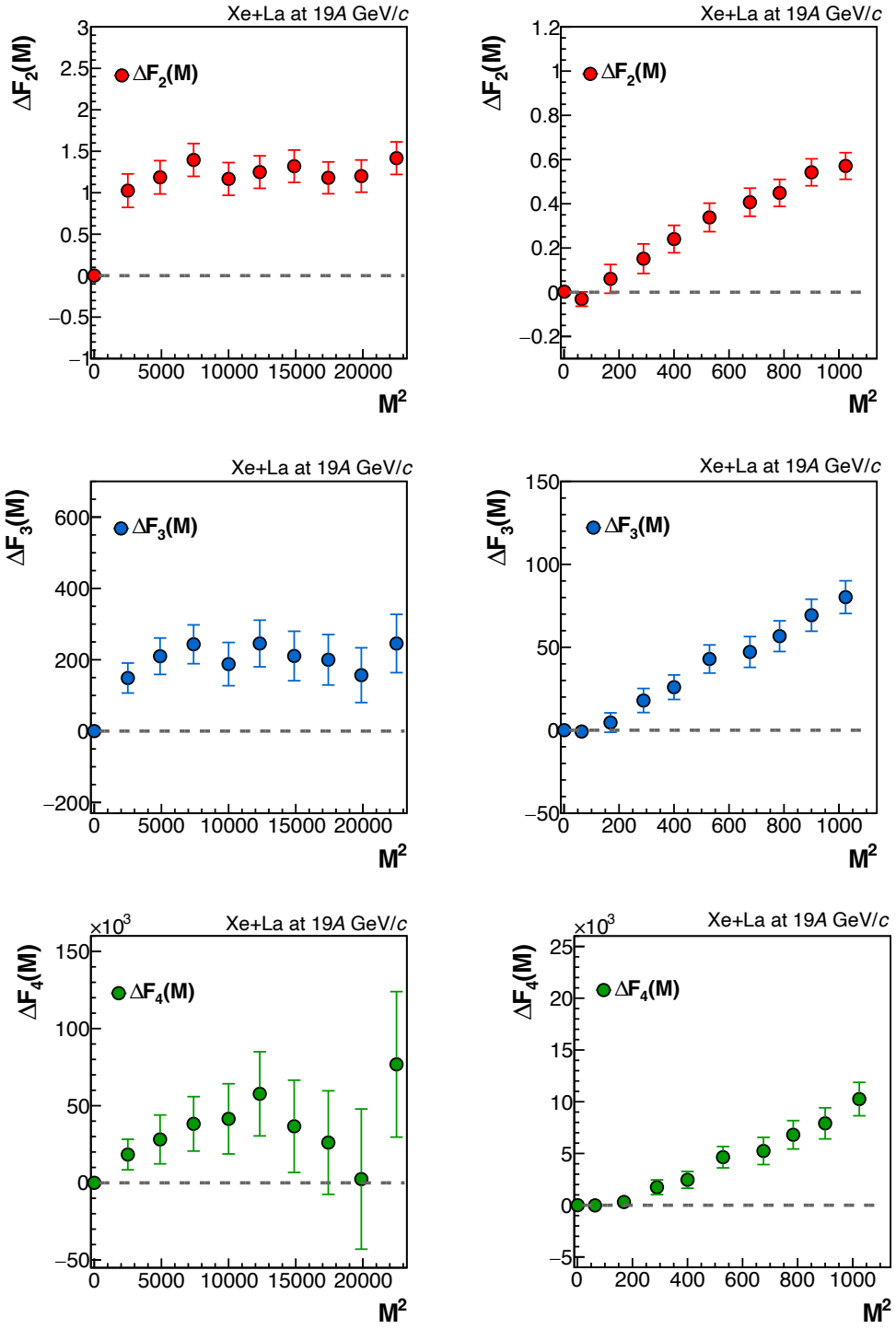

Figure 6.4: Results on the dependence of $\Delta F_r(M)$ of negatively charged hadrons multiplicity, the number of subdivisions in transverse momentum space M^2 is $1 \leq M^2 \leq 150$ on the left panel, and a magnification $1 \leq M^2 \leq 32$ on the right panel. Only statistical uncertainties are indicated.

Xe+La at 30*A* GeV/*c*

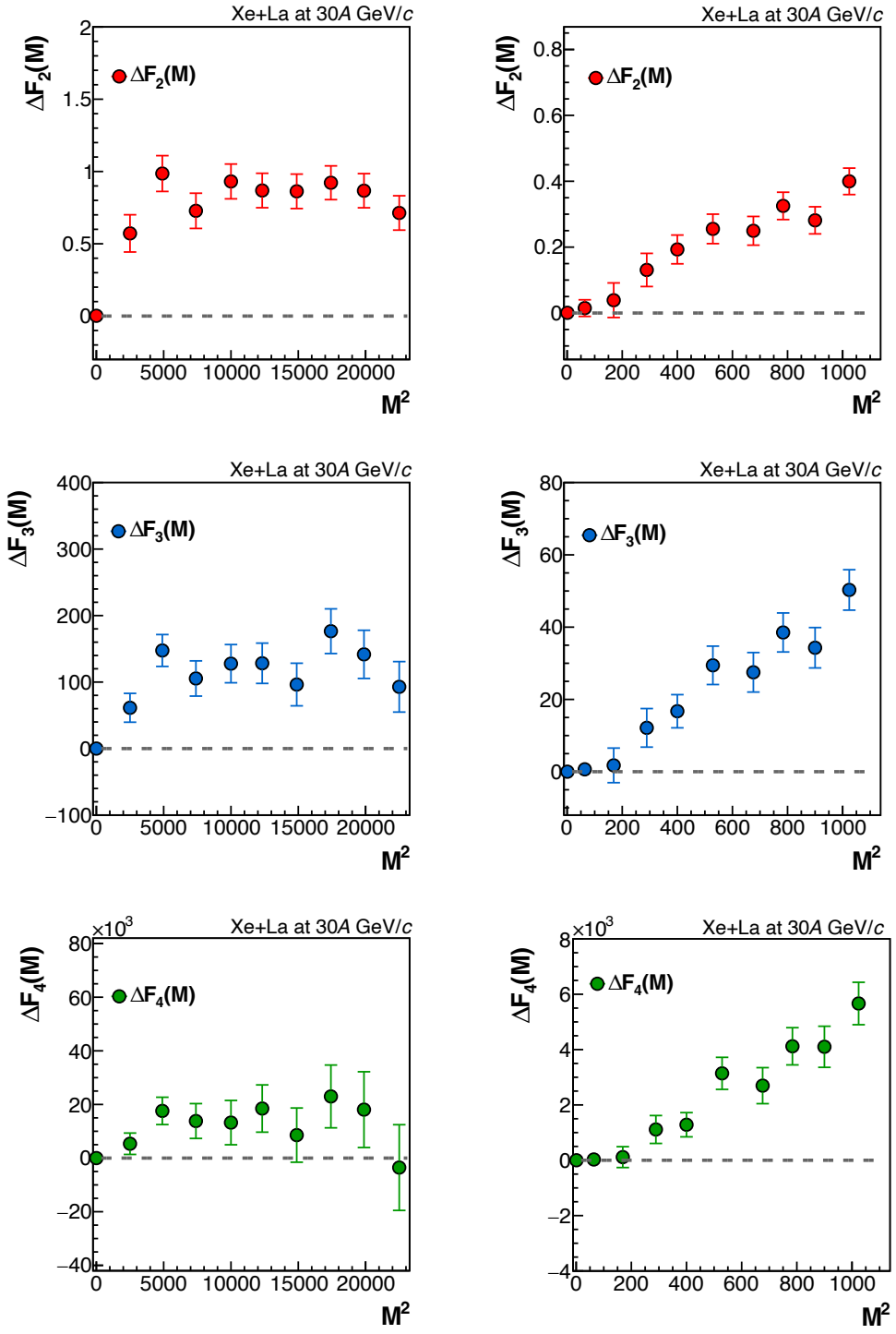

Figure 6.5: Results on the dependence of $\Delta F_r(M)$ of negatively charged hadrons multiplicity, the number of subdivisions in transverse momentum space M^2 is $1 \leq M^2 \leq 150$ on the left panel, and a magnification $1 \leq M^2 \leq 32$ on the right panel. Only statistical uncertainties are indicated.

Xe+La at 40*A* GeV/*c*

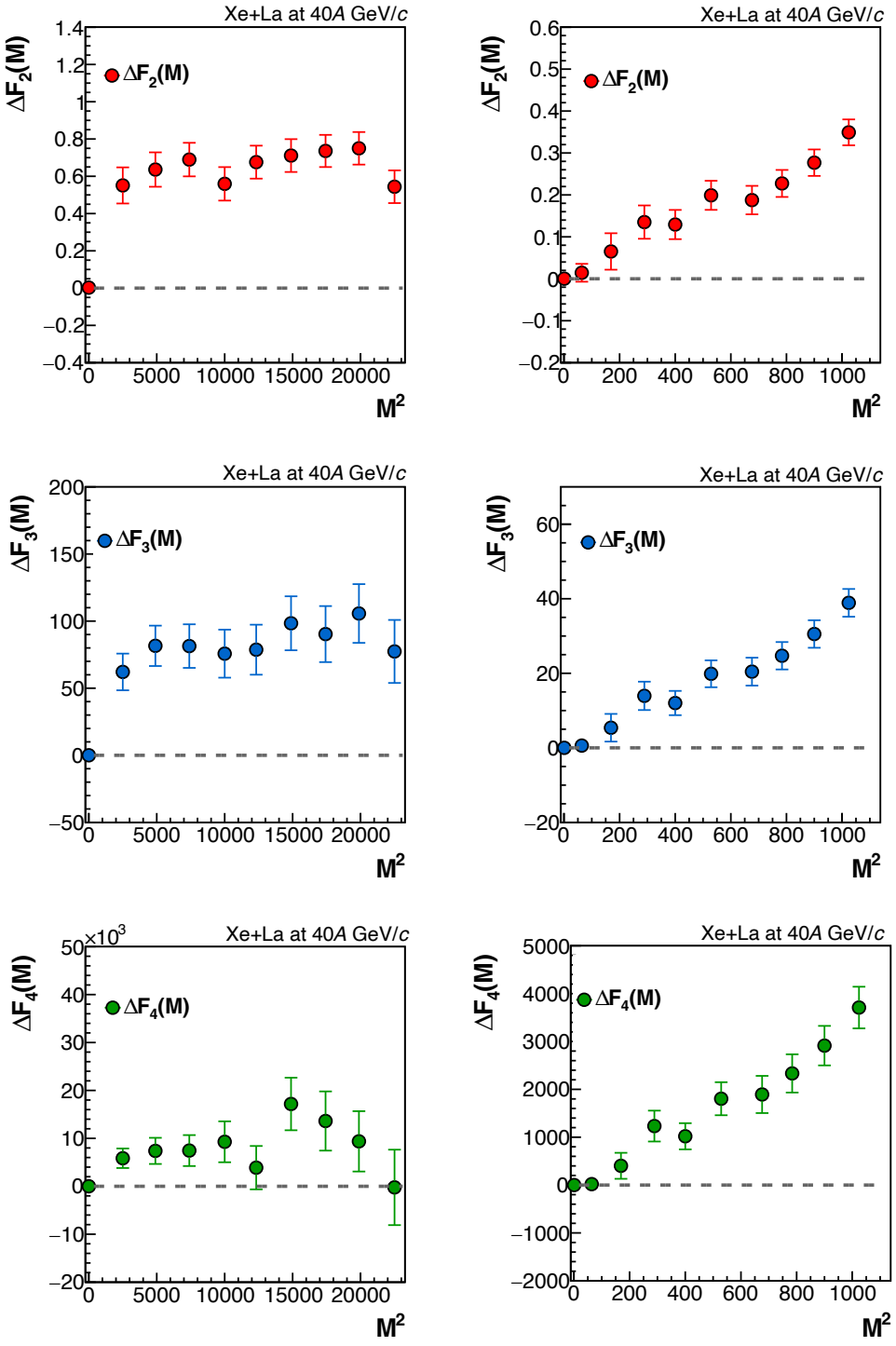

Figure 6.6: Results on the dependence of $\Delta F_r(M)$ of negatively charged hadrons multiplicity, the number of subdivisions in transverse momentum space M^2 is $1 \leq M^2 \leq 150$ on the left panel, and a magnification $1 \leq M^2 \leq 32$ on the right panel. Only statistical uncertainties are indicated.

Xe+La at 75*A* GeV/*c*

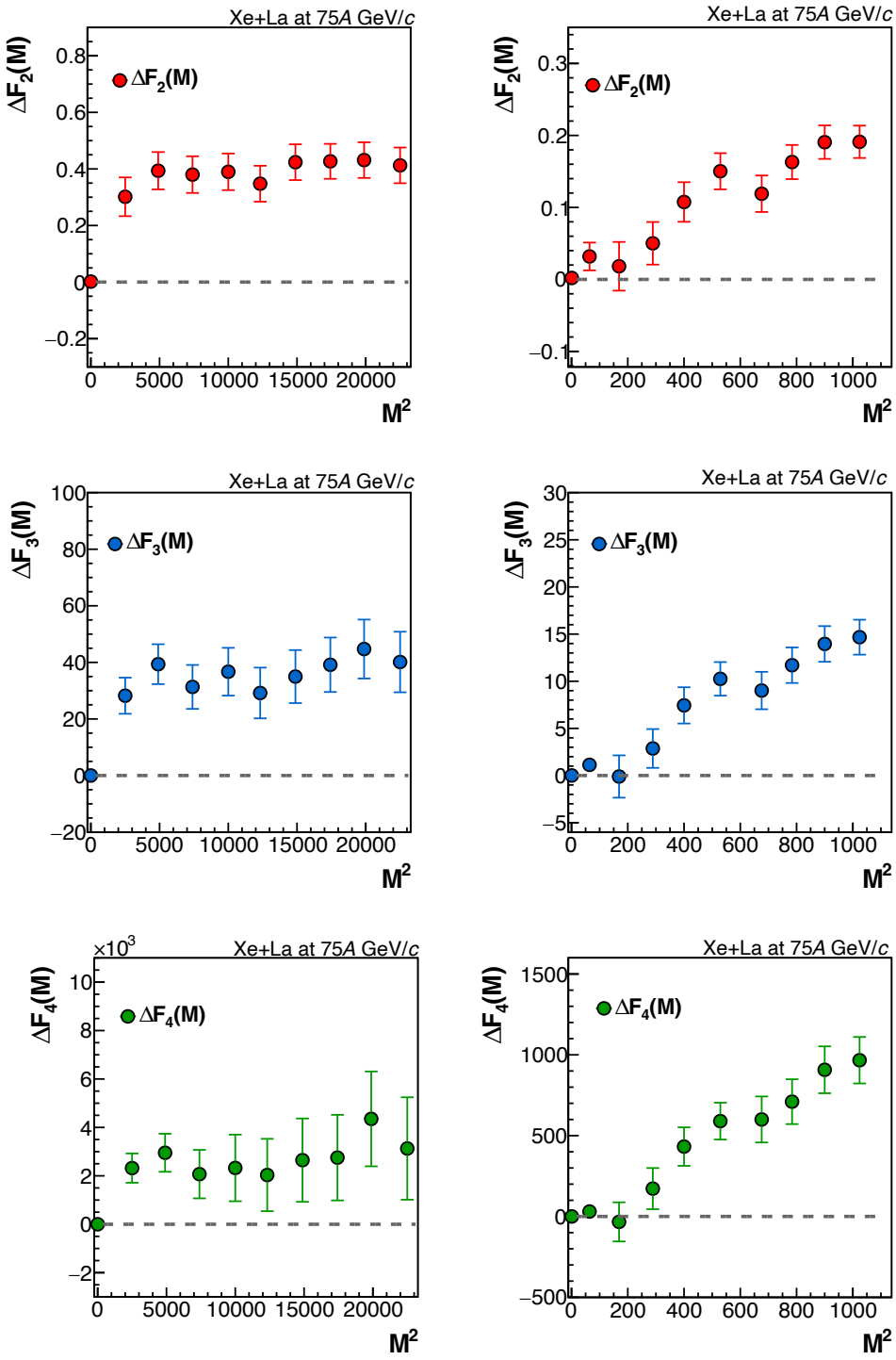

Figure 6.7: Results on the dependence of $\Delta F_r(M)$ of negatively charged hadrons multiplicity, the number of subdivisions in transverse momentum space M^2 is $1 \leq M^2 \leq 150$ on the left panel, and a magnification $1 \leq M^2 \leq 32$ on the right panel. Only statistical uncertainties are indicated.

Xe+La at 150*A* GeV/*c*

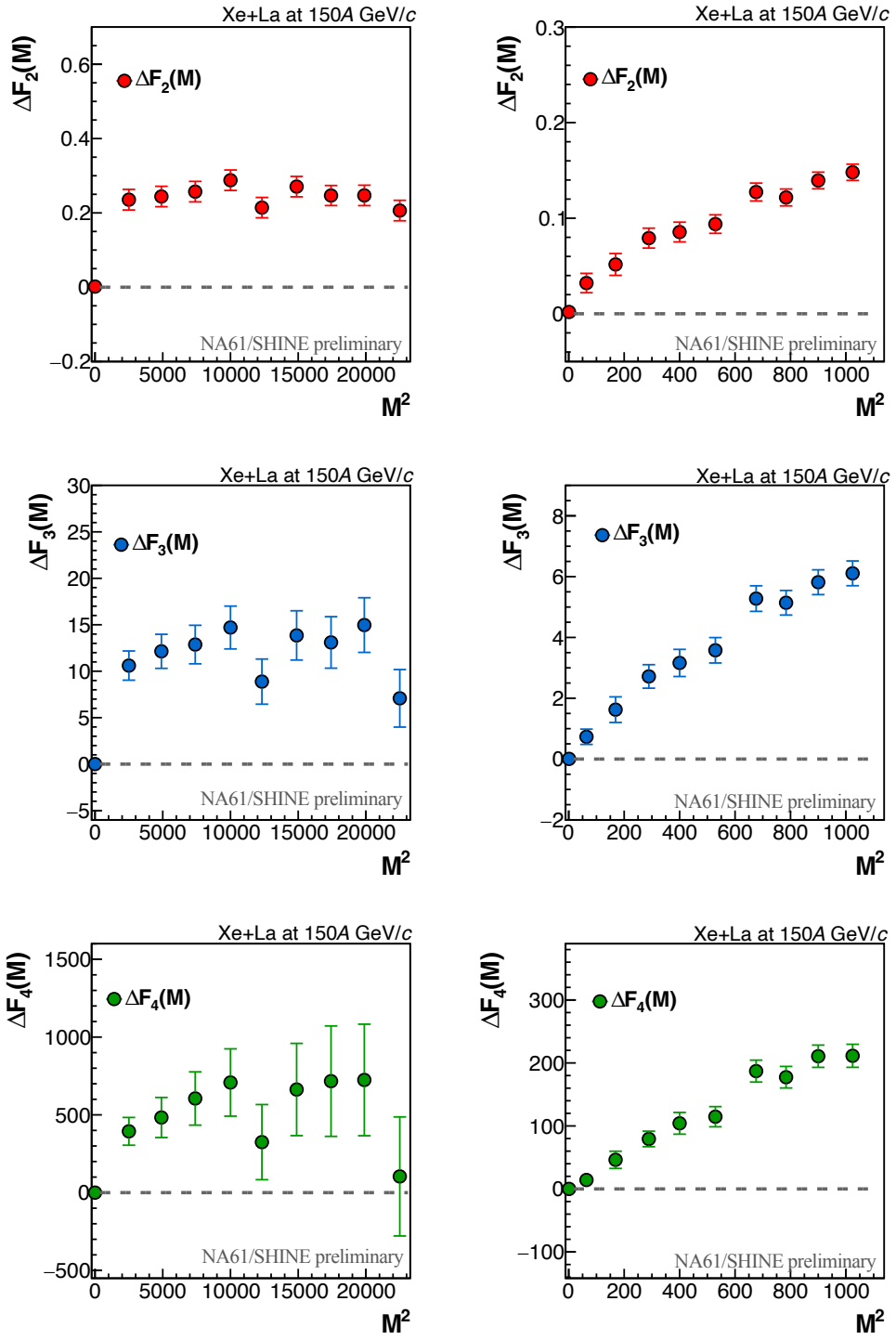

Figure 6.8: Results on the dependence of $\Delta F_r(M)$ of negatively charged hadrons multiplicity, the number of subdivisions in transverse momentum space M^2 is $1 \leq M^2 \leq 150$ on the left panel, and a magnification $1 \leq M^2 \leq 32$ on the right panel. Only statistical uncertainties are indicated.

Cumulative transverse momentum binning

The results on $\Delta F_r(M)_c$ (see Eq. 4.8) for subdivisions in p_T binning are displayed in Figs. 6.9 – 6.14. The results shown on the left of each column correspond to full binning (M^2 up to 150), whereas the results shown on all right columns correspond to fine binning (M^2 up to 32), meaning that the right columns are magnifications of the first two points of the left plots; therefore, scales are increased for the right panel plots.

For $M^2 > 2500$, the observed values of $F_r(M)$ are consistently lower than $F_r(M = 1)$, a trend attributed to anti-correlations introduced by the application of the mTTD cut. These findings indicate that both the mTTD and gTTD cuts systematically suppress $F_r(M)$ values for $M^2 = 2500$ in cumulative transverse-momentum space. It is important to note that the mTTD cut is essential for correcting for detector inefficiencies, specifically those arising from closely spaced track losses (see Sec. 5.1.4).

The main difference here, not seen in other NA61/SHINE intermittency analyses, is how different the results are with p_T binning compared to those results in cumulative p_T binning. (see Sec. 4.1.3). The first results displayed an increase of $\Delta F_r(M)$ with M^2, while the results obtained after applying the cumulative transformation do not display any increase at all of $\Delta F_r(M)_c$ with M^2 (see Eq. 4.1.3). The following statements remain valid:

- Cumulative transformation eliminates the dependence of intermittency parameters on the shape of the single-particle distribution.
- Importantly, it has also been demonstrated in [43] that this transformation preserves the essential features of critical behavior.

Therefore if the increase seen in Xe+La results using p_T binning in previous section (see Sec. 4.1.2) was due to critical behavior (or the Critical Point itself) the increase will hold in the results after applying the cumulative transformation $\Delta F_r(M))_c$ with M^2, the results in this section are rather around the zero-line for all SFMs as can be seen from Figs. 6.9– to 6.14.

We cannot attribute the reported increase in the previous section to critical behavior, but we cannot deny it entirely. As discussed in Sec. 2.2, the method involves counting particles within each M^2 bin to identify pairs, triplets, and quadruplets in the p_x, py phase space. However, following the application of the cumulative transformation, the spatial configuration of particles is significantly altered. This rearrangement can change the number of identified pairs, triplets, and quadruplets within each bin.

Given the particle multiplicity in the original dataset and the definition provided in Sec. 2.2, the transformed distribution may not retain a sufficient number of particles within a single M^2 bin

to reconstruct the same higher-order combinations. Consequently, certain plots expected in this section may be absent due to the absence of such groupings and are therefore omitted.

This effect becomes particularly evident in cases involving fine binning, such as $M^2 = 20000$. After the cumulative transformation, detailed in Sec. 4.1.3, the spatial redistribution can split previously co-located particle groupings across adjacent cells. For example, a triplet that originally occupied one bin may be divided such that two particles remain in one cell and the third is shifted to a neighboring cell. In this scenario, only a single pair can be formed in the first cell, while the second contains no pairs or triplets. As a result, the formation of triplets or quadruplets becomes unfeasible at such high cell resolutions.

Xe+La at 13*A* GeV/*c*

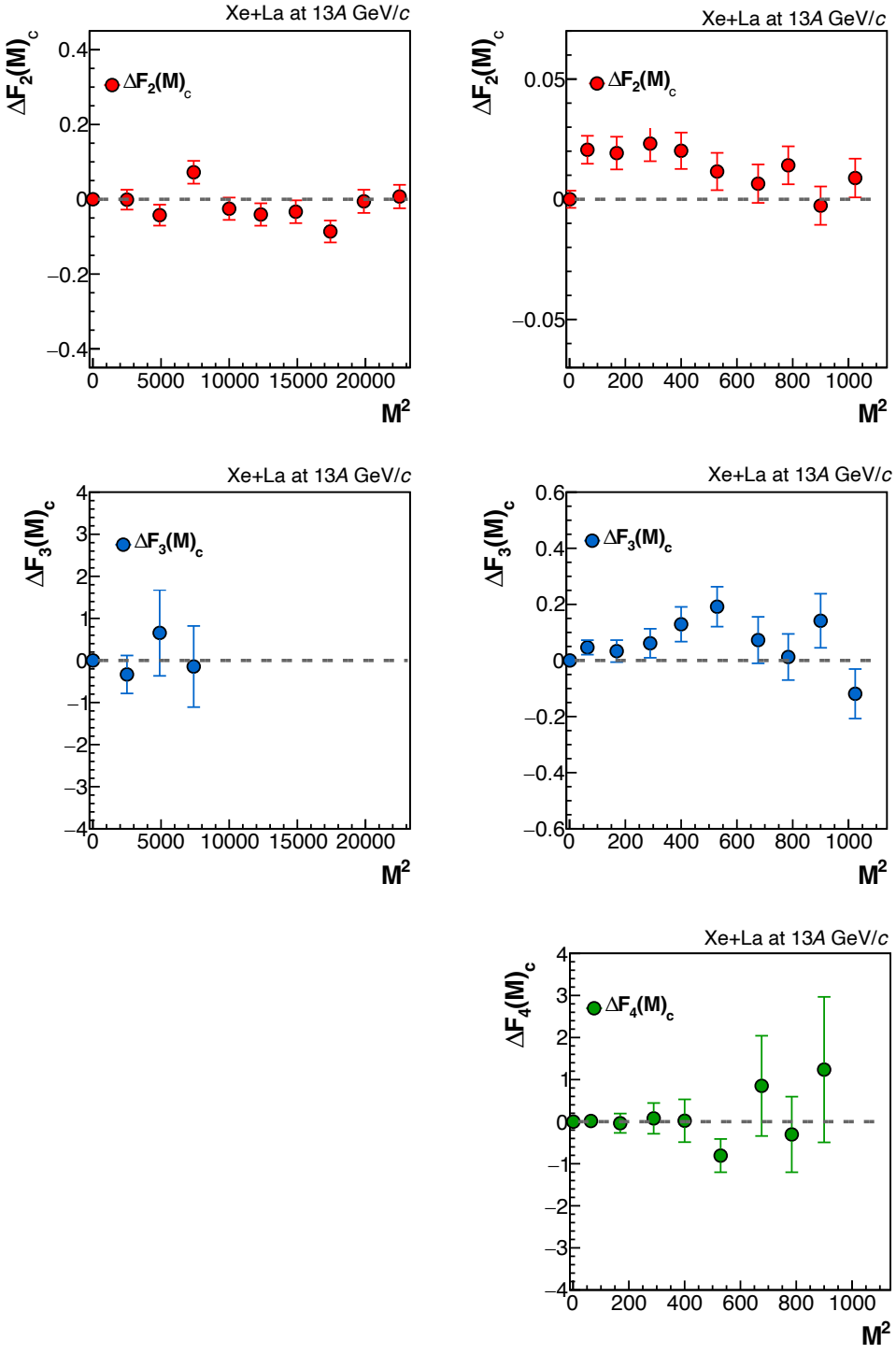

Figure 6.9: Dependence of $\Delta F_r(M)_c$ on negatively charged hadron multiplicity as a function of transverse momentum space subdivisions M^2, with $1 \leq M^2 \leq 150$ (left, if available) and $1 \leq M^2 \leq 32$ (right). Only statistical uncertainties are shown.

Xe+La at 19*A* GeV/*c*

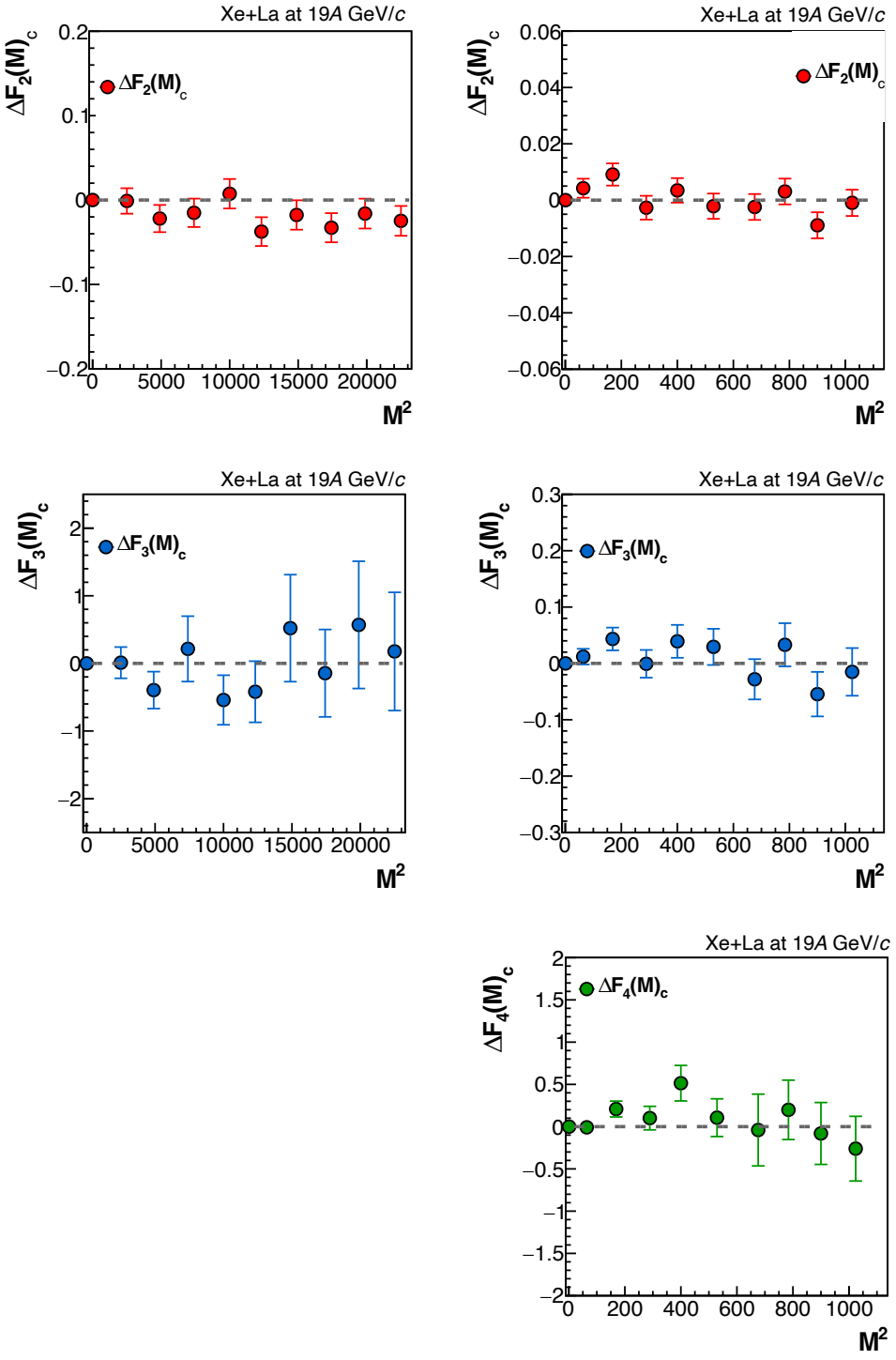

Figure 6.10: Dependence of $\Delta F_r(M)_c$ on negatively charged hadron multiplicity as a function of transverse momentum space subdivisions M^2, with $1 \leq M^2 \leq 150$ (left, if available) and $1 \leq M^2 \leq 32$ (right). Only statistical uncertainties are shown.

Xe+La at 30*A* GeV/*c*

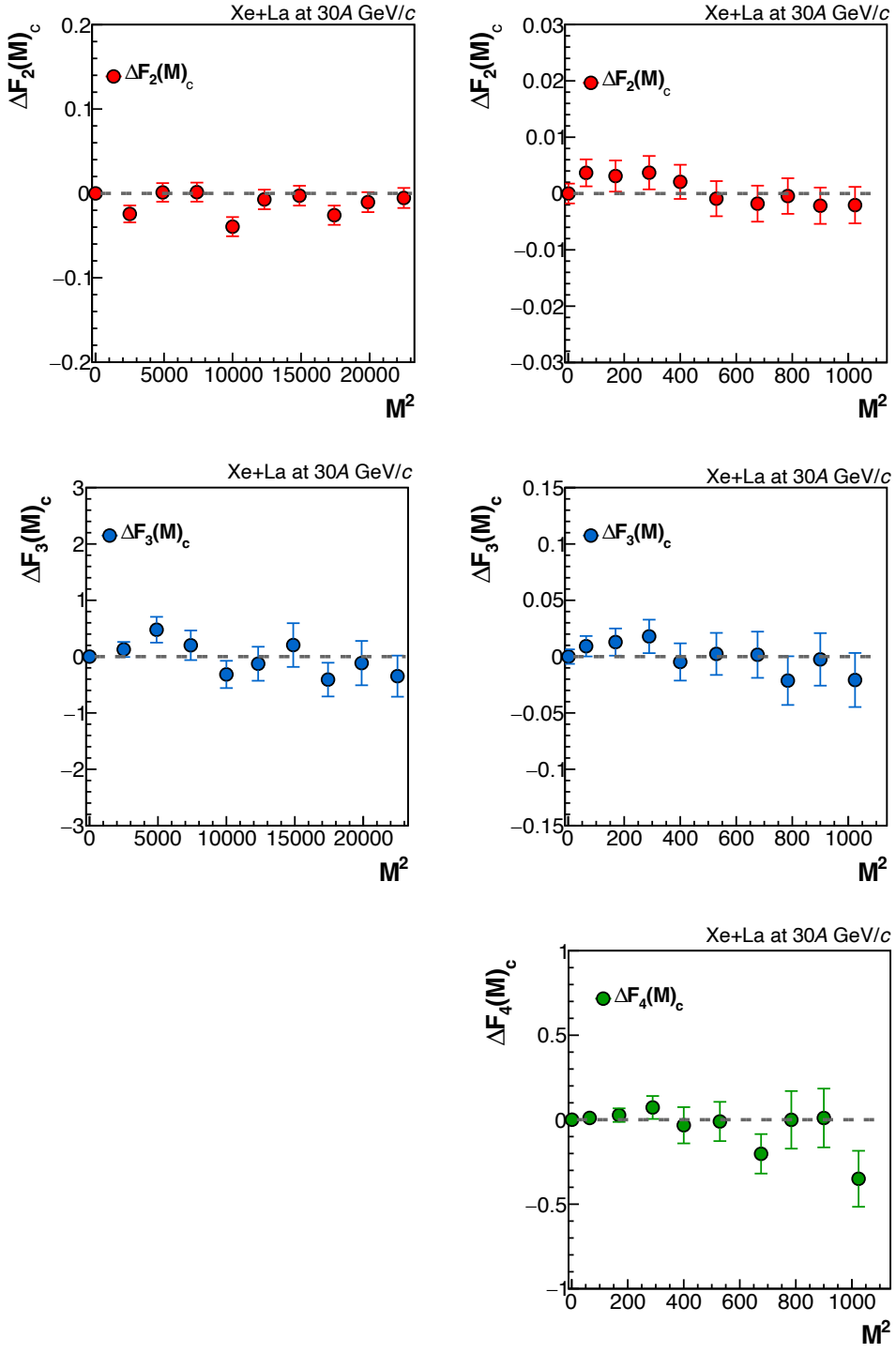

Figure 6.11: Dependence of $\Delta F_r(M)_c$ on negatively charged hadron multiplicity as a function of transverse momentum space subdivisions M^2, with $1 \leq M^2 \leq 150$ (left, if available) and $1 \leq M^2 \leq 32$ (right). Only statistical uncertainties are shown.

Xe+La at 40*A* GeV/*c*

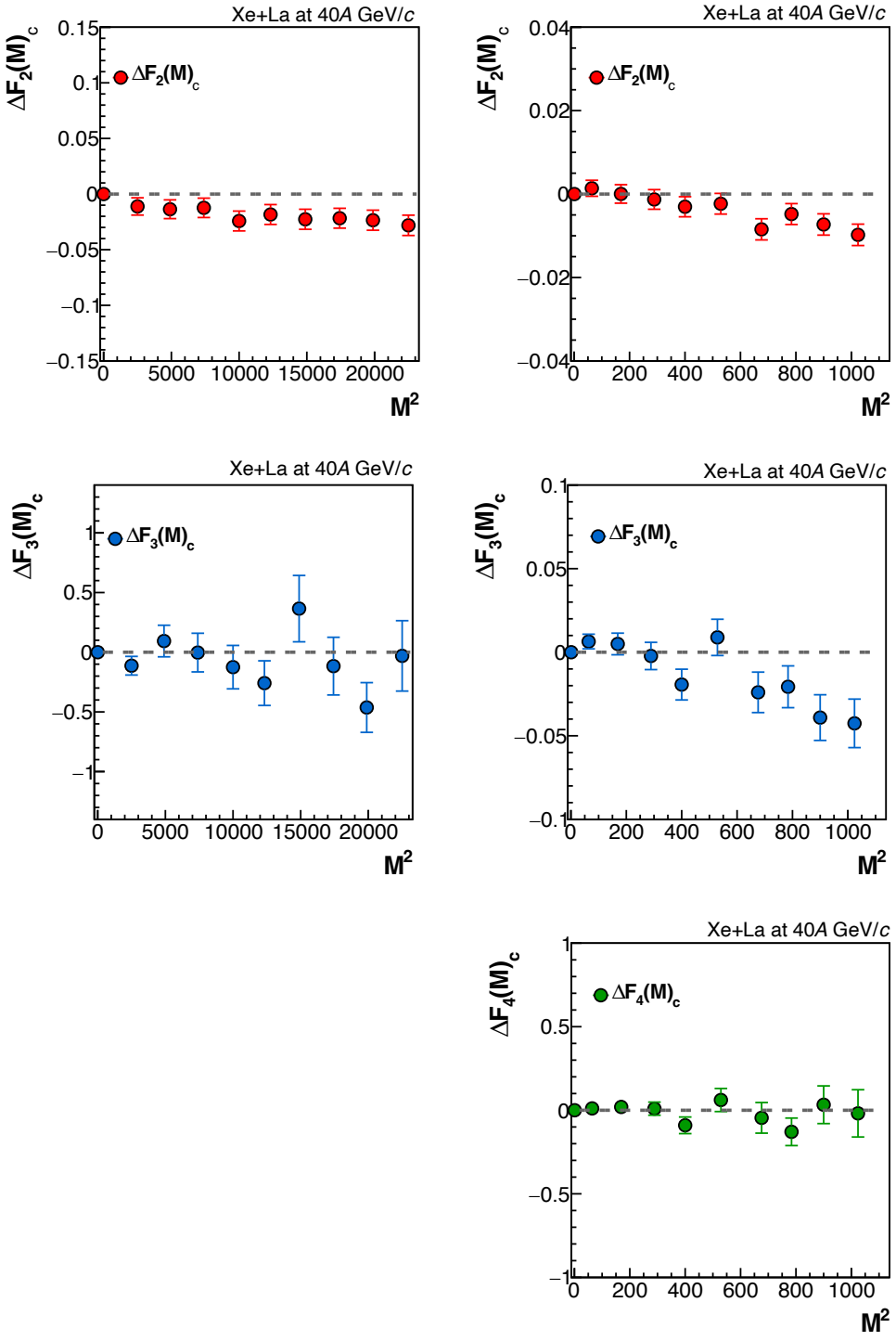

Figure 6.12: Dependence of $\Delta F_r(M)_c$ on negatively charged hadron multiplicity as a function of transverse momentum space subdivisions M^2, with $1 \leq M^2 \leq 150$ (left, if available) and $1 \leq M^2 \leq 32$ (right). Only statistical uncertainties are shown.

Xe+La at 75*A* GeV/*c*

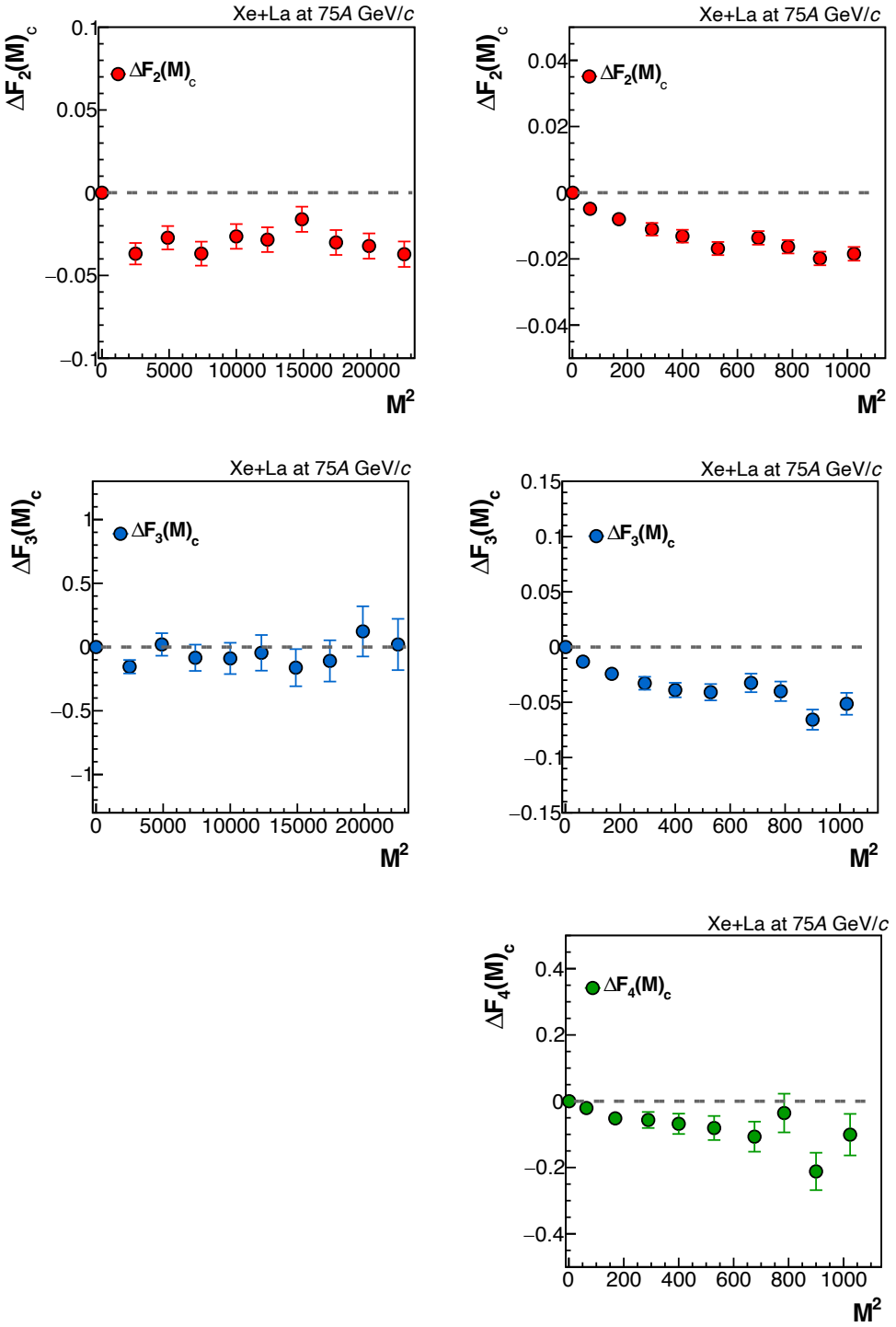

Figure 6.13: Dependence of $\Delta F_r(M)_c$ on negatively charged hadron multiplicity as a function of transverse momentum space subdivisions. Only statistical uncertainties are shown; some may be smaller than the marker size.

Xe+La at 150*A* GeV/*c*

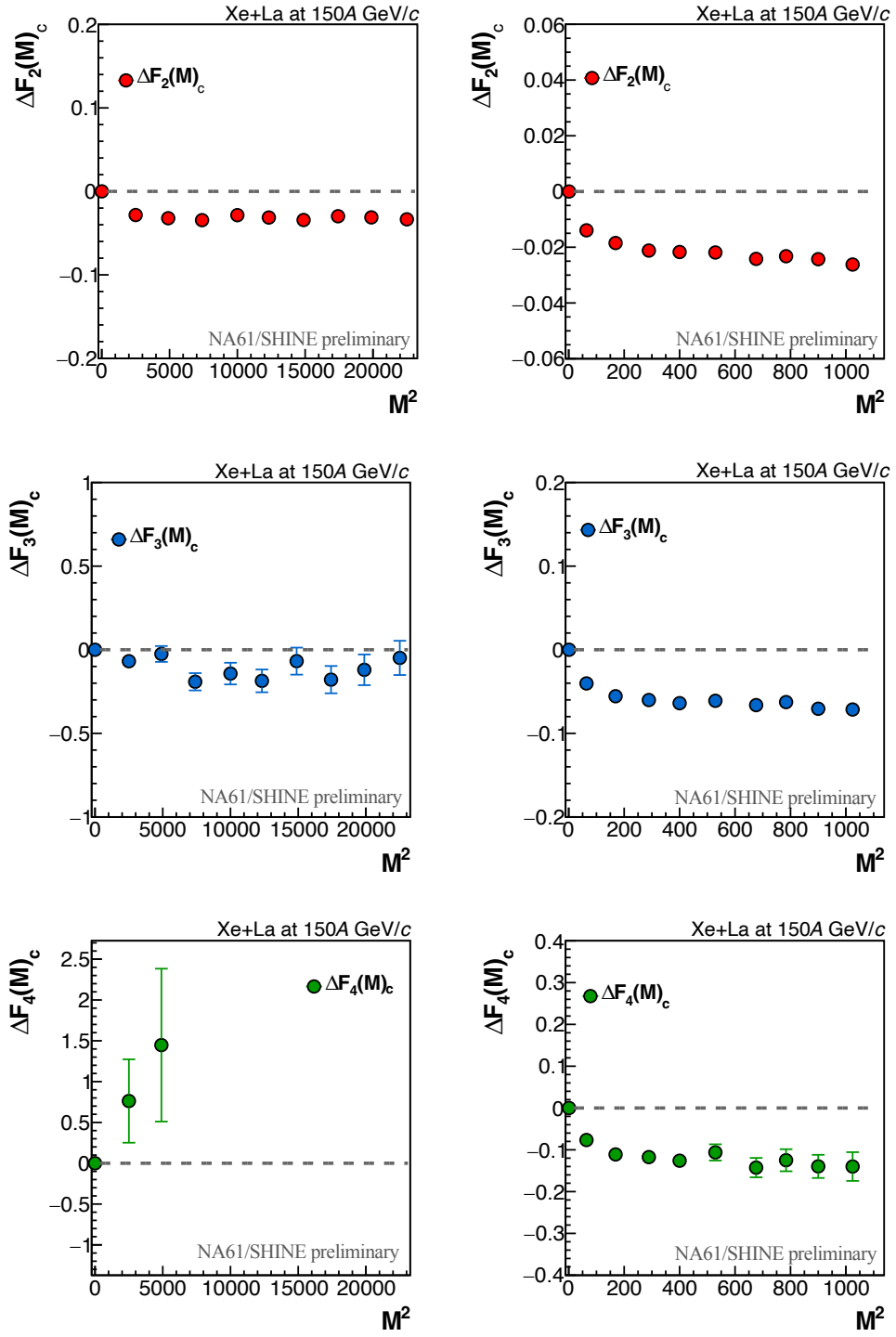

Figure 6.14: Dependence of $\Delta F_r(M)_c$ on negatively charged hadron multiplicity as a function of transverse momentum space subdivisions M^2. Only statistical uncertainties are shown; some might be smaller than the marker size. See the text for details.

6.3 Final results: Energy scan

The results on SFMs from Xe+La collisions at beam momenta of 13A–150A GeV/c have been presented. However, the central question remains unresolved. The unique opportunity provided by the NA61/SHINE experiment to explore this topic has prompted extensive discussions and rigorous testing. Two key tests, fundamental to addressing this question, are yet to be discussed.

In line with scientific methodology, it is essential to compare the experimental observations with predictions from established models or theoretical frameworks. The final chapter, preceding the conclusions, will focus on this comparison by presenting the last major test and quantifying the results against two models.

For now, the key findings obtained thus far can be summarized as follows:

- An increase in $\Delta F_r(M)$ with M^2 was observed across all Xe+La beam energies using the NA49 methodology – specifically, the p_T binning approach – along with the event and track selection criteria outlined in Sec. 2.3.2.1.
- This increase disappears after applying the cumulative transformation (see Sec. 6.2); no growth of $\Delta F_r(M)_c$ with M^2 is observed. This suggests that the presence of critical behavior can be potentially ruled out.

These observations set the stage for the final chapter, where the experimental results will be compared with expectations using two representative models, aiming to provide a comprehensive interpretation of the findings, and a conclusive chapter where the key ideas, and obtained results will be elocuently discuss, as well as other observations that emerged during the preparation of the presented results and dissertation (see Appendix A), these discussions were done in parallel and published in [51], [52] [1].

[1] Those discussion were inspired by the results obtained in this dissertation, but the ideas were proved using STAR collaboration data, no NA61/SHINE, and was not done for this collaboration due to time constrains.

p_T binning

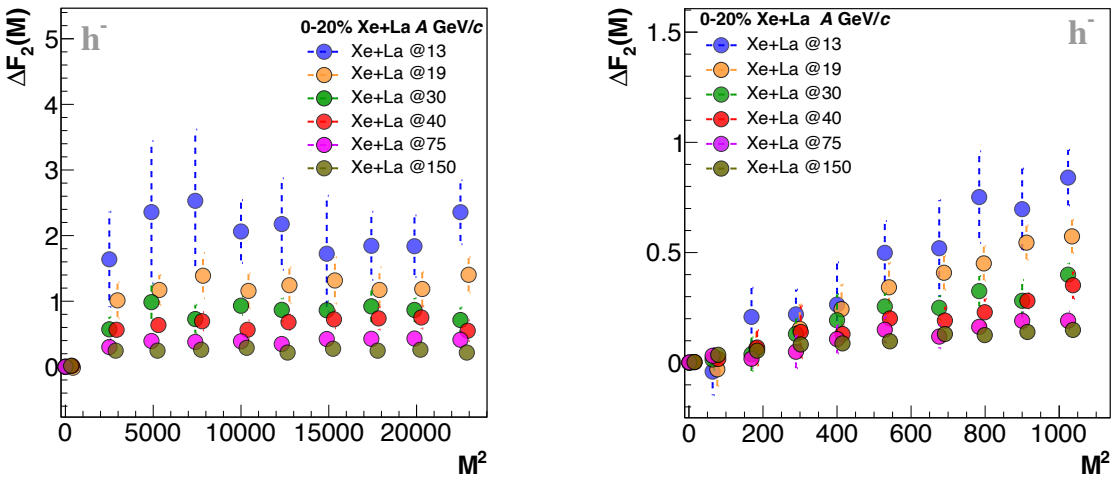

Figure 6.15: Final results on the dependence of $\Delta F_2(M)$ of negatively charged hadrons multiplicity with total error, for all the energies indicated. The large number of subdivisions in transverse momentum space is shown on the left panel, and the fine binning on the right panel.

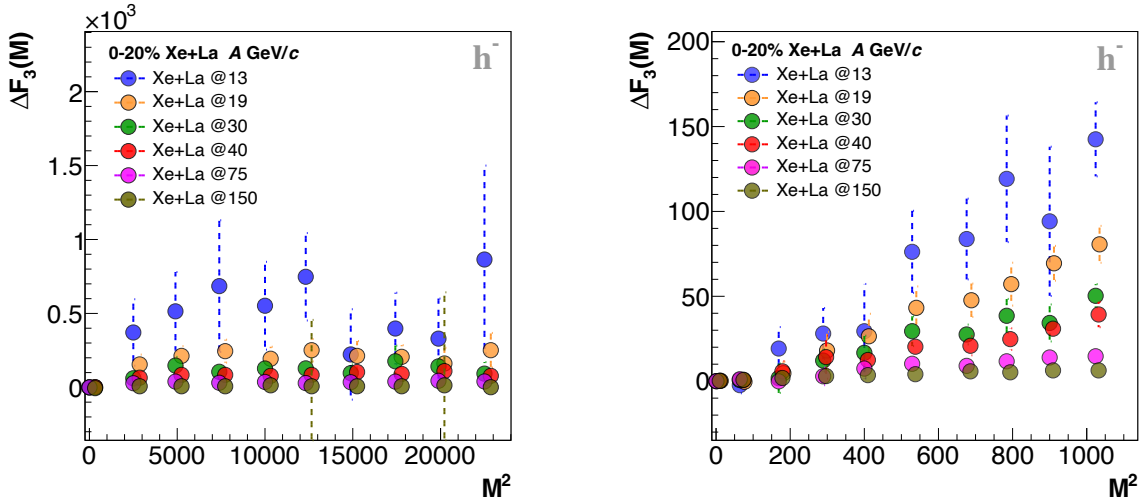

Figure 6.16: Final results on the dependence of $\Delta F_3(M)$ of negatively charged hadrons multiplicity with total error, for all the energies indicated. The large number of subdivisions in transverse momentum space is shown on the left panel, and the fine binning on the right panel.

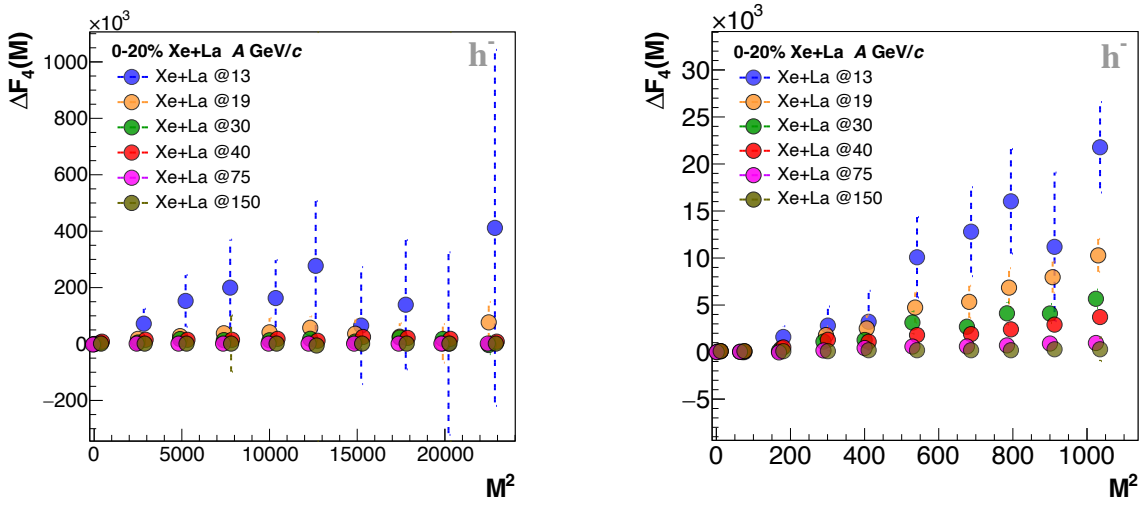

Figure 6.17: Final results on the dependence of $\Delta F_4(M)$ of negatively charged hadrons multiplicity with total error, for all the energies indicated. The large number of subdivisions in transverse momentum space is shown on the left panel, and the fine binning on the right panel.

Cumulative p_T binning

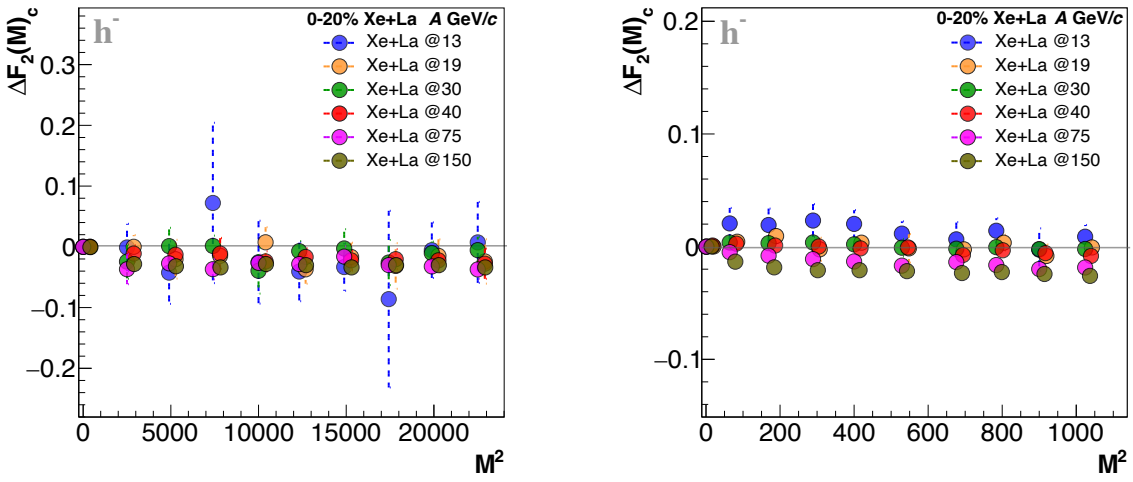

Figure 6.18: Final results on the dependence of $\Delta F_2(M)_c$ of negatively charged hadrons multiplicity with total error, for all the energies indicated. The large number of subdivisions in transverse momentum space is shown on the left panel, and the fine binning on the right panel.

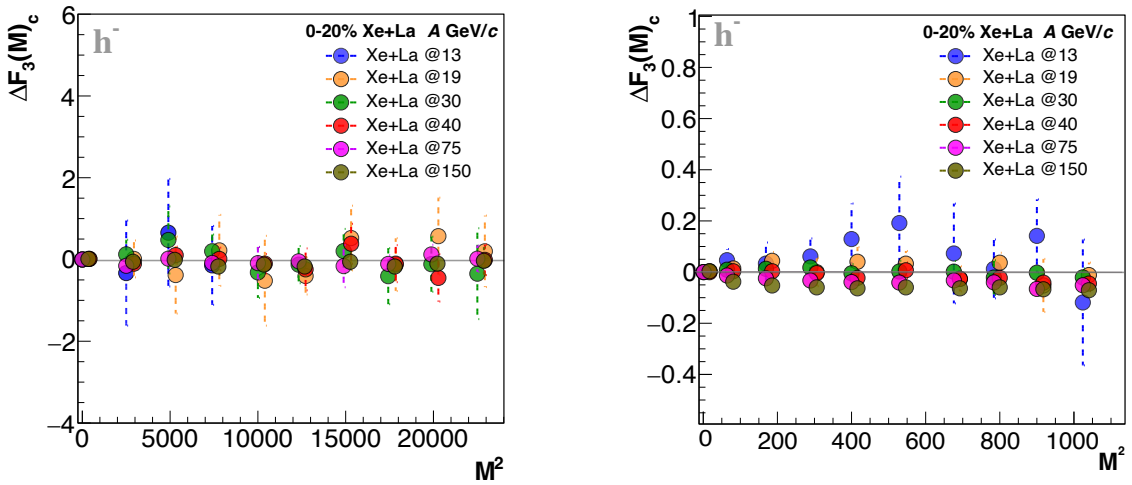

Figure 6.19: Final results on the dependence of $\Delta F_3(M)_c$ of negatively charged hadrons multiplicity with total error, for all the energies indicated. The large number of subdivisions in transverse momentum space is shown on the left panel, and the fine binning on the right panel.

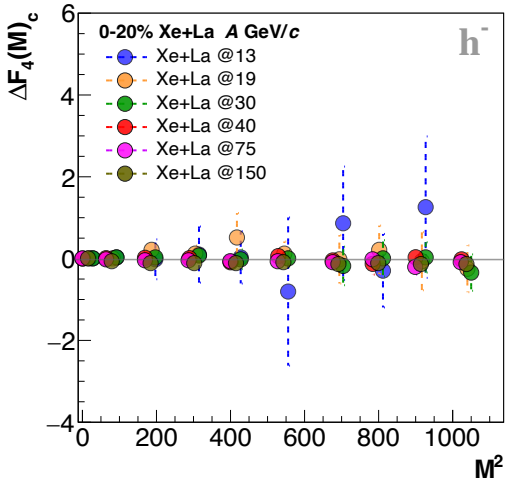

Figure 6.20: Final results on the dependence of $\Delta F_4(M)_c$ of negatively charged hadrons multiplicity with total error, for all the energies indicated. The large number of subdivisions in transverse momentum space is not shown due to the small amount of data available; fine binning is displayed.

CHAPTER 7

MODEL COMPARISON

This chapter compares the experimental results with predictions from two theoretical models. The first is a dynamical model, EPOS1.99 [75], which incorporates multiple sources of particle correlations, for example, resonance decays, and jet-like structures. The second is the Power-law Model [28], designed to simulate particle pairs with correlations in transverse momentum following a power-law distribution, combined with a component of uncorrelated particles (see Sec. 2.2). The following results compare the Xe+La data set at 0-20% centrality at 150A GeV/c beam momenta discussed in Chapter 5.

It is important to clarify that both comparisons are substantially different from each other. The comparison with EPOS will confirm or deny the final remarks of the previous chapter. The comparison with the Power-law Model will help understand the data dynamics in the presence of power-law behavior.

7.1 Comparison with EPOS 1.99

To ensure consistency with the experimental conditions, both models are subjected to a full detector simulation and reconstruction chain. The simulated particles are passed through the NA61/SHINE framework (see Sec. 3.3), which models particle transport, decay, and secondary interactions within the detector geometry. In this section, a comparison of the mentioned simulated productions discussed will be presented:

- **EPOS (pure)** A set of simulated events directly from the EPOS1.99 generator, including information on particle momenta, mass, charge, and origin.

- **EPOS with detector effects** The same generated events are processed through the full simulation and reconstruction chain.

Usually, a detailed comparison between model and data is essential to determine whether observed scaling behaviors, such as the power-law increase in SFMs, can arise from conventional particle production mechanisms or point to underlying critical phenomena. In our case, we will use this to better understand the physics related to our analysis from a theoretically modeled point of view.

In Figs. 7.1 and 7.2 we can see the previously shown results of SFMs in p_T binning and cumulative p_T binning , $\Delta F_r(M)$ vs M^2 and $F_r(M)_c$ vs M^2 of Xe+La 150A GeV/c interactions (see Fig. 6.8 and Fig. 6.14), alongside its simulated counterparts EPOS (pure) and EPOS with detector effects. In the left panels, the results for full M^2 binning, and on the right panels, the maximized version for short M^2 binning.

In Fig. 7.1, the $\Delta F_r(M)$ versus M^2 results for p_T binning are displayed. It can be observed that neither EPOS (pure) nor EPOS with detector effects exhibits the increasing trend with M^2 seen in the Xe+La data. This holds consistently for all orders $r = 2, 3, 4$, with the corresponding values remaining close to the dashed line at zero. It is well established that the EPOS model does not include short-range correlations of the Bose-Einstein type [75], which supports the interpretation that such correlations are necessary to produce the observed increase. Moreover, the agreement between EPOS (pure) and EPOS with detector effects confirms that the applied track selection criteria (see Sec. 5.1.2) effectively remove possible detector-induced correlations, if present, thus isolating any remaining contributions to genuine physical effects. Additionally, the results from the correlation function Δp_T, displayed in Fig. 7.3, also point out the existence of a correlation in data, but not present in EPOS, supporting the idea of the presence of short-range correlations in this data set.

After applying the cumulative transformation to the simulated results, a good agreement is observed between the data and both EPOS simulations, as shown in Fig. 7.2 $\Delta F_r(M)c$ versus M^2. Apart from the anticorrelations introduced by the mTTD cut (see Sec. 4.3), no visible increase remains, indicating that unwanted correlations, whether from detector effects or physical processes, have been effectively removed.

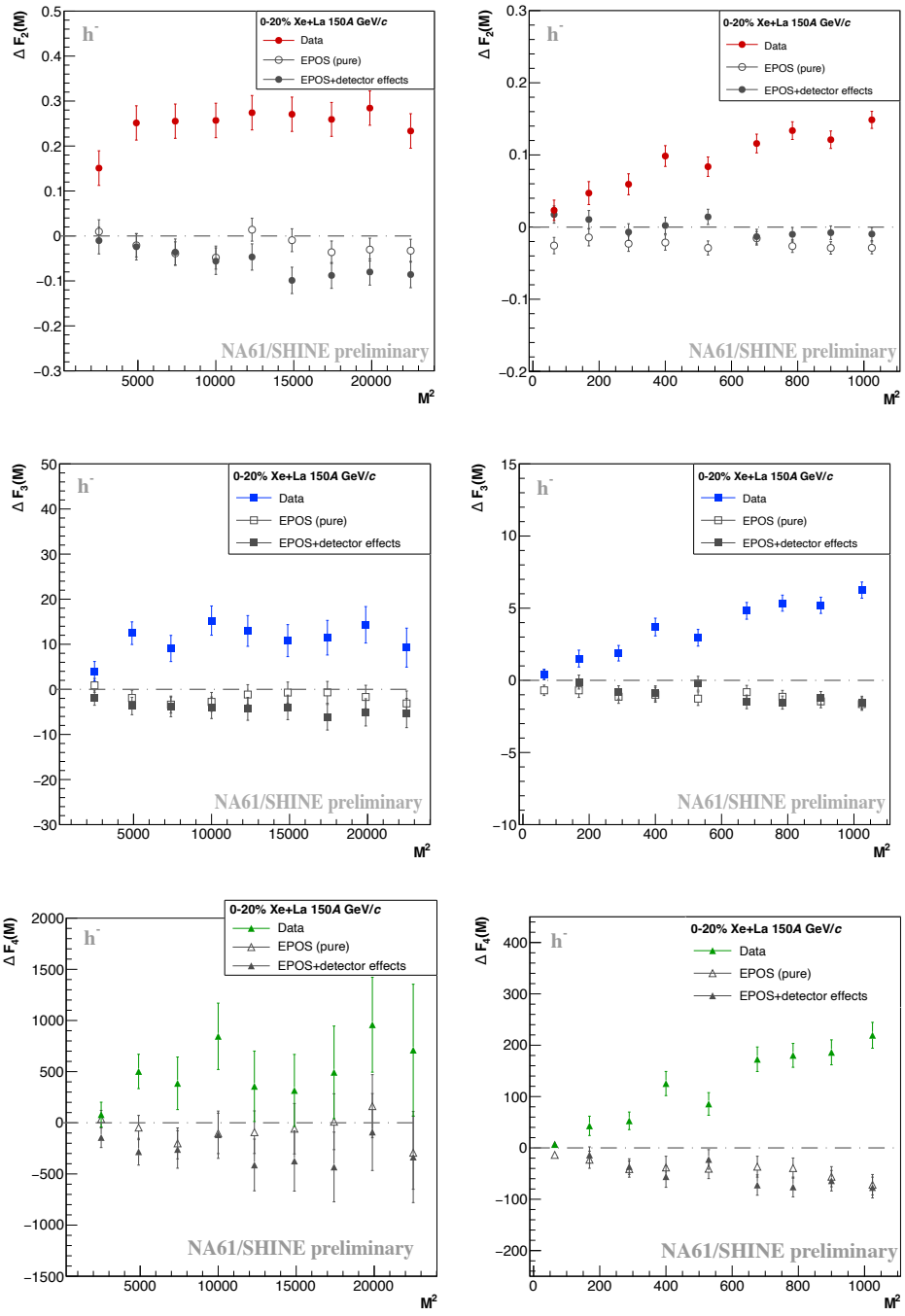

Figure 7.1: Comparison of $\Delta F_r(M)$ versus M^2 for Xe+La interactions at 150A GeV/c, shown alongside simulations from EPOS (pure) and EPOS with detector effects. Left panels display results with full M^2 binning, while right panels show results with optimized short M^2 binning. Color code is: red for $\Delta F_2(M)$, blue for $\Delta F_3(M)$, and green for $\Delta F_4(M)$ from the experimental data; simulated results from EPOS with detector effects are shown as gray filled markers, and EPOS (pure) results as empty markers.

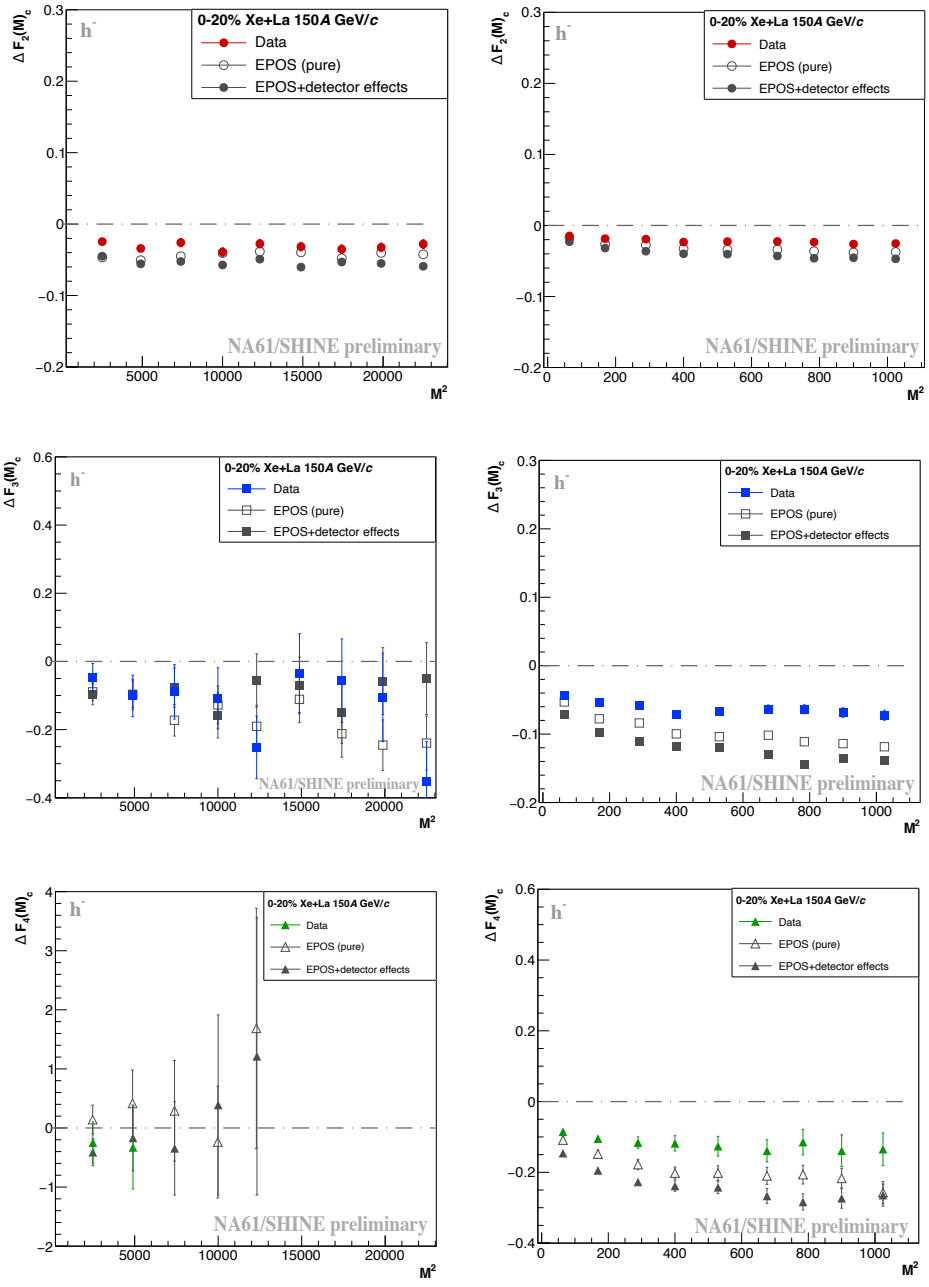

Figure 7.2: Comparison of $\Delta F_r(M)$ versus M^2 for Xe+La interactions at 150A GeV/c, shown alongside simulations from EPOS (pure) and EPOS with detector effects. Left panels display results with full M^2 binning, while right panels show results with optimized short M^2 binning. Color code is: red for $\Delta F_2(M)$, blue for $\Delta F_3(M)$, and green for $\Delta F_4(M)$ from the experimental data; simulated results from EPOS with detector effects are shown as gray filled markers, and EPOS (pure) results as empty markers.

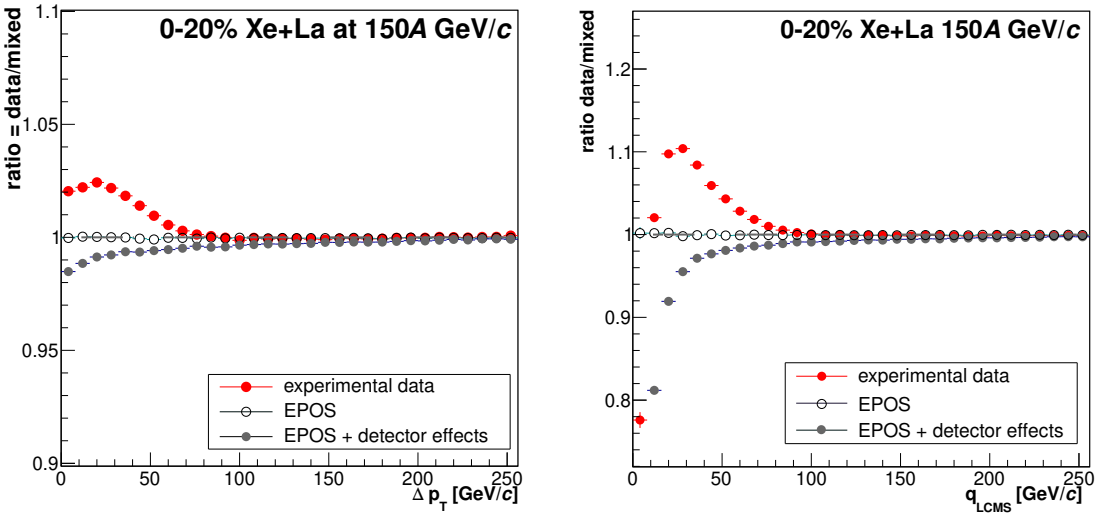

Figure 7.3: Correlation functions obtained for experimental data, EPOS and EPOS RECONSTRUCTED .

7.2 Comparison with Power-law Model

As motivation, the Power-law Model [28] uses power-law correlations between particles near the critical point to generate momentum correlated and uncorrelated particles. It was introduced in Sec. 2.2.

A feature of the Power-law Model is that we can configure it to produce correlated pairs of particles, given the parameters obtained in Xe+La 150A GeV/c analysis. Then we can embed these pairs into the data (by replacing a percentage of the original particles with correlated ones) and check what it will look like. The results obtained for p_T binning, $\Delta F_2(M)$ vs M^2 are shown in Fig. 7.4 and results obtained for cumulative p_T binning, $\Delta F_2(M)_c$ vs M^2 are shown in Fig. 7.5.

This brief study differs from the main analysis and the comparison with EPOS in its objective: it aims to introduce particles that are intrinsically correlated, as produced by the model, into the real data at varying percentages. The goal is to distinguish between signals from short-range correlations and those of a power-law nature. Two embedding scenarios were analyzed and compared to the previously discussed Xe+La results at 150A GeV/c. In Case 1, 25% of the particles were embedded into the Xe+La data, while in Case 2, 80% of the particles were embedded.

The steps for embedding and calculations on SFMs in this comparison are the following:

- Power-law generated correlated pairs based on the multiplicity distribution obtained for this data set.

- We replace 25% and 80% of the original particles with particles of the power-law from the set without acceptance map and mTTD.
- We repeat the analysis procedure: create a mixed data set from the embedded data set, and apply mTTD. (Correlated pairs are not acceptance map proof.)
- We recalculate SFMs' results for non-cumulative and cumulative binning.

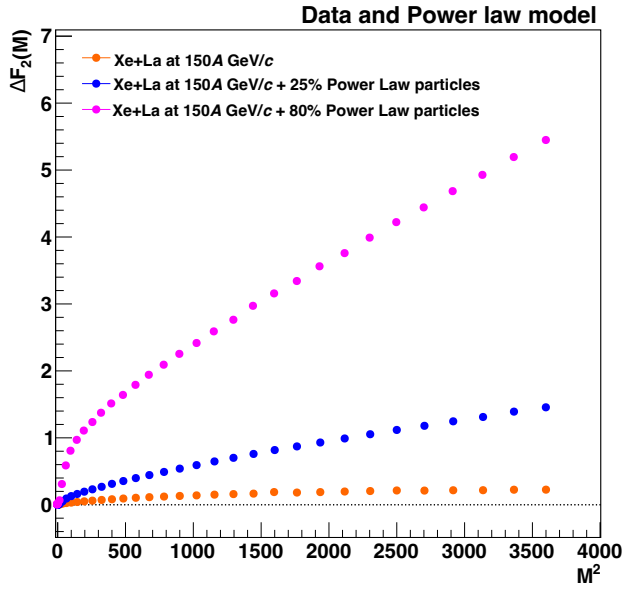

Figure 7.4: Comparison of two embedding scenarios with the original Xe+La results at 150A GeV/c (shown in orange) for $\Delta F_2(M)$ vs M^2. In Case 1 (blue), 25% of model-generated correlated particles were embedded into the Xe+La data, while in Case 2 (magenta), 80% were embedded.

The results obtained for p_T binning, $\Delta F_2(M)$ vs M^2, support the original statement about cumulative transformation see Sec. 6.2 shown in Fig. 7.5. A strong signal very different from the original Xe+La data set is observed in both cases, and this power-law increase remains present after the cumulative transformation is applied.

Additionally, another plot was made to measure the impact of power-law correlated particles within the short-range correlations frame. Fig. 7.6 shows the correlation function of Δp_T for the discussed cases.

Fig. 7.6 shows that a power-law-like correlated particle, if it exists within the dataset, will produce a highly different Δp_T correlation function compared to the data. Plot in color orange represents the results seen in the previous chapter for Xe+La 150A GeV/c, where a hill was reported within the Δp_T range between 0 to 100 MeV. Whereas the results obtained after embedding the power-

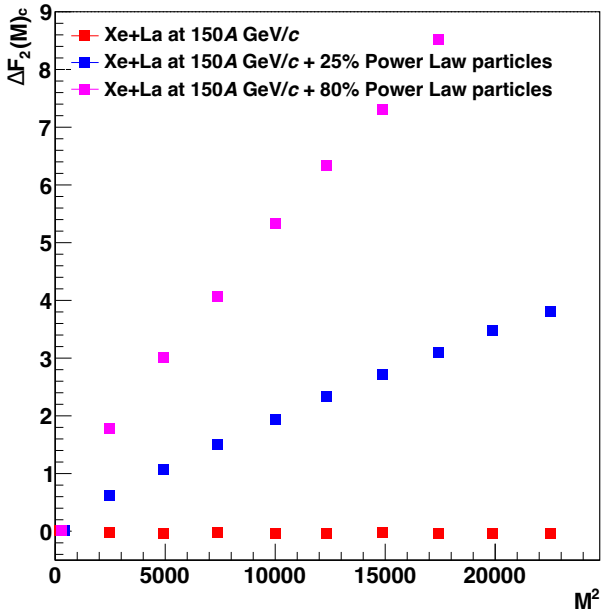

Figure 7.5: Comparison of two embedding scenarios with the original Xe+La results at 150A GeV/c (shown in orange) for $\Delta F_2(M)_c$ vs M^2. In Case 1 (blue), 25% of model-generated correlated particles were embedded into the Xe+La data, while in Case 2 (magenta), 80% were embedded.

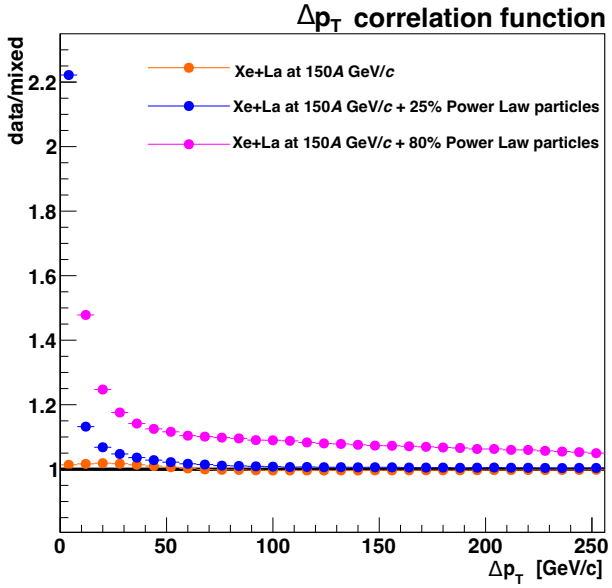

Figure 7.6: Comparison of two embedding scenarios with the original Xe+La results at 150A GeV/c (shown in orange) for Δp_T correlation function. In Case 1 (blue), 25% of model-generated correlated particles were embedded into the Xe+La data, while in Case 2 (magenta), 80% were embedded.

law particles have a completely different shape in the correlation function, rather than a peak in the smaller bins that decreases quickly with higher values of Δp_T.

This chapter has provided two complementary analyses that reinforce and clarify the findings presented earlier:

- A comparison with EPOS simulations – both in their pure Monte Carlo form and including detector effects – demonstrates that the analysis procedure effectively removes detector-induced correlations. As a result, the observed increase in $\Delta F_2(M)$ reported in Chapter 5.1.5 can be attributed only to genuine short-range correlations, such as those of HBT type.
- An embedding study, introducing power-law-like particles at two different fractions into the original Xe+La dataset at 150A GeV/c, showed that the resulting fluctuation patterns differ distinctly from those induced by short-range correlations. This confirms that the observed signal in the data is not a product of power-law behavior.

These findings pave the way for the conclusions, building upon the observations from Chapter 5.1.5 and the discussions throughout this chapter. The next and final chapter will synthesize these insights and revisit the broader context introduced in Chapter 2.

CHAPTER 8

SUMMARY AND CONCLUSIONS

This dissertation reports on the analysis of negatively charged hadrons on Scaled Factorial Moments in strong interacting matter in 0–20% central Xe+La collisions at 13A, 19A, 30A, 40A, 75A and 150A GeV/c recorded by the NA61/SHINE experiment at the CERN SPS.

The work included a brief review of the intermittency results obtained by previous collaborations and the discussions sparked by them, methodology in NA61/SHINE, results, and comparison with models. In brief:

- A review of intermittency analysis in high-energy physics in different experiments to study strongly interacting matter was discussed in Chapter 2.
- The NA61/SHINE approach to SFMs analysis to study the phase diagram of strongly interacting matter and possible existence of the critical point, using cumulative variables and statistically independent data points, was discussed in Chapter 3.
- The NA61/SHINE experimental facility and strong interaction program were discussed in Chapter 4.
- The event and track selection were discussed in detail in Chapter 5.
- Results on SFMs of negatively charged hadrons in transverse momentum space and cumulative transverse momentum space were presented in Chapter 6. Possible biases in the experimental results were estimated using the EPOS 1.99 model and the Power-law model, and studied in Chapter 7 to understand misleading signals due to physical effects.

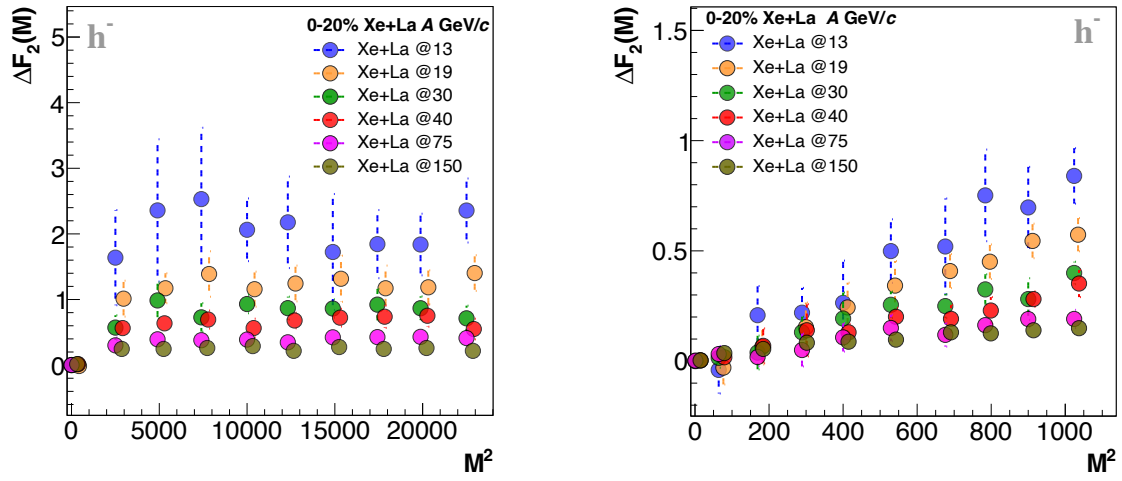

Figure 8.1: Final results on the dependence of $\Delta F_2(M)$ of negatively charged hadrons multiplicity with total error, for all the energies studied in this dissertation in Xe+La collisions with NA61/SHINE for transverse momentum binning.

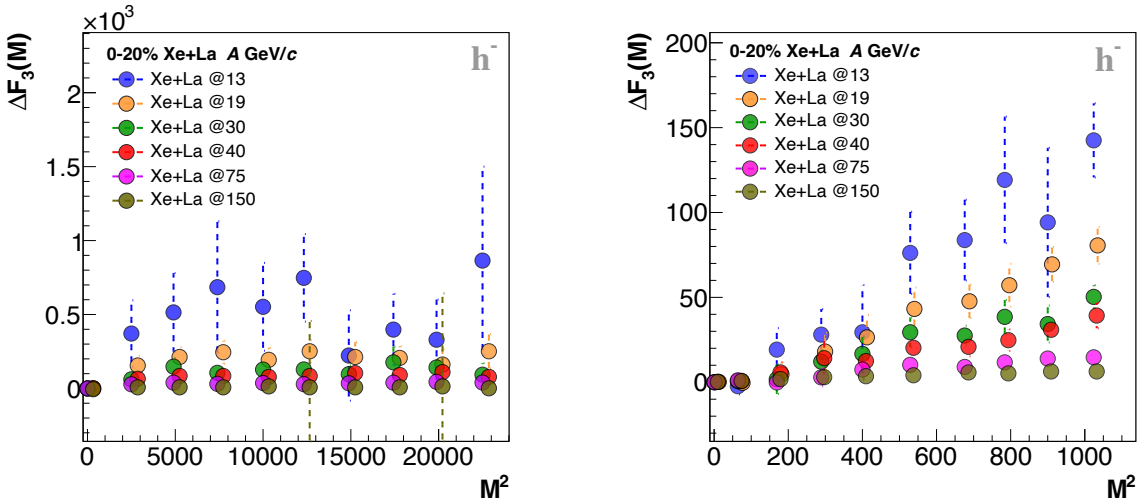

Figure 8.2: Final results on the dependence of $\Delta F_3(M)$ of negatively charged hadrons multiplicity with total error, for all the energies studied in this dissertation in Xe+La collisions with NA61/SHINE for transverse momentum binning.

The key physics result of the thesis is the absence of any indication of a power-law correlation in the 0–20% central Xe+La collisions. The presence of short-range correlations of the HBT type could explain the misleading signals reported in p_T binning. This increase in $\Delta F_r(M)$ was reported by another collaboration in a close collision energy range. A summary of these results can be found in Figs. 8.1, 8.2 and 8.3.

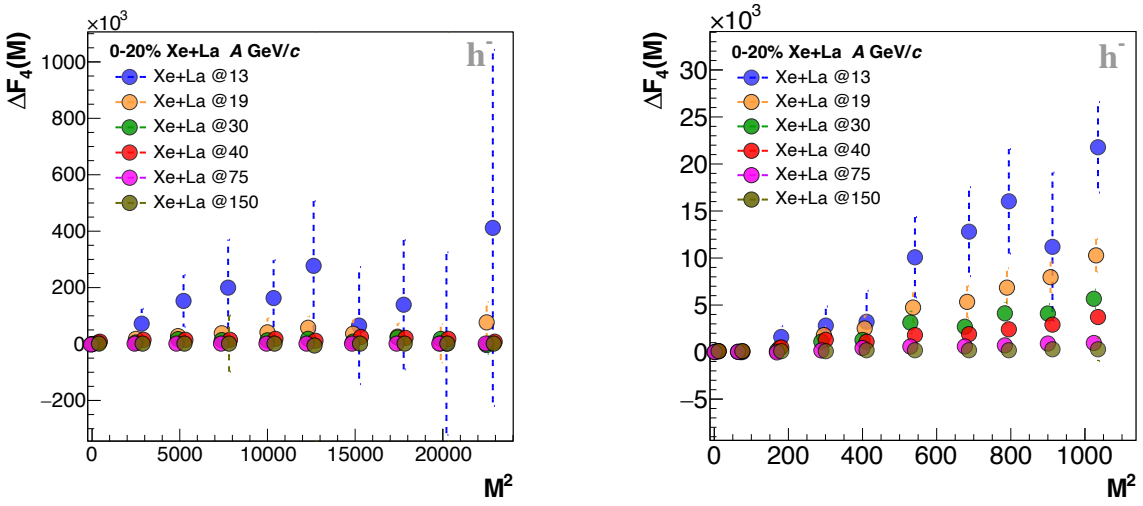

Figure 8.3: Final results on the dependence of $\Delta F_4(M)$ of negatively charged hadrons multiplicity with total error, for all the energies studied in this dissertation in Xe+La collisions with NA61/SHINE for transverse momentum binning.

In contrast, the results in cumulative transverse momentum don't exhibit any increase. This premise concludes that there is no indication of a power-law increase with cell size. Since cumulative transformation preserves the scale-invariant power-law correlations but destroys other types of non-scale-invariant correlations, the presented results in the non-cumulative momentum phase might not be an indication of critical behaviour in strongly interacting matter. A summary of these results can be found in Figs. 8.4, 8.5 and 8.6.

Although the results obtained by studying negatively charged hadrons were not predicted initially to present signals of the critical point, a comprehensive study of the SFMs in this direction was needed to further understand the behavior of particles from an experimental point of view using SFMs and a wider comprehension of the tool used.

Furthermore, a discussion not included in the main part of this dissertation was sparked, as mentioned at the end of Chapter 6; so far, short-range correlations were presented as the main responsible factor for misleading signals of a power-law, which is consistent with findings from the literature review in Chapter 2. However, other sources might also contribute to this effect.

Due to time constraints, these additional sources were not discussed within the scope of this thesis. Nonetheless, a discussion based on Monte Carlo models and STAR data was presented in [52] and expanded in [51].

The first publication [52] raised questions about the shape of the multiplicity distribution in each subdivided cell and its apparent Poisson distribution. Evidence supporting this can be found in

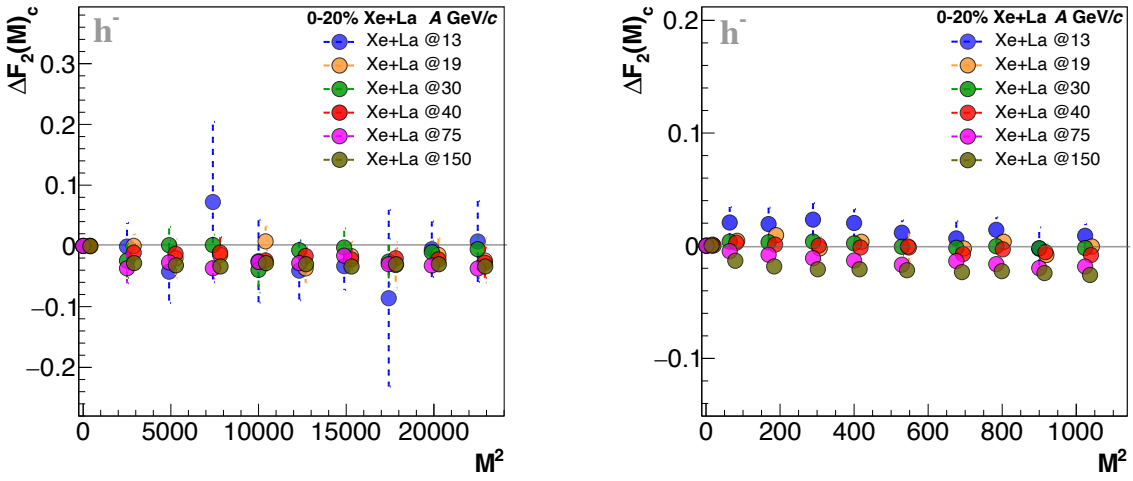

Figure 8.4: Final results on the dependence of $\Delta F_4(M)_c$ of negatively charged hadrons multiplicity with total error, for all the energies studied in this dissertation in Xe+La collisions with NA61/SHINE.

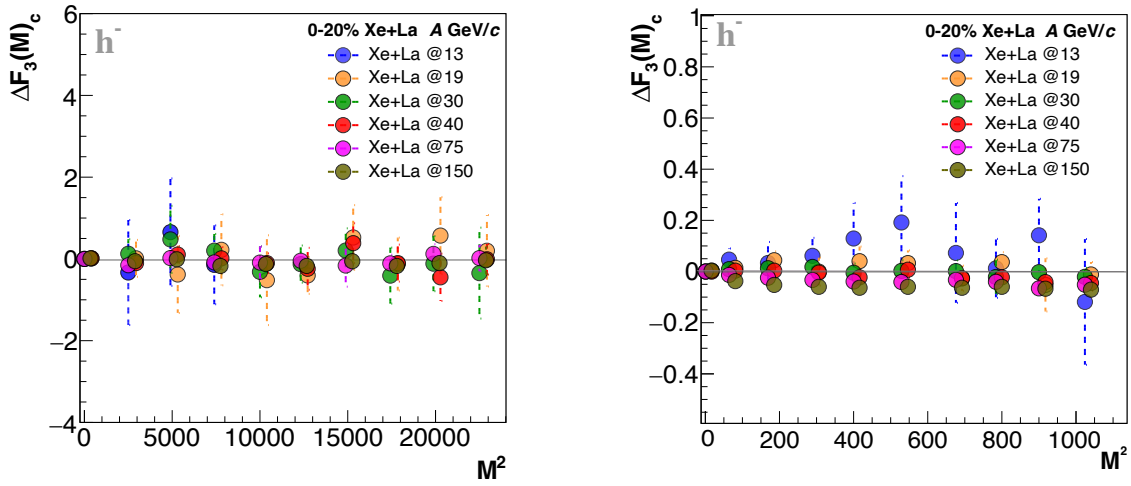

Figure 8.5: Final results on the dependence of $\Delta F_4(M)_c$ of negatively charged hadrons multiplicity with total error, for all the energies studied in this dissertation in Xe+La collisions with NA61/SHINE.

Appendix A. Additionally, from reported observations of charged particle density fluctuations in central Au+Au collisions at RHIC/STAR, the authors propose that analyzing factorial moments in relativistic heavy-ion collisions is a viable method to investigate density fluctuations linked to correlation phenomena, including new particle production mechanisms such as multiparticle bunching.

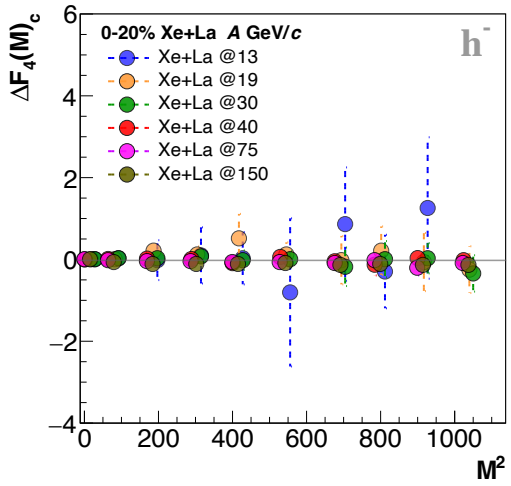

Figure 8.6: Final results on the dependence of $\Delta F_4(M)_c$ of negatively charged hadrons multiplicity with total error, for all the energies studied in this dissertation in Xe+La collisions with NA61/SHINE. The large number of subdivisions in transverse momentum space is not shown due to the small amount of data available; fine binning is displayed.

Furthermore, in the second publication, the authors emphasized that a power law is not necessarily an exclusive signal of critical behavior. As reviewed in Chapter 2 of this dissertation, several studies suggest that a scaling relation between higher-order factorial moments of hadron multiplicity distributions and the second factorial moment may serve as a diagnostic tool for identifying the QCD critical point.

However, the publication [51] demonstrates that the observed scaling behavior may not be exclusive to critical phenomena, but could instead result from the phase-space cell-partitioning procedure used in the analysis.

Whether the critical point exists – or whether its potential location could be revealed by a combination of tools – remains an open question. It is also possible that theoretical predictions are still a puzzle to solve, as predictions for the location of the critical point vary widely depending on the model employed.

Based on the results obtained in this dissertation, it is not possible to confirm or deny the existence of the critical point. However, the conclusions suggest the presence of multiple correlations in particle physics that have not yet been fully considered or quantified in the study of the QCD phase diagram. These correlations could yield intriguing results that call for more refined tools and computational methods.

The search for the critical point of strongly interacting matter in the NA61/SHINE is coming

to an end, since the strong interactions program has switched to the mentioned open charm topic, however other future experiments might be able to study more directions using SFMs to study the phase diagram of strongly interacting matter, the crossover region and the existing theoretical predictions of the critical point.

APPENDIX A

KINEMATIC VARIABLES

NA61/SHINE coordinate system

Chapter 3, provides an overview of the NA61/SHINE detector and its coordinates. The system's origin is located at the beamline's center in the VTX-2 magnet. The system is right-handed, with the z axis coinciding with the beamline axis. The y axis is vertical and parallel to the electron drift velocity in TPCs, while the x axis is horizontal.
The azimuthal angle is defined as:

$$\phi = \arctan \frac{p_y}{p_x} \,. \tag{A.1}$$

The polar angle, denoted by $\theta = \arcsin \frac{p_T}{p}$, measures the angle between a particle's direction and the z axis. When $\theta = 0$, the particle moves parallel to the beamline. The θ range between 0 and 2π.

Total momentum and transverse momentum variables

The total momentum length is defined as the square root of the momentum components in the coordinate system described, added in quadrature:

$$p = \sqrt{p_x^2 + p_y^2 + p_z^2} \,. \tag{A.2}$$

The z axis is considered parallel to the beamline, which means that the transverse variables are determined by their x and y components.The transverse momentum length is:

$$p_T = \sqrt{p_x^2 + p_y^2} \,. \tag{A.3}$$

Two-particle transverse momentum difference

The two-particle transverse momentum difference, Δp_T is defined as:

$$\Delta p_T = \sqrt{(p_{x_1} - p_{x_2})^2 + (p_{y_1} - p_{y_2})^2} \ , \tag{A.4}$$

where p_{x_1}, p_{x_2}, p_{y_1}, p_{y_2} are x and y components of the transverse momentum of particle 1 and 2, respectively.

Collision energy

The Lorentz-invariant Mandelstam variable describes the energy available in the center of mass:

$$\sqrt{s} = \sqrt{(E_{\text{beam}} + E_{\text{target}})^2 - (p_{\text{beam}} + p_{\text{target}})^2 c^2} \ . \tag{A.5}$$

Typically, the energy per pair of nucleons at the center of mass is represented as $\sqrt{s_{NN}}$, where m_{beam}, m_{target}, and m_N all have the same value. In experiments using a fixed target, p_{target} equals zero, and E_{target} equals the mass of the ion utilized as the target.

$$\sqrt{s_{NN}} = \sqrt{(E_{\text{beam}} + m_N)^2 - p_{\text{beam}}^2 c^2} \ . \tag{A.6}$$

Rapidity

Rapidity is a measure of velocity in the realm of relativity due to its properties under the Lorentz transformation. When multiple Lorentz boosts are performed in the same direction, they can be represented by a single boost. The transformation of velocity is given by:

$$\beta'' = |v/c|'' = \frac{\beta + \beta'}{1 + \beta\beta'} \ , \tag{A.7}$$

The velocity transformation is a non-linear. To address this issue, we use "rapidity" which is defined as $\beta = \tanh y$ or $y = \frac{1}{2}\frac{1+\beta}{1-\beta}$. The rapidity is linear, $y'' = y + y'$ when undergoing a longitudinal Lorentz boost.

Alternatively one expresses particle's rapidity by its energy (E) and momentum component (p_z) parallel to the transformation direction:

$$y = \frac{1}{2} \ln \frac{E + p_z c}{E - p_z c} \ . \tag{A.8}$$

Inversely one can get:

$$E = m_T \cosh y, \ p_z = m_T \sinh y \ , \tag{A.9}$$

where $m_T = \sqrt{m^2 + p_T^2}$. And using the mass of a pion for the calculations presented in this thesis.

Rapidity can be easily transformed from the laboratory to the center of mass (CMS) frame:

(A.10) $$y_{\text{CMS, frame}} = y_{\text{LAB, frame}} + y_{\text{CMS}} \ ,$$

where y_{CMS} is defined as:

(A.11) $$y_{\text{CMS}} = \arctan \frac{p_{\text{beam}} c}{E_{\text{beam}} + m} \ ,$$

p_{beam} is the beam momentum, $E_{\text{beam}} = \sqrt{p_{\text{beam}}^2 c^2 + m_N^2}$ is the beam energy with m as the mass of a pion. In this thesis, rapidity is given in the center-of-mass frame.

In this thesis, the term "mid-rapidity" refers to a region in the y-axis that is close to y=0, specifically between y=0 and y=0.75. This refers to particles that are approximately perpendicular to the beamline direction in the center of the mass system. The areas above $y = 0$ and below $y = 0$ are commonly known as the *forward* and *backward* rapidity regions, respectively.

APPENDIX B

MULTIPLICITY DISTRIBUTIONS PER CELL

With a keen understanding of intermittency that can emerge from the discussion in Chapter 2, one might ask about the multiplicity distributions of each cell.

Intermittency divides cells and counts the number of pairs, triplets, or quadruplets. It then divides the 2D phase space into subcells, counts again, and repeats the process. One can do an average distribution of the particles for each subdivided cell, or one might try to think about how the multiplicity distributions change while doing these divisions. Are these distributions Poissonian?

If we consider this, a significant problem arises at the end of the subdivision. The number of cells is $M^2 = 24000$; therefore, examining each multiplicity distribution is a very difficult task, which is one of the reasons why people have studied scaled factorial moments. There are questions unanswered in this matter.

First, let's check some example multiplicity distributions following this idea. In the following plots, I will present the multiplicity distribution of one cell with a corresponding Poissonian distribution; this will be the Poisson distribution obtained given the mean calculated from the original distribution. Next to it is the 2D cell of $p_x - py$ phase space.

Results obtained indicated that the multiplicity distributions are indeed Poisson-like, but the sources of these density fluctuations can be from different origins than the ones discussed in this dissertation.

Multiparticle bunching Intermittency states that the density fluctuations in the subdivided cells lead to the power-law-like behavior of SFMs, and it is said that this is a potential sign of

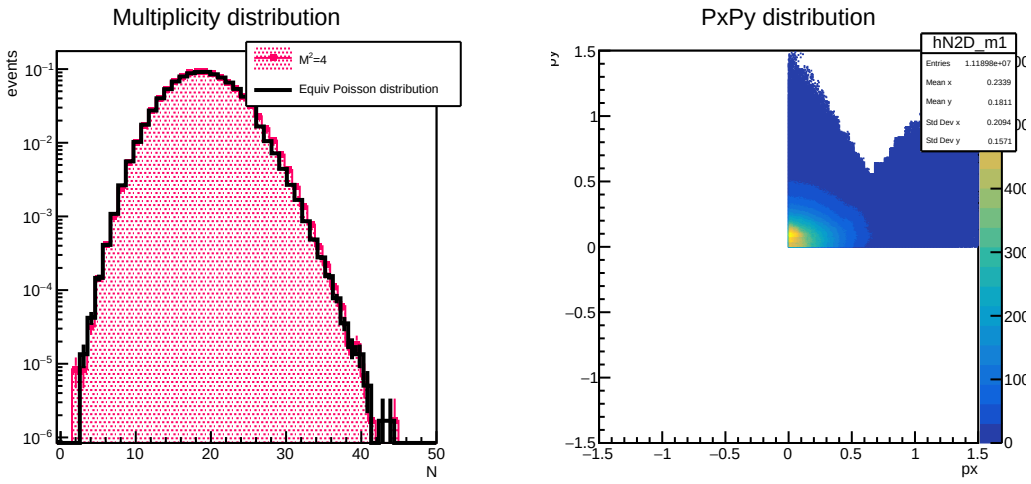

Figure B.1: Example Multiplicity distribution for cell when $M^2 = 4$ with a Poisson fit(right). Example of the 2D $p_x - p_y$ distribution of the same cell for illustration (left).

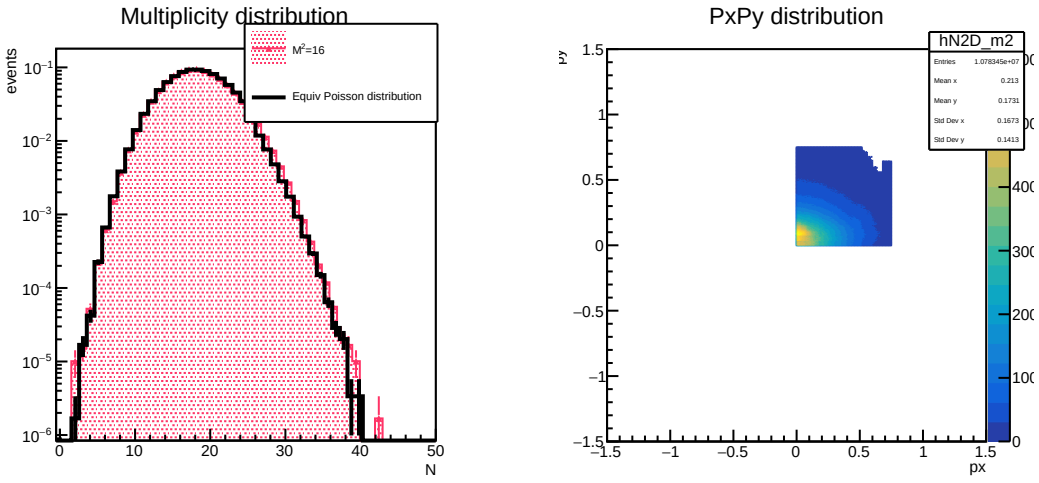

Figure B.2: Example Multiplicity distribution for cell when $M^2 = 16$ with a Poisson fit(right). Example of the 2D $p_x - p_y$ distribution of the same cell for illustration (left).

the critical point. But, a correlated bunch of particles that appear only in one cell can also be responsible for an "intermittent-like" behavior of $\Delta F_r(M)$. Further discussion can be found in [52].

Furthermore, it is possible to demonstrate that the observed increase or the power-law behavior on $\Delta F_r(M)$ of scaled factorial moments is not exclusive of critical phenomena [51]. Not only can particle bunching or HBT correlations be responsible. But to determine whether this simplified scenario can account for the broad range of experimental observations, further studies are needed.

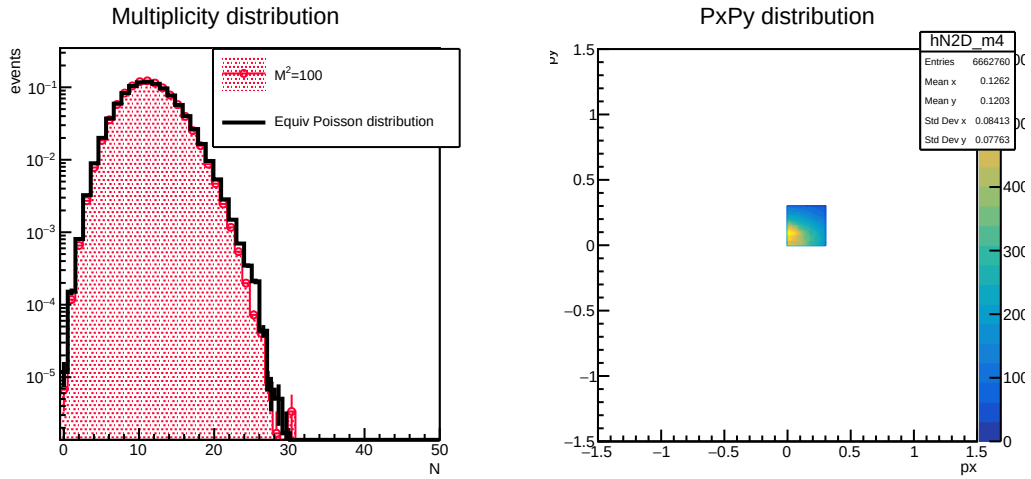

Figure B.3: Example Multiplicity distribution for cell when $M^2 = 100$ with a Poisson fit(right). Example of the 2D $p_x - p_y$ distribution of the same cell for illustration (left).

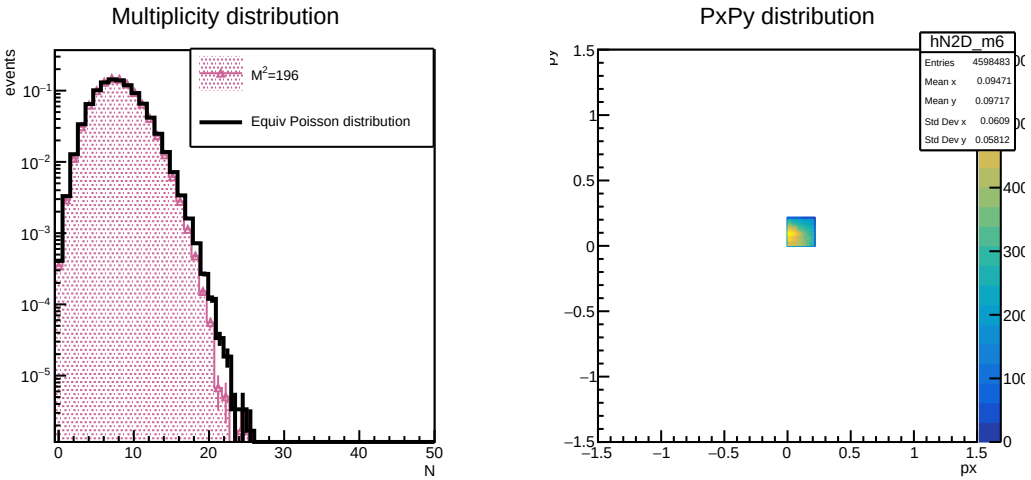

Figure B.4: Example Multiplicity distribution for cell when $M^2 = 196$ with a Poisson fit(right). Example of the 2D $p_x - p_y$ distribution of the same cell for illustration (left).

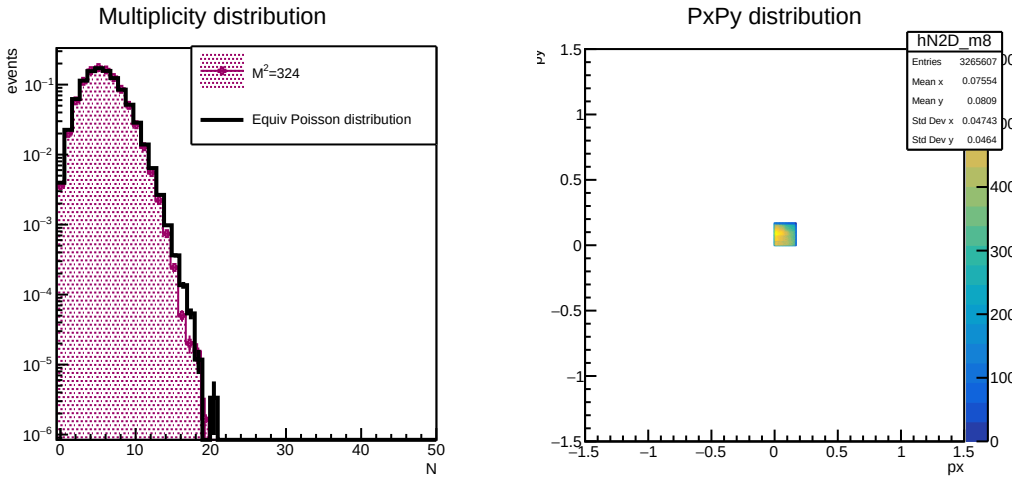

Figure B.5: Example Multiplicity distribution for cell when $M^2 = 324$ with a Poisson fit(right). Example of the 2D $p_x - p_y$ distribution of the same cell for illustration (left).

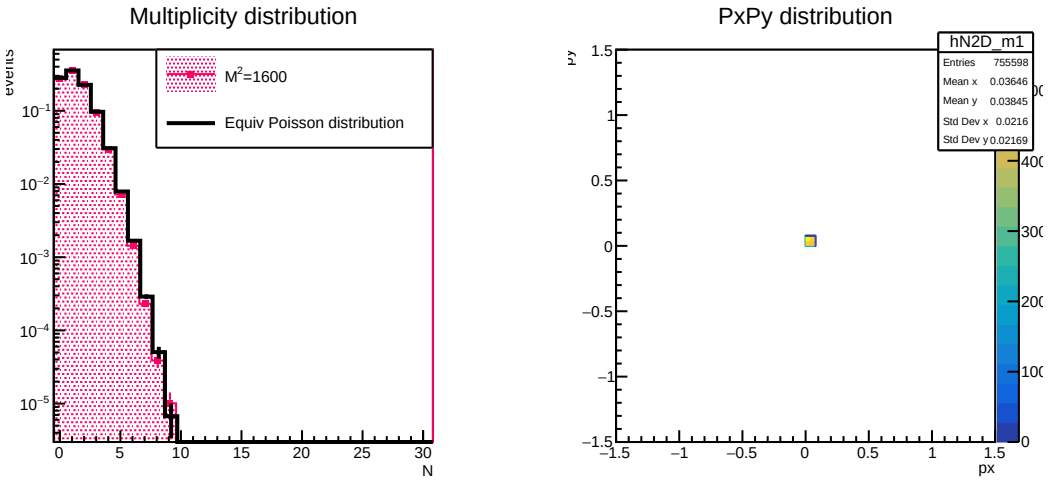

Figure B.6: Example Multiplicity distribution for cell when $M^2 = 1600$ with a Poisson fit(right). Example of the 2D $p_x - p_y$ distribution of the same cell for illustration (left).

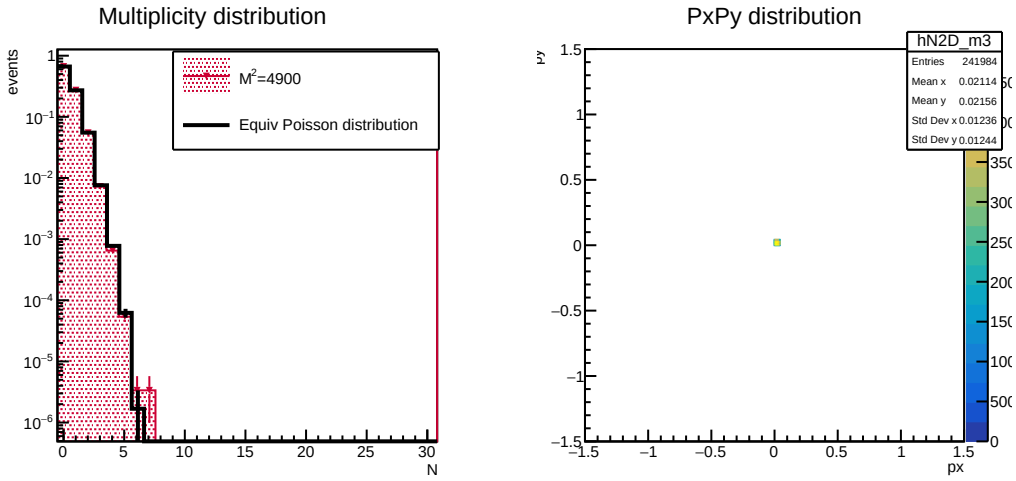

Figure B.7: Example Multiplicity distribution for cell when $M^2 = 4900$ with a Poisson fit(right). Example of the 2D $p_x - p_y$ distribution of the same cell for illustration (left).

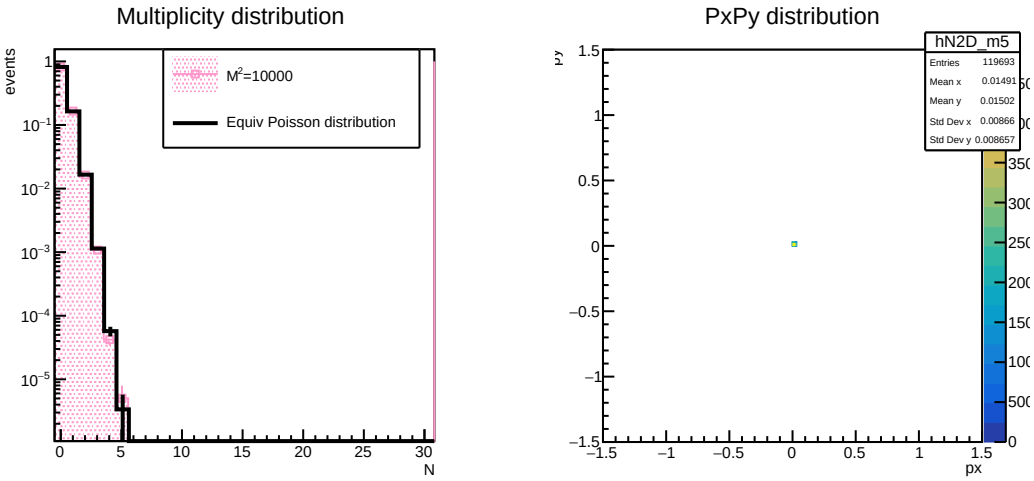

Figure B.8: Example Multiplicity distribution for cell when $M^2 = 10000$ with a Poisson fit(right). Example of the 2D $p_x - p_y$ distribution of the same cell for illustration (left).

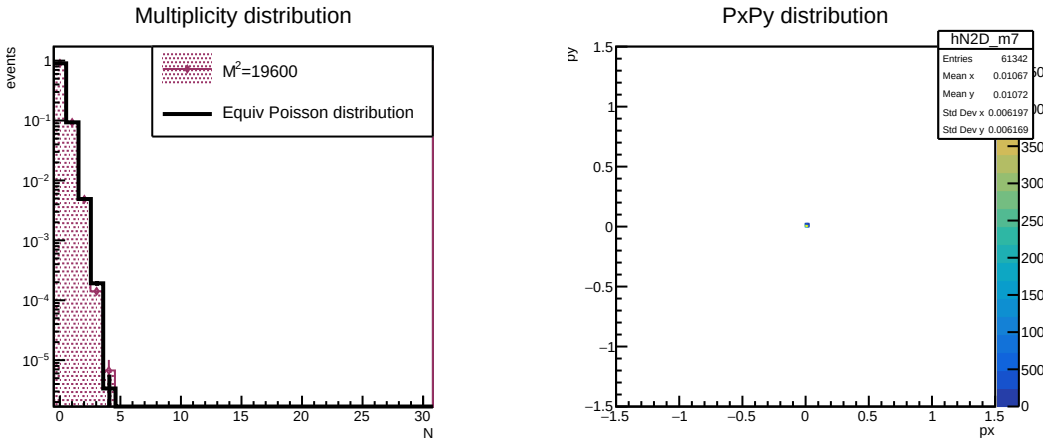

Figure B.9: Example Multiplicity distribution for cell when $M^2 = 19600$ with a Poisson fit(right). Example of the 2D $p_x - p_y$ distribution of the same cell for illustration (left).

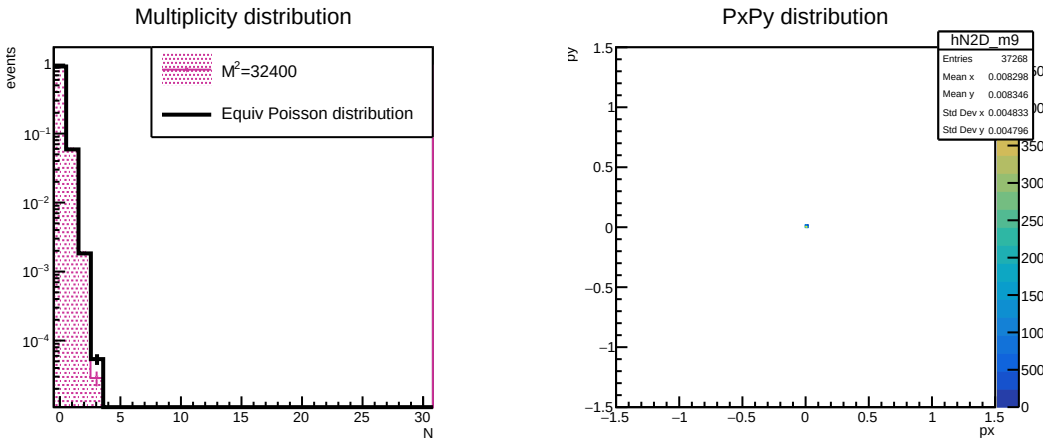

Figure B.10: Example Multiplicity distribution for cell when $M^2 = 32400$ with a Poisson fit(right). Example of the 2D $p_x - p_y$ distribution of the same cell for illustration (left).

APPENDIX C

CENTRALITY DETERMINATION

The determination of centrality in Xe+La analyses within NA61/SHINE was performed by Dr. Oleksandra Panova [72], [76]. In this work, only the resulting selection criteria were used for event analysis; in this text, I present a summary of her method.

In NA61/SHINE, centrality is estimated using data from the Projectile Spectator Detector (PSD) (See Sec. 3.2.2), which measures the total energy of all particles within its acceptance. The PSD is optimized to detect projectile spectators – nucleons that do not participate in the collision. For central collisions, fewer spectators reach the PSD, resulting in lower measured energy, whereas peripheral collisions produce higher PSD energies.

Figure C.1 shows an example of the mean PSD energy versus track multiplicity for each PSD module. Following standard NA61/SHINE procedures, only modules exhibiting a clear anticorrelation between these two quantities were used for centrality determination. Additionally, only modules that functioned reliably during the entire data-taking period (See Sec. 3.3)were included.

The total energy measured in the selected modules is referred to as PSD energy and denoted as (E_{PSD}). An online centrality preselection was applied using the T2 trigger (See Sec. 3.2.2). To evaluate the centrality range covered by this trigger and refine the selection, the PSD energy distributions from T1 and T2 triggered Xe+La events were compared:

- T1: includes all beam events (some without interaction).
- T2: includes events after applying all interaction and quality cuts.

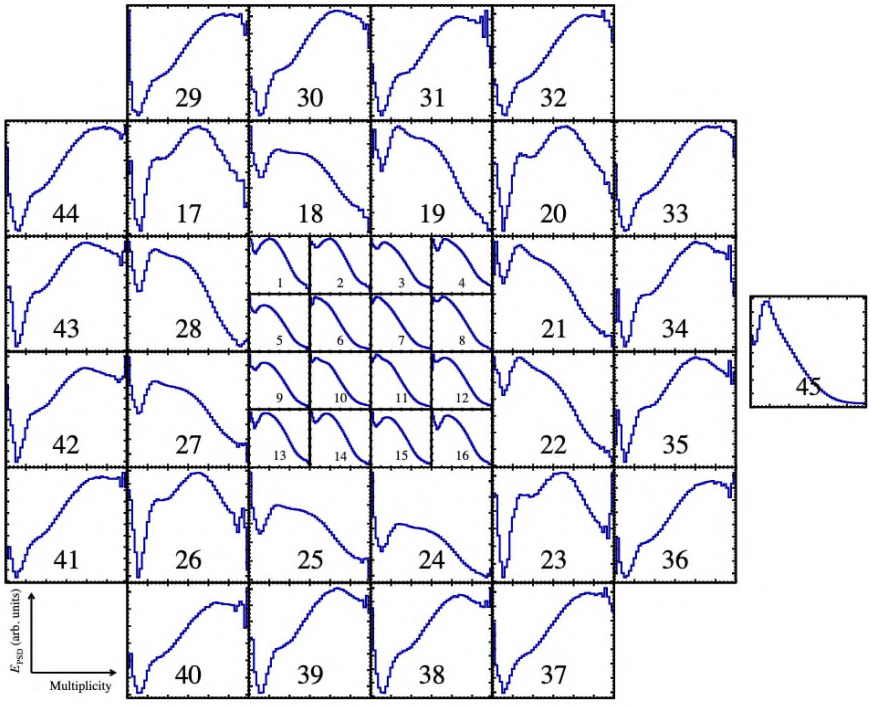

Figure C.1: Mean energy measured in each PSD module as a function of multiplicity of tracks measured by TPCs for Xe+La collisions at 40*A* GeV/*c* for 45 PSD modules. Only PSD modules with the anticorrelation were chosen for centrality selection. The range of the mean multiplicity is from 0 to 300. The range of the mean energy measured in each PSD module depends on the PSD module: the minimum is zero, and the maximum varies from 30 GeV for outer modules to 400 GeV for central modules. Image from [76].

An example of these distributions at 40*A* GeV/*c* is shown in Fig.C.2 (left). Both are normalized to their integral in a reference region. The interaction probability (P) for T1-triggered events is calculated as:

$$P = 1 - e^{-\frac{l\rho N_A \sigma}{m}},$$

where $l = 0.276 \pm 0.035$cm is the La target thickness, $\rho = 6.17 \pm 0.01$ g/cm^3 is its density, $m = 138.9055 \times 1.6605 \times 10^{-24} = 230.653 \times 10^{-24}$ g the atomic mass, and σ the interaction cross-section obtained from the GLISSANDO model, a Monte Carlo implementation of the Wounded Nucleon Model [77].

The fraction of events selected by the T2 trigger is estimated using:

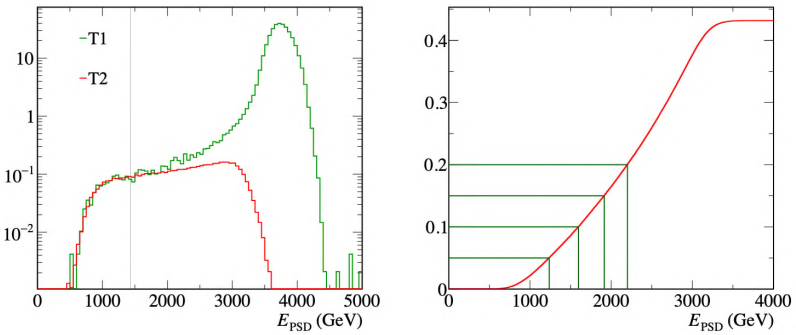

Figure C.2: Example distributions of the energy measured in the selected modules of the PSD for Xe+La collisions at 40*A* GeV/*c* recorded using the T1 and T2 triggers. Distributions are scaled to their integrals in the normalization region (to the left of the vertical grey line). Right: The cumulative distribution of the energy measured in the selected modules of the PSD for Xe+La collisions at 40A GeV/c recorded using the T2 trigger multiplied by C_{T2}. Image from [76]

$$C_{T2} = \frac{T2_{\text{int}}}{T1_{\text{int}} \cdot P},$$

where $T1_{\text{int}}$ and $T2_{\text{int}}$ are the integrals of the scaled PSD energy distributions for T1- and T2-triggered events, respectively.

The cumulative PSD energy distribution for Xe+La collisions at 40A GeV/c (T2 trigger, scaled by C_{T2} is shown in Fig. C.2 (right). Horizontal lines indicate 5%, 10%, 15%, and 20% centrality intervals, while vertical lines correspond to the E_{PSD} values that define these centralities. For the present analysis, only the 20% most central collisions were selected.

BIBLIOGRAPHY

[1] H. Satz,
Extreme states of matter in strong interaction physics: An introduction.
Berlin, Heidelberg: Springer Berlin Heidelberg, 2012,
Pp. 111–135.

[2] C. Gattringer and C. Lang,
Quantum chromodynamics on the lattice.
Berlin: Springer, 2010,
Vol. 788.

[3] C. Ratti and R. Bellwied,
The deconfinement transition of QCD: Theory meets experiment.
Springer, Jan. 2021.

[4] Z. Fodor and S. D. Katz, "Lattice determination of the critical point of qcd at finite t and μ,"
Journal of High Energy Physics, vol. 2002, no. 03, p. 014, Mar. 2002.

[5] P. de Forcrand and O. Philipsen, "The QCD phase diagram for small densities from imaginary chemical potential,"
Nuclear Physics B, vol. 642, no. 1–2, pp. 290–306, Oct. 2002.

[6] M. D'Elia and M. P. Lombardo, "Finite density QCD via an imaginary chemical potential,"
Physical Review D, vol. 67, no. 1, Jan. 2003.

[7] Allton, C. R. et al., "Equation of state for two flavor QCD at non-zero chemical potential,"
Physical Review D, vol. 68, no. 1, Jul. 2003.

[8] A. P. Society,
Historic website: The Bevatron,
Accessed: 2025-03-19.

[9] M. Asakawa and K. Yazaki, "Chiral restoration at finite density and temperature,"
Nuclear Physics A, vol. 504, no. 4, pp. 668–684, 1989.

[10] M. A. Stephanov,
Qcd phase diagram: An overview,
2006.

arXiv: hep-lat/0701002 [hep-lat].

[11] Barducci, A. et al.,
"Chiral phase transition at finite temperature and density,"
In *Proccedings of the ECFA Large Hadron Collider (LHC) Workshop: Physics and Instrumentation*,
1990.

[12] Shifman, M. et al., "QCD and resonance physics. Theoretical foundations,"
Nucl. Phys. B, vol. 147, pp. 385–447, 1979, Report numbers: ITEP-73-1978, ITEP-80-1978.

[13] K. Grebieszkow, for the NA49 and NA61 Collaborations, "NA49 and NA61/SHINE experiments: Results and perspectives,"
Acta Physica Polonica B, vol. 41, 2010.

[14] S. collaboration, "Cumulants and correlation functions of net-proton, proton, and antiproton multiplicity distributions in collisions at energies available at the bnl relativistic heavy ion collider,"
Physical Review C, vol. 104, no. 2, p. 024 902, 2021.

[15] NA61/SHINE Collaboration, "Measurements of higher-order cumulants of multiplicity and net-electric charge distributions in inelastic proton–proton interactions by NA61/SHINE,"
Eur. Phys. J. C, vol. 84, no. 9, p. 921, 2024.

[16] H. Satz, "Intermittency and critical behaviour,"
Nuclear Physics B, vol. 326, no. 3, pp. 613–618, 1989.

[17] Mukherjee, S. et al., "Intermittency, fluctuations and maximal chaos in an emergent universal state of active turbulence,"
Nature Physics, vol. 19, no. 6, pp. 891–897, Mar. 2023.

[18] A. N. Kolmogorov, "Dissipation of energy in the locally isotropic turbulence,"
Proceedings: Mathematical and Physical Sciences, vol. 434, no. 1890, pp. 15–17, 1991.

[19] del Rio, E. et al., "Theory of intermittency applied to classical pathological cases,"
Chaos: An Interdisciplinary Journal of Nonlinear Science, vol. 23, no. 3, p. 033 112, Jul. 2013.

[20] A. Bialas and R. Peschanski, "Moments of rapidity distributions as a measure of short range fluctuations in high-energy collisions,"
Nucl. Phys. B, vol. 273, pp. 703–718, 1986, Report number: SACLAY-SPH-T-85-101.

[21] A. Bialas and R. Peschanski, "Intermittency in multiparticle production at high-energy,"
Nucl. Phys. B, vol. 308, pp. 857–867, 1988, Report numbers: SACLAY-SPH-T-88-33, TPJU-4-88.

[22] L. J. S. Bradbury,

Turbulent shear flows. 4 : selected papers from the fourth International Symposium on Turbulent Shear Flows.
1st ed. 1985.
Berlin: Springer-Verlag, 1985.

[23] N. collaboration, "Search for the critical point of strongly-interacting matter in ^{40}Ar + ^{45}Sc collisions at 150A GeV/c using scaled factorial moments of protons,"
Eur. Phys. J. C, vol. 83, no. 9, p. 881, 2023.

[24] W. G. Paeng et al., "Scale-invariant hidden local symmetry, topology change, and dense baryonic matter. II.,"
Phys. Rev. D, vol. 96, no. 1, p. 014 031, 2017.

[25] J. Wosiek, "Intermittency in the Ising Systems,"
Acta Phys. Polon., vol. B19, pp. 863–866, 1988.

[26] A. Bialas and R. C. Hwa, "Intermittency parameters as a possible signal for quark-gluon plasma formation,"
Phys. Lett. B, vol. 253, pp. 436–438, 1991.

[27] F. Diakonos, et al.,
"Unbiased proton intermittency analysis for the detection of the QCD critical endpoint in ion collisions,"
In *Proceedings of Corfu Summer Institute 2021 School and Workshops on Elementary Particle Physics and Gravity*.

[28] T. Czopowicz,
Simple Power-Law Model for generating correlated particles,
arXiv: 2309.13706 [hep-ex],
2023.

[29] N. G. A. et al., "Critical Opalescence in Baryonic QCD Matter,"
Phys. Rev. Lett., vol. 97, p. 032 002, 3 Jul. 2006.

[30] Holynski, R. et al., "Evidence for Intermittent Patterns of Fluctuations in Particle Production in High-Energy Interactions in Nuclear Emulsion,"
Phys. Rev. Lett., vol. 62, pp. 733–736, 7 Feb. 1989.

[31] I.V. Ajinenko et al., "Intermittency patterns in π+p and K+p collisions at 250 GeV/c,"
Physics Letters B, vol. 222, no. 2, pp. 306–310, 1989.

[32] Derado, I. et al., "Investigation of intermittency in muon-proton scattering at 280 GeV,"
Z. Phys. C - Particles and Fields, vol. 47, pp. 23–29, 1990.

[33] A. Bialas and J. Seixas, "Strong intermittency in momentum space,"
Phys. Lett. B, vol. 250, pp. 161–163, 1990.

[34] N. collaboration, “An investigation of intermittency in proton-gold, oxygen-gold, sulphur-gold and sulphur-sulphur interactions at 200 GeV per nucleon,”
Z. Phys. C, vol. 61, pp. 551–562, 1994.

[35] R. e. a. Albrecht, “Intermittency and correlations in 200 GeV/nucleon S+S and S+Au collisions,”
American Physical Society, vol. 50, pp. 1048–1064, 2 Aug. 1994.

[36] M. Arslandok,
Probing bulk dynamics of the QGP with correlations and fluctuations,
Plenary talk in Quark Matter 2025, Frankfurt Germany,
2025.

[37] N. collaboration, “Search for the QCD critical point in nuclear collisions at 158A GeV at the CERN Super Proton Synchrotron (SPS),”
Phys. Rev. C, vol. 81, p. 064 907, 6 Jun. 2010.

[38] T. Anticic and et. al,
Critical fluctuations of the proton density in A+A collisions at 158A *GeV*,
2015.
arXiv: 1208.5292 [nucl-ex].

[39] S. collaboration, “Energy dependence of intermittency for charged hadrons in Au+Au collisions at RHIC,”
Phys. Lett. B, vol. 845, p. 138 165, 2023.
arXiv: 2301.11062 [nucl-ex].

[40] N. Davis,
“Searching for the chiral critical point of quark matter in relativistic ion collisions,”
Ph.D. dissertation, Athens Natl. Capodistrian U., 2015.

[41] N. collaboration, “Search for a critical point of strongly-interacting matter in central ^{40}Ar + ^{45}Sc collisions at 13 A–75A GeV/c beam momentum,”
Eur. Phys. J. C, vol. 84, no. 7, p. 741, 2024.

[42] A. Bialas and M. Gazdzicki, “A new variable to study intermittency,”
Phys. Lett. B, vol. 252, pp. 483–486, 1990.

[43] Samanta, S. et al, “Scaling of factorial moments in cumulative variables,”
Nucl. Phys. A, vol. 1015, p. 122 299, 2021.

[44] V. Z. R. O. for the NA61/SHINE collaboration,
First results of negatively charged hadrons intermittency in the NA61/SHINE collaboration,
Talk at the 15th Workshop of Critical Point and Onset of Deconfinement at Berkeley CA, USA,
May 2024.

[45] A. Bialas, "Intermittency and the Hanbury-Brown-Twiss effect,"
Acta Phys. Polon. B, vol. 23, pp. 561–567, 1992.

[46] T. Wibig, "Bose-Einstein source of intermittency in hadronic interactions,"
Phys. Rev. D, vol. 53, pp. 3586–3590, 1996.

[47] A. Bialas, "Intermittency, fractal sources, Levy distributions,"
AIP Conference Proceedings, vol. 828, no. 1, pp. 513–518, Apr. 2006.

[48] P. Brax and R. Peschanski, "Spikes, Anomalous Events and the Dimensional Structure of Multiparticle Fluctuations,"
Phys. Lett. B, vol. 253, pp. 225–230, 1991.

[49] T. Csörgő, S. Hegyi, and W. A. Zajc, "Bose-Einstein Correlations for Levy Stable Source Distributions,"
Eur. Phys. J. C, vol. 36, p. 67, 2004.

[50] T. Csörgő, S. Hegyi, and T. Novák, "Bose-Einstein or HBT Correlations and the Core-Halo Picture of Particle Emission,"
Acta Phys. Pol. B, vol. 36, p. 329, 2005.

[51] V. R. Ortiz, M. Rybczyński, and Z. Włodarczyk, "Scaling for count-in-cell and factorial moment analysis,"
Nuclear Physics B, vol. 1018, p. 117 051, 2025.

[52] V. Z. Reyna Ortiz, M. Rybczynski, and Z. Wlodarczyk, "Probing multi-particle bunching from intermittency analysis in relativistic heavy-ion collisions,"
Nucl. Phys. A, vol. 1053, p. 122 980, 2025.

[53] N. collaboration, "NA61/SHINE facility at the CERN SPS: Beams and detector system,"
JINST, vol. 9, P06005, Jan. 2014.

[54] M. Gazdzicki, and Z. Fodor, and G. Vesztergombi for the NA49-future collaboration,
Study of Hadron Production in Hadron-Nucleus and Nucleus-Nucleus Collisions at the CERN SPS,
2006.

[55] CERN,
New schedule for CERN's accelerators,
Accessed: 09-09-2025,
Oct. 2024.

[56] Abe, K. et al., "The T2K experiment,"
Nuclear Instruments and Methods in Physics Research Section A: Accelerators, Spectrometers, Detectors and Associated Equipment, vol. 659, no. 1, pp. 106–135, 2011.

[57] M. U. for the NA61/SHINE collaboration,

"New results from the cosmic-ray program of the na61/shine facility at the cern sps,"
In *Proceedings of 36th International Cosmic Ray Conference -ICRC2019-*,
Sep. 2019,
P. 446.

[58] M. Gazdzicki and P. Seyboth, "Search for Critical Behaviour of Strongly Interacting Matter at the CERN Super Proton Synchrotron,"
Acta Physica Polonica B, vol. 47, no. 5, p. 1201, 2016.

[59] A. A. for the NA61/SHINE collaboration,
"Report from the NA61/SHINE experiment at the CERN SPS,"
CERN, Geneva,
Tech. Rep.,
2018.

[60] M. Gazdzicki, M. Gorenstein, and P. Seyboth, "Onset of Deconfinement in Nucleus-Nucleus Collisions,"
Acta Physica Polonica B, vol. 42, no. 2, p. 307, 2011.

[61] M. Gazdzicki, "The Mixed Phase Collision Energy Range from the Experimental Data,"
Acta Phys. Polon. B, vol. 45, no. 12, M. Praszalowicz, Ed., p. 2319, 2014.

[62] A. Makhnev, et al., "New Beam Position Detectors for NA61/SHINE experiment,"
J. Phys.: Conf. Ser., vol. 2374, no. 1, p. 012 057, 2022.

[63] NA61/SHINE collaboration,
Charm Program of NA61/SHINE: Motivation and Measurements,
Mar. 2018.
arXiv: 1803.01692 [nucl-ex].

[64] P. S. for the NA61/SHINE collaboration, "Open charm measurements in NA61/SHINE at CERN SPS,"
Nuclear Physics A, vol. 982, pp. 879–882, 2019.

[65] NA61/SHINE Collaboration,
Proposal from the NA61/SHINE Collaboration for update of European Strategy for Particle Physics,
Jul. 2025.
arXiv: 2507.08602 [nucl-ex].

[66] CERN,
The H2 Secondary Beam Line of EHN1/SPS,
Accesed: 2017-09-30.

[67] R. A.-F. et al.,
Performance of the CERN Low Energy Ion Ring (LEIR) with Xenon beams,

2018.

[68] A. Aduszewicz for the NA61/SHINE collaboration,
Xe+La 2017 data taking,
2018.

[69] A. A. for the NA61/SHINE collaboration,
"Report from the NA61/SHINE experiment at the CERN SPS,"
CERN, Geneva,
Tech. Rep.,
2018.

[70] P. Podlaski,
"Study of charged hadron production with tof-dE/dx identification method in central Ar+Sc collisions in NA61/SHINE experiment at CERN,"
Ph.D. dissertation, Warsaw University, 2021.

[71] B. Kurgyis, et al, "Coulomb Corrections for Bose–Einstein Correlations from One- and Three-Dimensional Lévy-Type Source Functions,"
Universe, vol. 9, no. 7, p. 328, Jul. 2023.

[72] O. Panova and E. Z. for the NA61 collaboration,
Event cuts and centrality selection for Xe+La at 13A-150A GeV/c,
2024.

[73] V. Z. R. O. for the NA61 collaboration,
Negatively charged hadron intermittency at Xe+La 150A GeV/c,
2024.

[74] R. Barlow,
Systematic Errors: facts and fictions,
arXiv: 0207026,
2002.

[75] T. Pierog and K. Werner, "EPOS Model and Ultra High Energy Cosmic Rays,"
Nuclear Physics B - Proceedings Supplements, vol. 196, pp. 102–105, Dec. 2009.

[76] O. Panova,
"Study of charged hadron production with tof-dE/dx identification method in central Ar+Sc collisions in NA61/SHINE experiment at CERN,"
Ph.D. dissertation, Jan Kochanowski University of Kielce, 2025.

[77] M. Rybczyński, G. Stefanek, W. Broniowski, and P. Bożek, "Glissando 2: Glauber initial-state simulation and more..., ver. 2,"
Computer Physics Communications, vol. 185, no. 6, pp. 1759–1772, Jun. 2014.

List of Tables

List of Figures

FIGURE **Page**